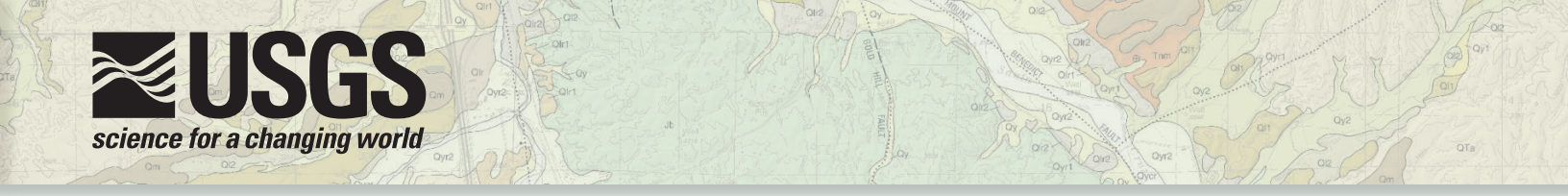

USGS
science for a changing world

Bedrock Morphology and Structure, Upper Santa Cruz Basin, South-Central Arizona, with Transient Electromagnetic Survey Data

Open-File Report 2016–1152

U.S. Department of the Interior
U.S. Geological Survey

Bedrock Morphology and Structure, Upper Santa Cruz Basin, South-Central Arizona, with Transient Electromagnetic Survey Data

By Mark W. Bultman and William R. Page

Open-File Report 2016–1152

U.S. Department of the Interior
U.S. Geological Survey

U.S. Department of the Interior
SALLY JEWELL, Secretary

U.S. Geological Survey
Suzette M. Kimball, Director

U.S. Geological Survey, Reston, Virginia: 2016

For more information on the USGS—the Federal source for science about the Earth, its natural and living resources, natural hazards, and the environment—visit http://www.usgs.gov or call 1–888–ASK–USGS.

For an overview of USGS information products, including maps, imagery, and publications, visit http://store.usgs.gov/.

Suggested citation:
Bultman, M.W., and Page, W.R., 2016, Bedrock morphology and structure, upper Santa Cruz Basin, south-central Arizona, with transient electromagnetic survey data: U.S. Geological Survey Open-File Report 2016–1152, 49 p., http://dx.doi.org/10.3133/ofr20161152.

ISSN 2331-1258 (online)

Acknowledgments

We greatly appreciate the technical reviews of the report completed by Mark Gettings and Geoffrey Phelps; their comments and suggestions vastly improve the report. In addition, copy editing by Lisa Binder and final illustration drafting by Jeff Hartley contributed enormously to the quality of the final report.

Contents

Plates

Figures

Tables

Appendixes

Conversion Factors

International System of Units to U.S. customary units

Multiply	By	To obtain
	Length	
meter (m)	3.281	foot (ft)
kilometer (km)	0.6214	mile (mi)
	Area	
square meter (m^2)	10.76	square foot (ft^2)
	Mass	
gram (g)	0.03527	ounce, avoirdupois (oz)
metric ton (t)	1.102	ton, short (2,000 lb)
	Density	
gram per cubic centimeter (g/cm^3)	62.4220	pound per cubic foot (lb/ft^3)
	Acceleration	
milligal (mGal)	3.281×10^{-5}	ft. per second squared ($ft./s^2$)
	Magnetic field strength	
nT (nanoTesla)	1.000×10^{-5}	gauss (G)
	Magnetic field intensity	
amperes/meter (A/m)	1.257×10^{-2}	oersteds (Oe)

Datum

Vertical coordinate information is referenced to the North American Vertical Datum of 1988 (NAVD 88).

Horizontal coordinate information is referenced to the North American Datum of 1983 (NAD 83).

Universal Transverse Mercator, zone 12 north

Altitude, as used in this report, refers to distance above the vertical datum.

Supplemental Information

Specific conductance is given in microsiemens per centimeter at 25 degrees Celsius (µS/cm at 25 °C).

Bedrock Morphology and Structure, Upper Santa Cruz Basin, South-Central Arizona, with Transient Electromagnetic Survey Data

By Mark W. Bultman and William R. Page

Abstract

The upper Santa Cruz Basin is an important groundwater basin containing the regional aquifer for the city of Nogales, Arizona. This report provides data and interpretations of data aimed at better understanding the bedrock morphology and structure of the upper Santa Cruz Basin study area which encompasses the Rio Rico and Nogales 1:24,000-scale U.S. Geological Survey quadrangles. Data used in this report include the Arizona Aeromagnetic and Gravity Maps and Data referred to here as the 1996 Patagonia Aeromagnetic survey, Bouguer gravity anomaly data, and conductivity-depth transforms (CDTs) from the 1998 Santa Cruz transient electromagnetic survey (whose data are included in appendixes 1 and 2 of this report).

Analyses based on magnetic gradients worked well to identify the range-front faults along the Mt. Benedict horst block, the location of possibly fault-controlled canyons to the west of Mt. Benedict, the edges of buried lava flows, and numerous other concealed faults and contacts. Applying the 1996 Patagonia aeromagnetic survey data using the horizontal gradient method produced results that were most closely correlated with the observed geology.

The 1996 Patagonia aeromagnetic survey was used to estimate depth to bedrock in the upper Santa Cruz Basin study area. Three different depth estimation methods were applied to the data: Euler deconvolution, horizontal gradient magnitude, and analytic signal. The final depth to bedrock map was produced by choosing the maximum depth from each of the three methods at a given location and combining all maximum depths. In locations of rocks with a known reversed natural remanent magnetic field, gravity based depth estimates from Gettings and Houser (1997) were used.

The depth to bedrock map was supported by modeling aeromagnetic anomaly data along six profiles. These cross sectional models demonstrated that by using the depth to bedrock map generated in this study, known and concealed faults, measured and estimated magnetic susceptibilities of rocks found in the study area, and estimated natural remanent magnetic intensities and directions, reasonable geologic models can be built. This indicates that the depth to bedrock map is reasonable and geologically possible.

Finally, CDTs derived from the 1998 Santa Cruz Basin transient electromagnetic survey were used to help identify basin structure and some physical properties of the basin fill in the study area. The CDTs also helped to confirm depth to bedrock estimates in the Santa Cruz Basin, in particular a region of elevated bedrock in the area of Potrero Canyon, and a deep basin in the location of the Arizona State Highway 82 microbasin. The CDTs identified many concealed faults in the study area and possibly indicate deep water-saturated clay-rich sediments in the west-central portion of the study area. These sediments grade to more sand-rich saturated sediments to the south with relatively thick, possibly unsaturated, sediments at the surface. Also, the CDTs may indicate deep saturated clay-rich sediments in the Highway 82 microbasin and in the Mount Benedict horst block from Proto Canyon south to the international border.

Introduction

This report provides an analysis of geophysical data from the Rio Rico and Nogales 1:24,000-scale U.S. Geological Survey (USGS) quadrangles, Santa Cruz County, Arizona (fig. 1). This area, referred to as the study area, includes the city of Nogales, Arizona. This report is intended to compliment the Geologic Map of the Rio Rico and Nogales 1:24,000-scale U.S. Geological Survey quadrangles, Santa Cruz County, Arizona (Page and others, 2016). Our primary objective was to describe the depth to bedrock, general morphology and structure of the upper Santa Cruz Basin (fig. 1) in the study area, and define its relationship to the geohydrology of the region. The upper Santa Cruz Basin occupies the entire study area except for two places: (1) where it is split by Mt. Benedict in the central part of the upper Santa Cruz Basin study area and; (2) where the southern flank of the San Cayetano Mountains and Grosvenor Hills enters the study area in the northern part of the study area (fig. 2).

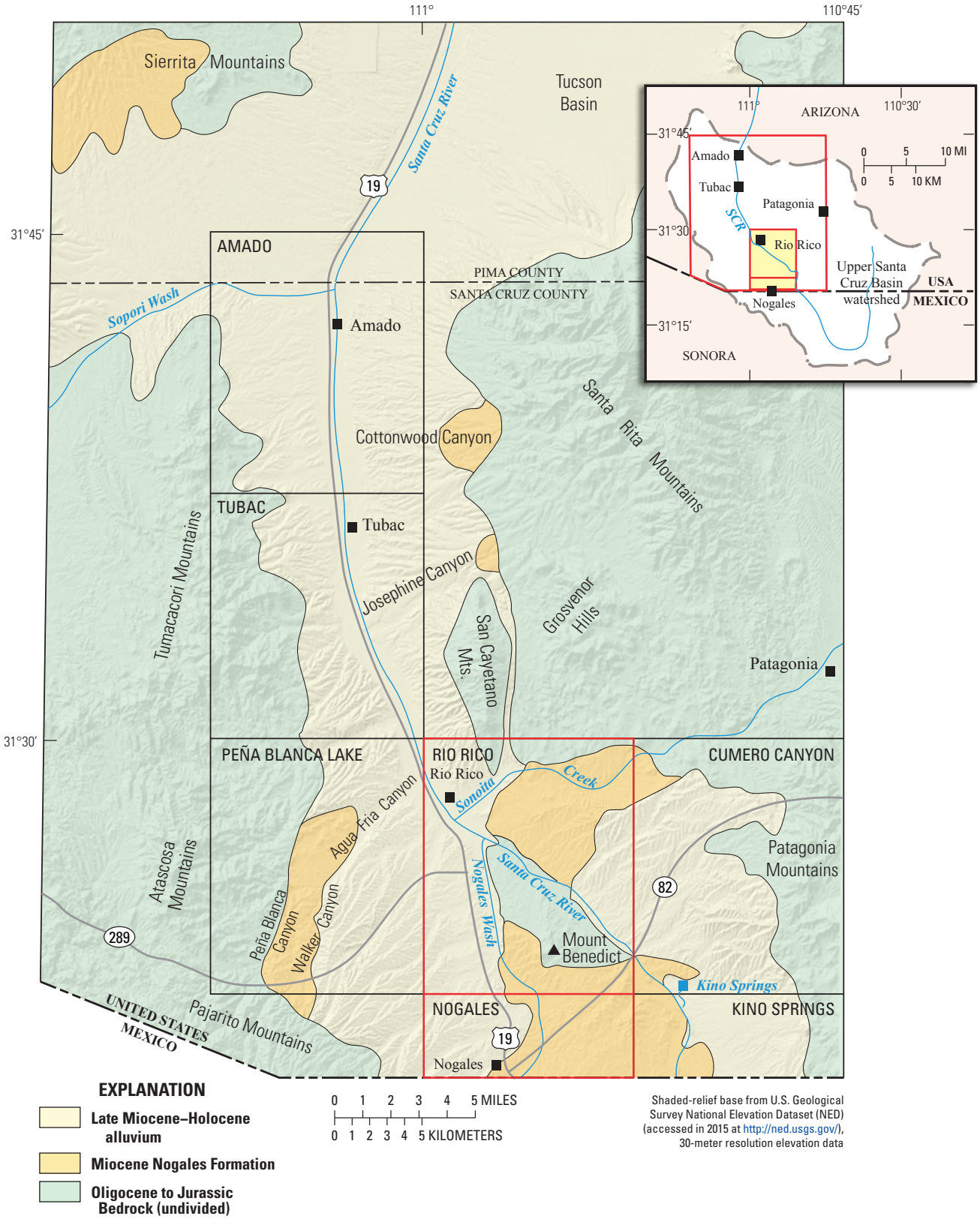

Figure 1. Map showing location of upper Santa Cruz basin study area (Rio Rico and Nogales, Arizona 1:24,000-scale quadrangles outlined in red). Map shows the generalized geology as well as major physiographic and hydrologic features in the region. Black squares are town locations. Inset map in upper right shows location of upper Santa Cruz River basin with boundary in red, Santa Cruz River (SCR) in blue, and the location of Rio Rico and Nogales quadrangles outlined in red and shaded in yellow (after Page and others, 2016).

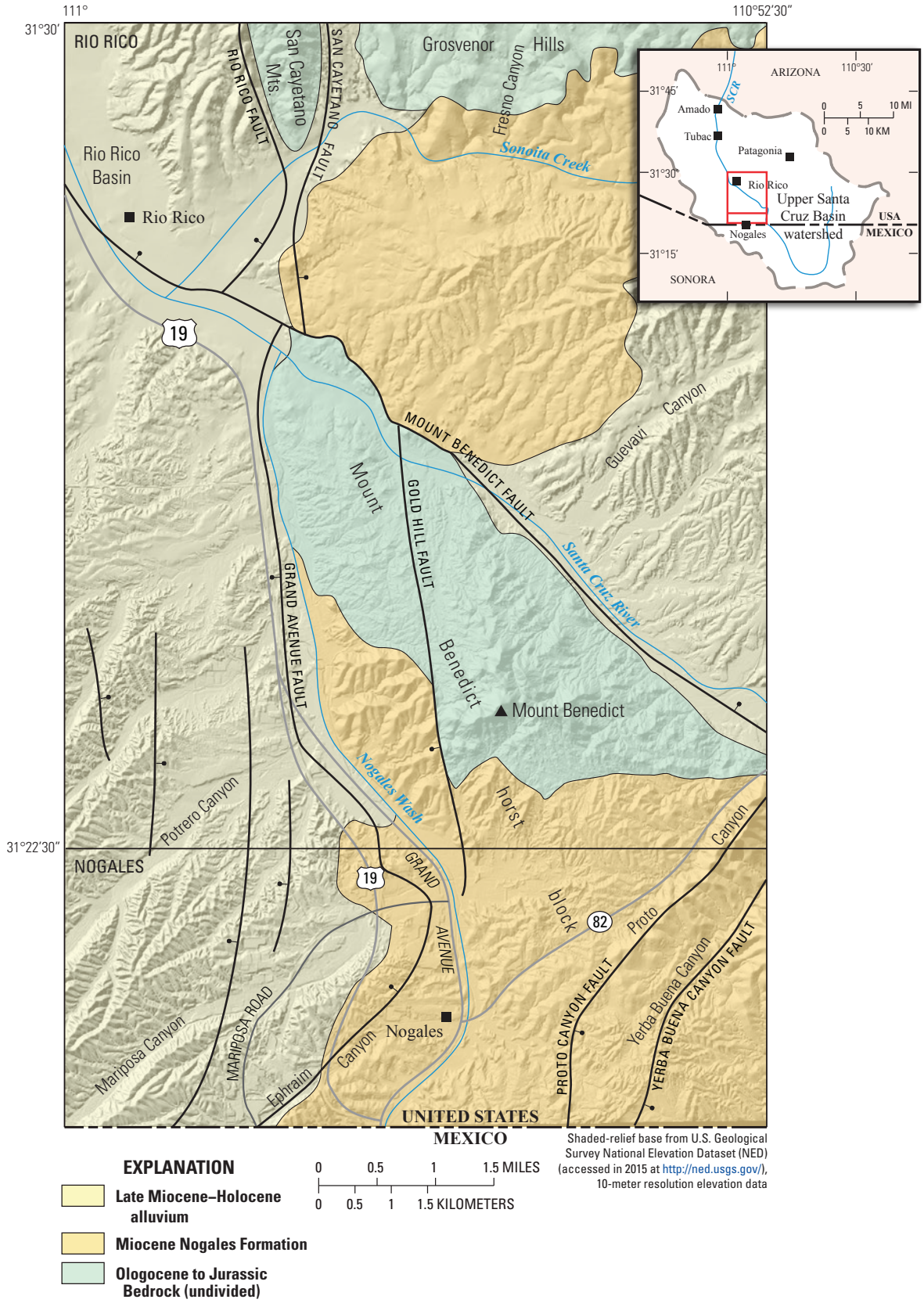

Figure 2. Map of upper Santa Cruz Basin study area (Rio Rico and Nogales, Arizona 1:24,000-scale quadrangles) showing major geologic, physiographic, and hydrologic features. Black squares are town locations and black ball and bar symbols indicate the downthrown side of normal faults (after Page and others, 2016).

A groundwater basin can be defined as "A hydrologic unit of groundwater storage defined as an area more or less separate from neighboring groundwater storage areas" (Richard and others, 2007). The upper Santa Cruz Basin can be considered a groundwater basin, and therefore constraints on the storage and availability of groundwater are important for proper characterization of groundwater as a resource. The thickness, distribution, and character of sediments deposited in the upper Santa Cruz Basin provide important constraints on the ground-water availability of the area. This report considers several geophysical techniques, each of which provides an estimate of the thickness of sediments in the upper Santa Cruz Basin. Additionally, the report includes some information on the distribution and character of those sediments.

The geophysical data used in this report include Earth's gravity anomaly data from a nationwide database (University of Texas at El Paso [UTEP], 2014) and Earth's magnetic field anomaly data from the Arizona Aeromagnetic and Gravity Maps and Data, referred to here as the 1996 Patagonia aeromagnetic survey (Sweeney and Hill, 2001), and data from a 1998 transient electromagnetic survey of the Santa Cruz Basin. Data from the 1998 transient electromagnetic survey have not been published in their entirety prior to this report, and two appendixes are provided here that include all data from that survey.

The gravity data were interpreted for depth to bedrock in the upper Santa Cruz Basin by Gettings and Houser (1997) and no new depth interpretation of those data is presented here. In this report we use the results of Gettings and Houser (1997) to supplement our depth analyses as necessary. The gravity data are also used in this report to identify edges of bedrock bodies with contrasting density by analyzing the horizontal gradient and analytic signal of the interpolated gravitational field.

This report applies aeromagnetic data from the 1996 Patagonia aeromagnetic survey (Sweeney and Hill, 2001) to estimate basin depth in a region where depth has already been estimated by gravity data. This was done for two reasons. First, the gravity data in the upper Santa Cruz Basin are spatially sparse; there are a small number of gravity stations that are quite spread out. The aeromagnetic data available are much denser spatially and provide a depth to bedrock map with a higher spatial resolution. Tectonism and erosion created complex topography in the bedrock as it was being inundated with sediments, and tectonism has continued since the basin was formed. This resulted in a complex morphology of the bedrock surface that requires data with a high spatial resolution to properly define the buried bedrock surface. Second, all geophysical solutions are non-unique and can have relatively high uncertainty. It is therefore important to use all available methods to get multiple independent solutions for any problem that is addressed by geophysical methods.

Aeromagnetic data from the 1996 Patagonia aeromagnetic survey (Sweeney and Hill, 2001) are also used to interpret edges of bedrock bodies with contrasting magnetic intensities. In addition, forward modeling of magnetic anomalies in cross section is used to check the veracity of parts of the depth to bedrock map.

Conductivity-depth transforms (CDTs) derived from the 1998 transient electromagnetic survey are presented and used to further increase understanding of the basin morphology, structure, depth to bedrock, and hydrogeology of the upper Santa Cruz Basin. The CDTs provide information on the thickness, distribution, and character of basin fill sediments that were deposited in the upper Santa Cruz Basin and provide important constraints on the groundwater availability of the area.

Geologic Setting of the Study Area

The upper Santa Cruz Basin is located in the southern Basin and Range province in southeastern Arizona in the United States, and northern Sonora in Mexico (fig. 1 inset). The terrain is composed of alternating fault-bounded linear mountain ranges and sediment-filled basins that trend generally north-south (fig. 1) that began to form in the Miocene. The mountain ranges restrict groundwater movement and storage and confine the majority of useable groundwater to the basin fill. In this report we define the basin fill as the Upper Miocene to Holocene sediments and the Miocene Nogales Formation (fig. 1).

The rocks that compose the mountain ranges surrounding the upper Santa Cruz Basin and that lie structurally below the basin fill will be referred to in this report as bedrock. The upper Santa Cruz Basin is flanked to the west by the Tumacacori and Atascosa Mountains (fig. 1) composed primarily of Tertiary rhyolites and andesites. The Pajarito Mountains, mostly Cretaceous volcanics, form the southwest boundary of the basin (Drewes, 1980). To the east lie the Patagonia Mountains which are cored by a Late Cretaceous quartz monzonite and have Jurassic and Precambrian granites on the western flank. The Santa Rita and San Cayetano mountains form the north end of the study area. These mountains are composed of a variety of rocks including igneous, metamorphic, volcanic, and sedimentary bedrock ranging in age from Precambrian to Miocene (Drewes, 1971, 1972, 1980).

The basin fill in the upper Santa Cruz Basin is composed of Miocene to Holocene sand and gravel deposits of alluvial fans, valley centers, terraces, and channels (Gettings and Houser, 1997). On the basis of age and consolidation, Gettings and Houser (1997) defined two basin-fill units that are recognized in the upper Santa Cruz Basin: (1) the Miocene Nogales Formation, that is poorly to moderately well consolidated, and (2) the upper basin-fill unit composed of upper Miocene to lower Pleistocene unconsolidated to poorly consolidated sediments. These are overlain by Pleistocene and Holocene surficial deposits including alluvium of stream channels, flood plains, and terraces that are unconsolidated overall but locally well indurated.

The bedrock geology for parts of the study area has been mapped at 1:48,000 by Simons (1974) and at 1:125,000 by

Drewes and others (2002) and Drewes (1996, 1980). Page and others (2016) recently published a map of the Rio Rico and Nogales 1:24,000-scale quadrangles that focuses on the Tertiary and Quaternary. This report was produced in conjunction with the map of Page and others (2016), and used geologic data from the map and helps to understand the concealed geologic features on that map.

Previous Geophysical Analysis and Depth to Bedrock Estimates

The 1996 Patagonia aeromagnetic survey covers an area that extends approximately 10 kilometers (km) to the east and west of the upper Santa Cruz Basin study area and 20 km to the north of it. In 2002, three studies were published that analyzed the entire 1996 Patagonia aeromagnetic survey.

Gettings (2002) provided a thorough study and included a comparison of the aeromagnetic data with geologic mapping, demonstrating correlation of magnetic anomalies with mapped geology, and showing that numerous map units of volcanic and intrusive rocks from the Jurassic, Cretaceous, and Middle Tertiary have significant natural magnetic remanence. Gettings also carried out a textural analysis of the aeromagnetic data which matched magnetic anomaly texture with exposed rock units, enabling prediction of the location of these rock units when hidden beneath basin fill.

Phillips (2002) used analytic techniques on the 1996 Patagonia aeromagnetic data to delineate contacts and make depth estimates of the bedrock basement based on three methods of depth estimation. They include the horizontal gradient method, the analytic signal method, and the local wavenumber method. The horizontal gradient method (Cordell and Grauch, 1985; Blakely and Simpson, 1986) is dependent on carrying out a "reduction to the pole" operation that recalculates total magnetic intensity data as if the inducing magnetic field had a 90-degree inclination. This transformation converts dipolar magnetic anomalies to dipolar magnetic anomalies centered over the geologic bodies responsible for the anomaly. The horizontal gradient method has a low sensitivity to noise and its maxima are highly continuous and generally parallel to the contours of the reduced-to-pole aeromagnetic field. The horizontal gradient method assumes that the Earth's magnetic field is aligned with the direction of remanent magnetism in the source rocks. It also assumes, when using reduced-to-the-pole magnetic data, that contacts are vertical and separate thick horizontal sheets of source rock. Violations of these assumptions required for good depth estimation using the horizontal gradient method can result in displacement of the contacts away from their true locations. In the case of a simple dipping fault that juxtaposes rock units of differing magnetic properties, the displacement is typically down dip from the true contact location (Grauch and Cordell, 1987).

The analytic signal method is more susceptible to noise in the magnetic field data but provides results that are independent of the directions of source remanent magnetization and the local geomagnetic field (Nabighian, 1972). Depths are generally accurate for contacts and are too shallow for most other source types (Phillips, 1997). The local wave number method is very sensitive to noise in the magnetic field. Both of these methods provide contacts between units of contrasting susceptibility that are less continuous than the horizontal gradient method.

Depth to bedrock in the upper Santa Cruz Basin has been estimated by several authors. They are (with their primary method of investigation in parentheses if known): Halpenny, 1964; Oppenheimer and Sumner, 1980 (gravity); Halpenny and Halpenny, 1988; Saltus and Jachens, 1995 (gravity); Gettings and Houser, 1997 (gravity); Richard and others, 2007 (geophysical data); and Culbertson and others, 2010 (transient electromagnetic data). The most comprehensive study for estimating depth to bedrock in the upper Santa Cruz Basin was Gettings and Houser (1997) because the other reports were carried out at too small a scale or only looked at small portions of the upper Santa Cruz Basin. Gettings and Houser (1997) used complete Bouguer gravity anomaly and water well data to obtain a depth to bedrock map for the upper Santa Cruz Basin. Porosity and saturated bulk density were estimated using a combination of down-hole gravimeter data from nearby bore holes in similar sediments, grain density measurements of cuttings, and surface gravimetric profiles. Gettings and Houser (1997) calculated the porosity of the Nogales Formation at 16 percent yielding a saturated bulk density of 2.32 grams per cubic centimeter (g/cm^3); the porosity of the upper basin fill was calculated to be 21 percent yielding a saturated bulk density of 2.24 g/cm^3. Depth to bedrock was estimated using a procedure involving interpolation of: (1) the density functions derived in their report; (2) stratigraphic data from water wells; (3) a residual gravity anomaly grid obtained by subtracting the gravity effects of the bedrock ranges bordering the basin from the complete Bouguer gravity anomaly; and (4) depth to bedrock estimates from three Natural Uranium Resource Evaluation (NURE) aeromagnetic profiles (http://www.ngdc.noaa.gov/geomag/fliers/nure.shtml). The Gettings and Houser (1997) depth to bedrock map for the upper Santa Cruz Basin extends from approximately Green Valley, Arizona (north of the study area) to the United States-Mexican border. The portion of that map within the upper Santa Cruz Basin study area is shown (fig. 3) as contours plotted over basin geology from Page and others (2016). Figure 4 presents the map units for the geologic map displayed in figure 3.

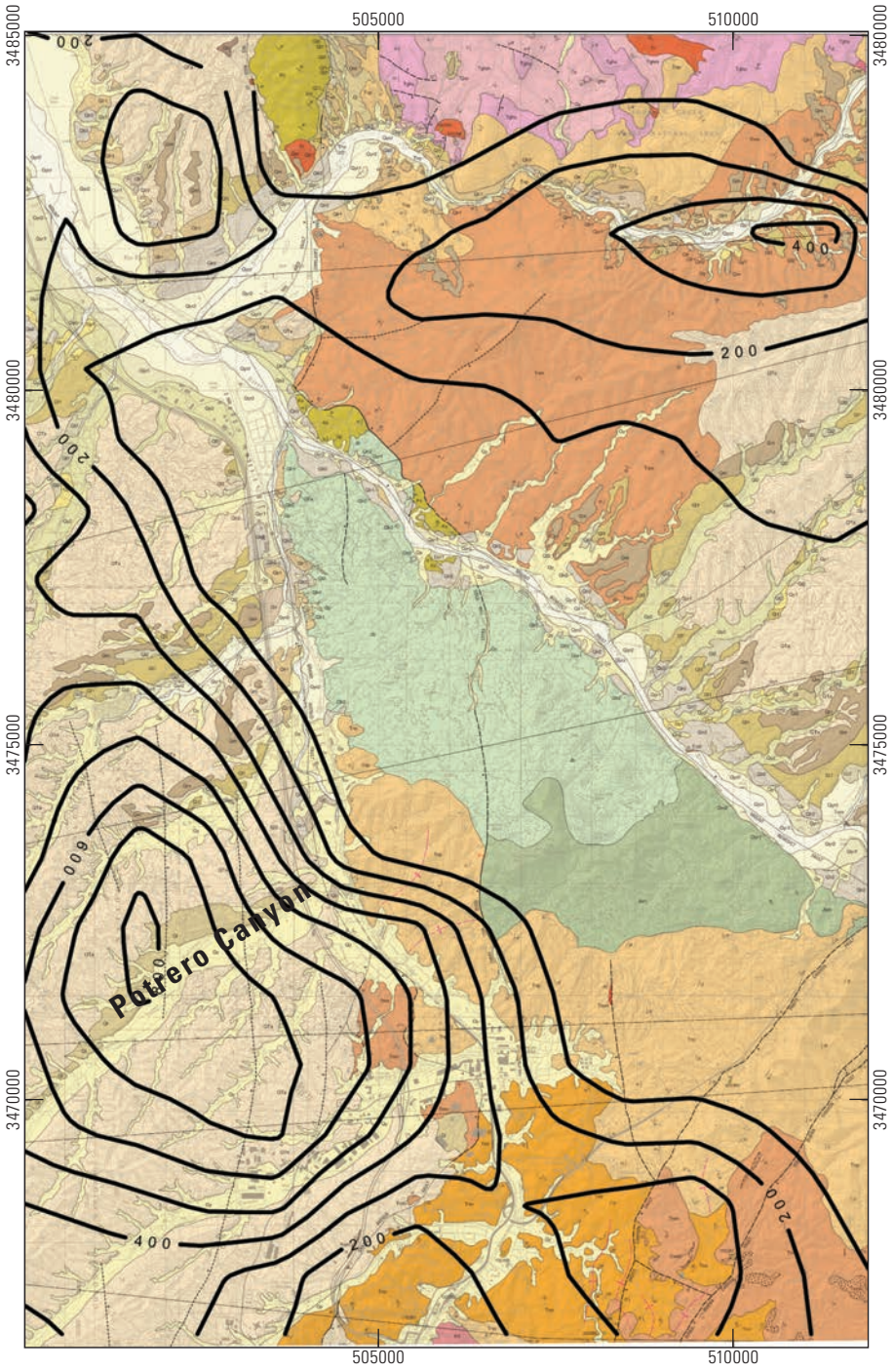

Figure 3. Map showing depth to bedrock in the upper Santa Cruz Basin study area. Estimated depth from the portion of Gettings and Houser's (1997) depth to bedrock map that fall within the upper Santa Cruz Basin study area is shown as contours plotted over basin geology from Page and others (2016).

Figure 4. List of map units for upper Santa Cruz Basin study area geologic map (after Page and others, 2016).

Potential Field Data and Analysis in the Study Area

Potential Field Datasets

Gravity data used in this report were downloaded from the University Texas at El Paso gravity database of the United States (UTEP, 2014). Complete Bouguer anomaly data show the effects of different rock densities in the subsurface and are ideal for locating concealed faults and contacts. Complete Bouguer anomaly data were extracted from the database and gridded at 100 m and the resulting Complete Bouguer anomaly grid for the study area is shown in figure 5 displayed as a color shaded relief image. It includes the location of gravity stations used to produce the grid. Figure 5 shows that most gravity data were acquired along roads and that there are large areas with no data at all. The spacing between gravity stations along roads varies from about 100 meters to a few hundred meters. A grid cell size of 100 m was chosen so that anomalies observed that were caused by station spacing along roads would be depicted in the gridded data.

The 1996 Patagonia aeromagnetic survey data were obtained from Sweeney and Hill (2001). The aeromagnetic data in this survey were collected along east-west flight lines spaced 250 m apart at a nominal terrain clearance of 230 m (Sweeney and Hill, 2001). Data were also collected along several widely-spaced north-south tie lines that were used to level the flight line data. In addition, these data are corrected for the flight direction of the aircraft (magnetic compensation), corrected for daily changes in the Earth's magnetic field due to changes in currents of charged particles in the ionosphere (diurnal corrections), and have a mathematical model of the Earth's magnetic field called the International Geomagnetic Reference Field or IGRF (National Oceanic and Atmospheric Administration [NOAA], 2014). All of these corrections, which were performed by Sial, the contractor that acquired the data (U.S. Geological Survey, 2000), and produced the magnetic anomaly data which are used in all the aeromagnetic analyses in this report. Many aeromagnetic maps gridded from flight line data show significant streaking or "corrugation" along the flight line direction caused by elevation shifts between adjacent flight lines probably due to large changes in elevation over the survey area. This corrugation can be corrected for by a technique developed by Urquhart (1988) and implemented by Phillips (1997, 2007). Figure 6 shows the decorrugated aeromagnetic data from the 1996 Patagonia aeromagnetic survey over the study area gridded with a cell size of 50 m and displayed as a color shaded relief image.

Techniques for the Analysis of Potential Field Data

Certain functions of potential field data have local extrema over sharp contrasts of rock magnetic intensity (the vector sum of rock magnetic susceptibility and remanence) for magnetic data and rock density for gravity data. Curvature analysis (Blakely and Simpson, 1986) of these functions can be used to locate these function extrema and by association the resulting contrast in rock properties. These sharp contrasts in rock properties are inferred to be contacts or faults and can be observed even when they are buried by non-magnetic basin fill.

Two such functions are used here to infer the location of buried faults and contacts with both Earth's magnetic field data and the complete Bouguer anomaly data: the horizontal gradient magnitude and the analytic signal. In addition, these functions can both be used to estimate the depths of sources of magnetic anomalies, as can a third function, the Euler deconvolution. All three of these functions are used in this report to estimate the depth of rock bodies within the study area

Horizontal Gradient Magnitude Method

The horizontal gradient method is dependent only on horizontal derivatives of the potential field data and is relatively insensitive to noise and aliasing; it tends to produce results that are spatially continuous. For Earth's magnetic field data locations of contacts based on the horizontal gradient method are more accurate when applied to reduced-to-the pole data. This procedure converts dipolar magnetic anomalies to dipolar anomalies centered over the geologic bodies responsible for the anomaly. Assuming thick homogeneous rock units, contacts with non-vertical dips will result in horizontal locations of contacts that are down dip from the true locations (Grauch and Cordell, 1987). This method also assumes that the natural remanent magnetic field of the rocks in question is aligned with the present day field (Bournas and Baker, 2001). Blakely and Simpson (1986) used the horizontal gradient magnitude method to determine the edges of bodies and structures using both Earth's magnetic field and gravity data. Phillips (2000, 2007) used the horizontal gradient method to accurately locate the tops of isolated vertical contacts and faults from the reduced-to-pole magnetic field.

Roest and Pilkington (1993) first proposed the use of the horizontal gradient method for depth estimation. As with contact locations, this method is more accurate when using reduced-to-the pole Earth's magnetic field data and when the rock's natural remanent magnetic field is aligned with the present day field (Bournas and Baker, 2001). Phillips (2000) discusses details of the method: it works best for vertical contacts with a large depth extent, as depth estimates are generally biased to be too shallow and false deep contacts may appear parallel to the actual contact due to dipolar effects when this method is applied to a thin horizontal body. In the analysis used in this report, most contacts found buried by basin fill in the Upper Santa Cruz Basin tend to be offsets in bedrocks that are extensive in depth; few effects from thin horizontal bodies are expected. However, it should be noted that there are several relatively thin basalt flows of limited areal extent interbedded in the basin fill near the Mexican border. These are thin horizontal bodies may be magnetic enough to affect the aeromagnetic data and give false (too shallow) depth to bedrock estimates.

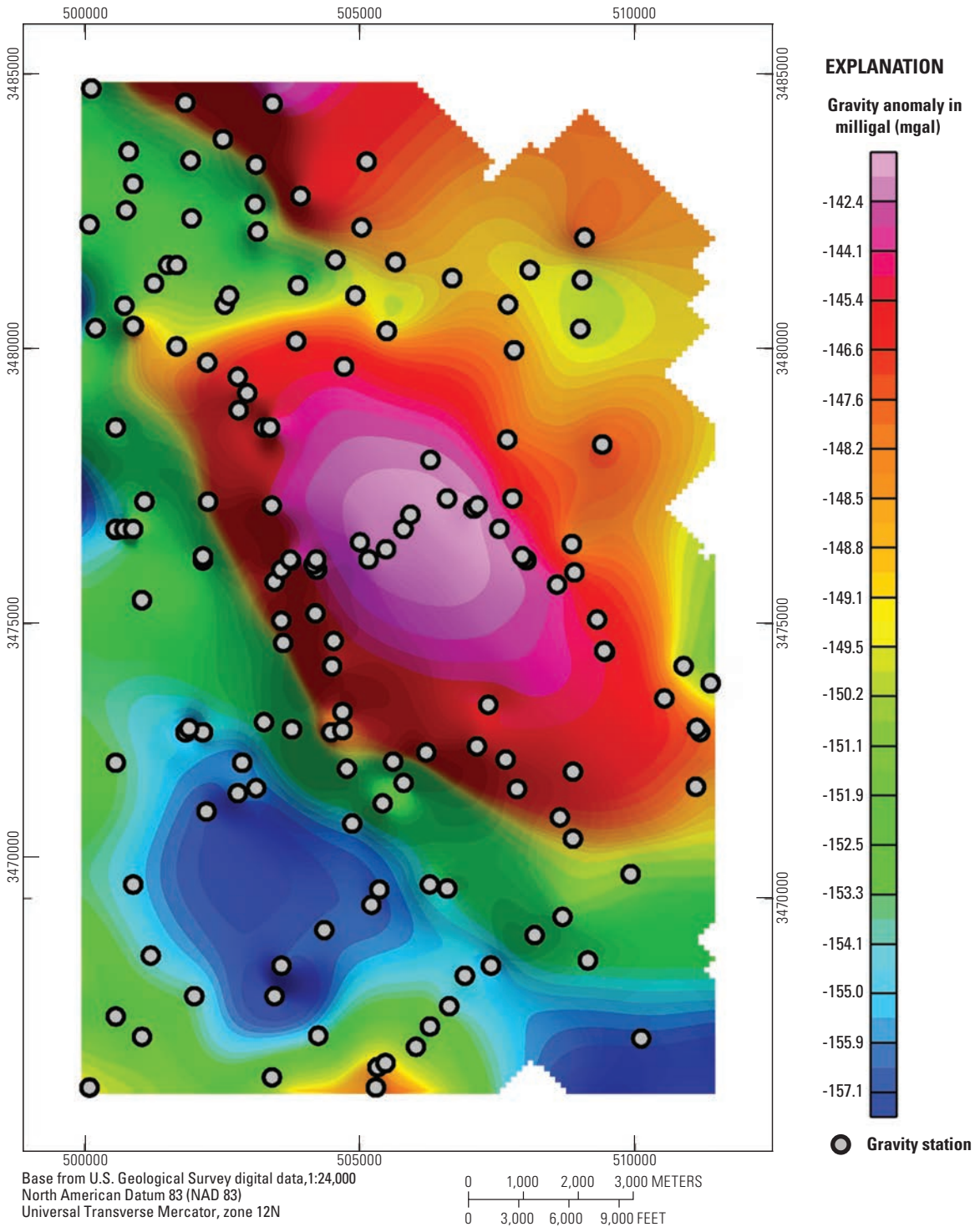

Figure 5. Map showing complete Bouguer gravity anomaly in the upper Santa Cruz Basin study. Data extracted from The University of Texas at El Paso gravity database (UTEP, 2014), gridded with a cell size of 100 m and displayed as a color shaded relief image.

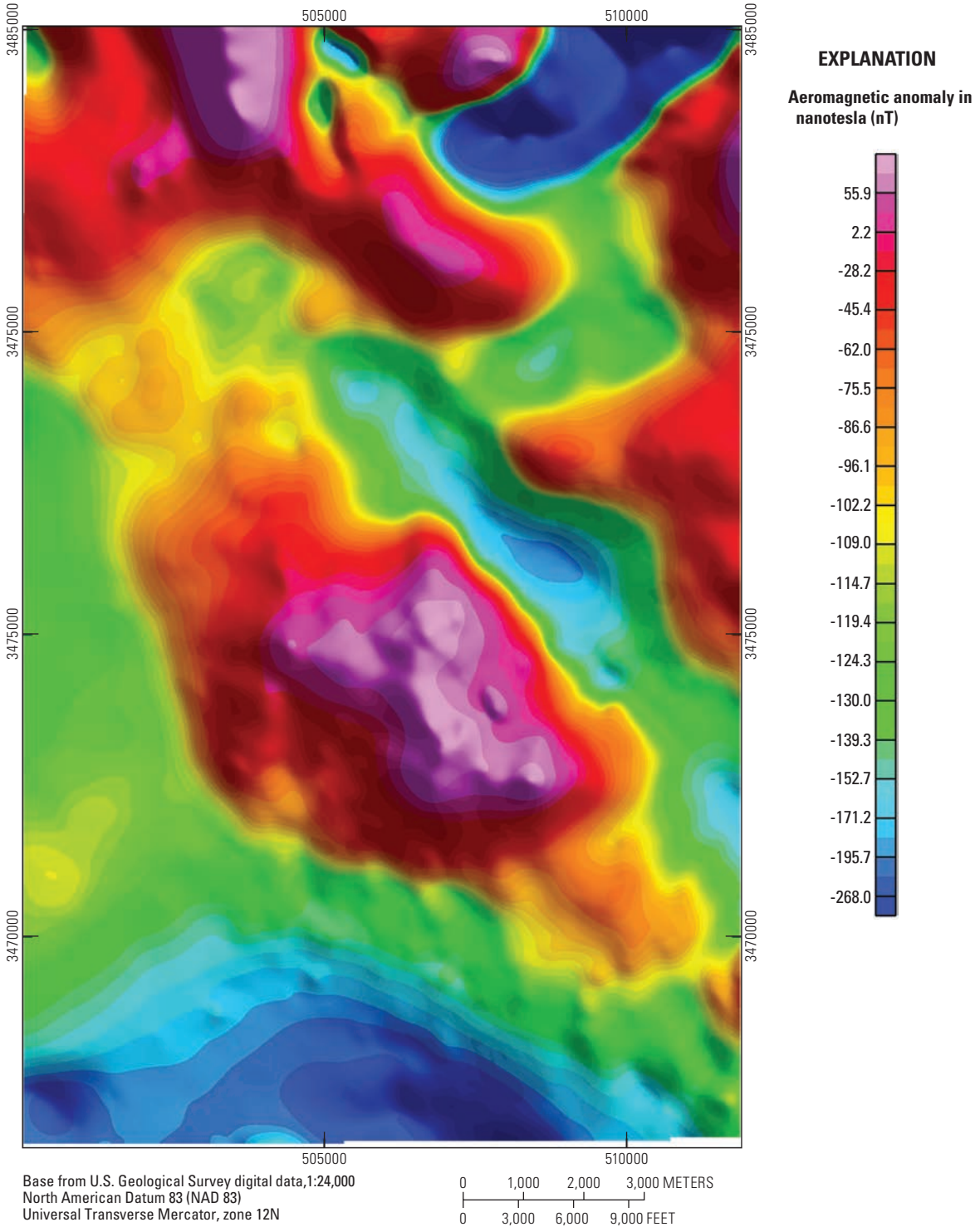

Figure 6. Map showing aeromagnetic anomalies in the upper Santa Cruz Basin study area using aeromagnetic data from the 1996 Patagonia aeromagnetic survey over the study area (Sweeny and Hill, 2001), gridded with a cell size of 50 m and displayed as a color shaded relief image.

Analytic Signal Method

The analytic signal method can be applied directly to the observed Earth's magnetic field and produces good horizontal locations for contacts regardless of their geologic dip or the geomagnetic latitude (Phillips, 2000). The peaks of the analytic signal function occur over the edges of wide bodies and over the center of narrow bodies (Gunn, 1997). This method produces diffuse peaks over structural edges (Gunn, 1997) and it is more sensitive to noise and aliasing than the horizontal gradient method (Phillips, 2000) and because of this tends to produce contacts that are less continuous than the horizontal gradient method (Phillips, 2000).

The analytic signal method can also be used for depth estimation (Nabighian, 1972, 1974, 1984). This method is independent of magnetization direction and the aeromagnetic data do not need to be reduced-to-the pole (Hsu and others, 1998). Depths to contacts are generally accurate but depth estimates are too shallow for most other source types such as horizontal and non-horizontal sheet sources, isolated linear sources, three-dimensional sources, pipeline sources, and so forth (Phillips, 2000). Since this method is more sensitive to noise than the horizontal gradient method, it may be necessary to upward continue the data, which leads to some loss of resolution (Phillips, 2000).

Euler Deconvolution

Potential field anomalies that are caused by magnetic sources obey Euler's homogeneity equation (Hood, 1965), and Euler deconvolution of potential field data is based on that relationship. The value of the exponent in Euler's homogeneous equation (degree of homogeneity) is source-dependent and characterizes how fast the potential field decreases as a function of distance from the source. When used for potential field analysis, the negative of the exponent in the Euler homogeneity equation is referred to as the structural index and it controls how an anomaly from a dipolar source decreases as a function of distance from the source. Due to the non-linear mathematics used in the analysis, the Euler deconvolution method is more susceptible to noise that either the horizontal gradient of analytic signal method. Common structural indices are n=3 for a sphere, n=2 for a cylinder, n=1 for a dike, and n=0.5 for a fault or contact. The method returns depth estimates for sources based on the selected structural index. Thompson (1982) developed the technique to apply Euler's deconvolution to profile data and Reid and others (1990) developed a technique for grid-based data.

Analysis of Potential Field Gradient Data in the Study Area

We applied both the horizontal gradient magnitude and analytic signal methods to Earth's magnetic and gravity fields for the purpose of locating buried faults and contacts. For the horizontal gradient magnitude method the 1996 Patagonia aeromagnetic data were gridded at 50 m, and holes in the data were plugged and the data were decorrugated (Phillips, 1997). Then, the data were reduced-to-the pole and the horizontal gradient magnitude technique was applied. It should be noted that these data were also converted to pseudogravity data (Cordell and Grauch, 1985). When used with the horizontal gradient method, pseudogravity data provide contact locations that are accurate on both vertical and dipping contacts. Unfortunately, the resulting dataset displayed large edge effects along the southern boundary of the study area and did not represent the non-transformed data well and was thus not used. Curvature analysis was used to locate ridges (linear, curvilinear, or arcuate highs) in the horizontal gradient magnitude datasets. These ridges represent a potential field boundary (magnetic field in this case) between rocks with differing geophysical properties (magnetic susceptibly, magnetic remanence, or both in this case). The results are plotted as symbols (red dots) on plate 1 overlying the geologic map by Page and others (2016). These ridges represent potential field boundaries and will be referred to (in general) as geophysical or potential field boundaries or (specifically, based on the type of data that generated the ridge) as Earth's magnetic field horizontal gradient magnitude boundaries, Earth's magnetic field analytic signal boundaries, complete Bouguer anomaly horizontal gradient magnitude boundaries, or complete Bouguer anomaly analytic signal boundaries.

The analytic signal method was applied to the 1996 Patagonia aeromagnetic data and was gridded at 50 m; the results were unsatisfactory due to noise. The data were re-gridded at 100 m (a low pass filter) and the analytic signal method then produced plausible results, although contacts were not as continuous as those produced by the horizontal gradient method. Curvature analysis was used to locate potential field boundaries as with the horizontal magnitude data and the results are plotted as symbols (black dots) on plate 1 overlying the geologic map by Page and others (2016).

The horizontal gradient magnitude method and the analytic signal method were also applied to the complete Bouguer anomaly data, gridded at 100 m. Curvature analysis was used to locate potential field boundaries (based on density in this case) in the datasets and these are displayed on plate 1 using blue dots for the complete Bouguer anomaly horizontal gradient magnitude boundaries and gray dots for the complete Bouguer anomaly analytic signal boundaries.

Plate 1 is a tool for looking at possible bedrock structure at both small and large scales in the study area. Individual potential field boundaries can display large scale structure, while combinations of similarly trending geophysical boundaries can indicate small scale regional features. There are several things to consider when interpreting the results of the analyses shown on plate 1. First, the methods detect differences in contrasting susceptibilities or densities. If there is little or no contrast, a fault or contact will not be detected using these methods. Second, changes in susceptibility or density can occur because of alteration, or tectonic, igneous, or sedimentary

processes not associated with a fault or depositional contact. Third, horizontal gradient magnitude analysis of Earth's magnetic field data appears to be the dominant feature on the map. This is likely due to the fact that the horizontal gradient magnitude analysis was applied to the 1996 Patagonia aeromagnetic data gridded at 50 m. For the analytic signal method, these data had to be gridded at 100 m due to noise in the data. Recall that potential field boundaries produced from the horizontal gradient method can be offset from the actual location of the physical boundary (contact) if the contacts are not vertical. When these techniques are applied to Earth's gravity data they produce fewer results due to both the relatively small number of gravity survey stations (fig. 5) and the 100-m-grid cell size in these data. The horizontal gradient analysis of gravity data does produce a number of useful relationships.

There are a number of interesting relationships that appear on plate 1 and a few are described below and tied to numerals located on the plate. These are simply a few random locations that appeared interesting to the authors. There are many other locations that could be analyzed in a similar fashion. Map coordinates are in Universal Transverse Mercator (UTM), zone 12 north.

- Location 1, plate 1, map coordinates 503600E, 3479300N:

Here, an Earth's total intensity magnetic field anomaly horizontal gradient magnitude boundary (red dots) appears to connect the Grand Avenue and San Cayetano faults (see fig. 2) across the basin based on the 1996 Patagonia aeromagnetic data. Surface data indicate that the displacement of the faults is in opposite directions, that is, down to the west on the Grand Avenue fault and down to the east on the San Cayetano fault. Also, the Grand Avenue fault has much more offset in this region than the San Cayetano fault, approximately 0.5 km compared to 0.1 km. This geophysical boundary may reflect a splay of the Grand Avenue fault or simply indicate the northern extent of map unit Jb (table 1). Also, moving south from location 1, the aeromagnetic horizontal gradient maximum hugs the range front right along the Grand Avenue fault then moves west of where the concealed fault is thought to exist near the surface. The subsurface expression of this range front fault may move basinward here, or a piece of map unit Jb may exist to the west of the fault here.

- Location 2, plate 1, map coordinates 503000E, 3470100N:

Farther south along the Grand Avenue fault from location 1, the Earth's magnetic field horizontal gradient magnitude boundary may show a westward splay of the fault that merges with a nearly north-south complete Bouguer anomaly horizontal gradient magnitude boundary (blue dots). The gravity data may depict a deeper part of this range front fault (the Grand Avenue fault) lying west of the main fault. The range front fault is clearly seen as both gravity and magnetic potential field boundaries in the basin fill further south where both of these features turn east near location 2a, at map coordinates 506000E, 3473800N.

- Location 3, plate 1, map coordinates 502000E, 3472900N:

Here, an Earth's magnetic field horizontal gradient magnitude boundary is aligned with an inferred fault along an unnamed canyon that runs along N. Al Harrison Road in the city of Nogales, Ariz. In addition, several other similar alignments can be seen in this area.

- Location 4, plate 1, map coordinates 502100E, 3473000N:

At this location, an Earth's magnetic field horizontal gradient magnitude boundary runs parallel to a mapped inferred fault about 0.3 km west of location 4.

- Location 5, plate 1, map coordinates 510000E, 3477600N:

An Earth's magnetic field horizontal gradient magnitude boundary runs just to the south of this location and trends along a north-east trending concealed fault. Potential splays of this fault may exist along Earth's magnetic field horizontal gradient magnitude boundaries just to the north and south of this location.

- Location 6, plate 1, map coordinates 508500E, 3476300N:

The Mt. Benedict fault (see fig. 2) can be seen as a complete Bouguer anomaly horizontal gradient magnitude boundary in this location. About 1 km to the north of this location the geophysical boundary moves to the northeast of the mapped fault and may show that the predominant range front fault is associated with this feature (or the Earth's total intensity magnetic field anomaly horizontal gradient magnitude boundary just to the west, see location 7 below) especially considering that bedrock (map unit Ks) appears east of the mapped surface location of the Mt. Benedict fault which follows the Santa Cruz River. Also, a complete Bouguer anomaly horizontal gradient magnitude boundary demarks the southern boundary of the Mt. Benedict Jurassic igneous rocks (map units Jb and Jbm) at location 6a, at map coordinates 506000E, 3472000N.

- Location 7, plate 1, map coordinates 505900E, 3478300N:

Here, an Earth's magnetic field horizontal gradient magnitude boundary is strongly correlated with the mapped fault (the Mt. Benedict fault) that forms the east side of the graben in which the Santa Cruz River runs.

- Location 8 plate 1, map coordinates 510200E, 3483200N:

Two northeast trending Earth's magnetic field horizontal gradient magnitude boundaries may be edges of buried volcanic rocks or structural features. The feature to the south of location 8 seems to control the path of Sonoita Creek in this area.

Table 1. Map units used for modeling aeromagnetic anomalies in the Santa Cruz basin study area (modified from Drewes, 1980, 1996; Drewes and others, 2002; Page and others, 2016).

[Map units, map units modified from fig. 4 and used in models shown in figs. 16 through 21; Q_e, estimated Koenigsberger ratio; A/m, amperes per meter; --, no data or information not available.]

Map units	Map unit color in figs.16–21	Map unit description, source	Normal/reverse polarity of the natural remanent magnetic field	Q_e (estimated from fig. 14)	Susceptibility (SI), *k*	Apparent suceptibility (SI, see text) K_a	Remanent magnetic intensity (A/m)	Inclination of remanent field	Declination of remanent field	Source of rock magnetic susceptibility	Source of rock remanent magnetic vector
Tn		All Tertiary and Quaternary basin fill	normal	0.6	0.001	0.001	--	--	--	Gettings, 2002	--
Tv		Extrusive andesite and dacite with reversed natural magnetic remanence (Drewes, 1980, 1996; Drewes and others, 2002)	reversed	1.5	0.01	--	0.58	–42	170	Estimated from fig. 13	Miocence-Oligocene Mogolion-Datil volcanic rocks, Diehl and others (1988)
Tghu		Grosvenor Hills upper rhyodacite (Page and others, 2016)	normal	2	0.013	0.002	--	--	--	Estimated from fig. 13	--
Tghu		Grosvenor Hill upper rhyodacite with reversed natural magnetic remanence (Page and others, 2016)	reversed	2 to 1.3	0.013	--	1.0 to 0.60	–42	170	Estimated from fig. 13	Miocence-Oligocene Mogolion-Datil volcanic rocks, Diehl and others (1988)
Ti		Intrusive rhyolite and dacite with reversed natural magnetic remanence (Drewes, 1980, 1996; Drewes and others, 2002)	reversed	0.9	0.04	--	1.4	–58.8	167.5	Estimated from fig. 13	From Gringo Gulch volcanic rocks, Hagstrum (1994)
Kd		Diorite with reversed natural remanent magnetic field (Page and others, 2016)	reversed	1.3	0.006	--	0.3	–48.2	164.9	Estimated from fig. 13	From Elehant Head igneous rocks, Hagstrum (1994)
Kd		Diorite with normal natural remanent magnetic field (Page and others, 2016)	normal	1.3	0.006	0.013	--	--	--	This report, sample SC1	--
Ks		Salero Formation (Page and others, 2016)	normal	--	0.005	0.014	--	--	--	Estimated from fig. 13	--
Ks		Salero Formation (Page and others, 2016)	reversed	2	0.005	--	0.4	–48.2	164.9	Estimated from fig. 13	From Elehant Head igneous rocks, Hagstrum (1994)
Jg		Cumero Canyon granite (Drewes, 1980, 1996; Drewes and others, 2002)	normal	1.4	0.02	0.046	--	--	--	Estimated from fig. 13	--
Jg		Cumero Canyon granite with reversed natural remanent magnetic field, (Drewes, 1980, 1996; Drewes and others, 2002)	reversed	1.4	0.02 to 0.007	--	1.1	–39	157	Estimated from fig. 13	From Canelo Hills volcanics, Kluth and others (1982)
Jb		Biotite-hornblende quartz monzonite of Mt Benedict (Page and others, 2016)	normal	0.6	0.007	0.01	--	--	--	This report, sample SC3	--
Jb		Biotite-hornblende quartz monzonite of Mt Benedict with reversed natural magnetic remanence (Page and others, 2016)	reversed	3	0.007	--	0.8	–39	157	This report, sample SC3	From Canelo Hills volcanics, Kluth and others (1982)
Jbm		Quartz monzonite of Mt Benedict (Page and others, 2016)	normal	0.6	0.005	0.007	--	--	--	This report, sample SC 15	--
PCh		Hornblende rich granite (Drewes, 1980, 1996; Drewes and others, 2002)	normal	0.6	0.016	0.025	--	--	--	Gettings and Bultman, 2014	--

- Location 9, plate 1, map coordinates 503400E, 3483800N:

North and east-trending Earth's magnetic field horizontal gradient magnitude boundaries lie parallel and close to the San Cayetano fault and may show other faults in this structurally complex region.

Depth Analysis of Aeromagnetic Data in the Study Area

Gettings and Houser (1997) produced a depth to bedrock map (results of which are shown with contours in fig. 3) in the upper Santa Cruz Basin that fully utilizes the Earth's gravity data found in the study area. Their model of the depth to bedrock is used here for comparison purposes and to fill gaps where the aeromagnetic data do not provide adequate depth estimates. We used the 1996 Patagonia aeromagnetic survey to estimate depths in the upper Santa Cruz Basin, an analysis not previously investigated. Depths were estimated using three different methods: horizontal gradient analysis, analytic signal analysis and Euler deconvolution, except in regions where the direction of remanent magnetization was reversed with respect to the earth's magnetic field and significantly modifies the total magnetic field. In those regions the depth estimates of Gettings and Houser (1997) were used.

Estimation of Depth to Bedrock

A unique approach to estimating depth to bedrock was taken. Euler deconvolution applied to the 1996 Patagonia aeromagnetic data was chosen as a starting point for the creation of a depth to bedrock surface. This method allowed removal of depth estimates with large errors by choosing a small depth tolerance. Also, while multiple depths are often given for a single source or group of sources, many of the deeper estimates made using this method were close to depth estimates based on Gettings and Houser (1997), especially in the deeper parts of the basin. This consistency in estimated depth between the gravity based estimates and the deeper Euler estimates made the Euler deconvolution the method of choice for the aeromagnetic data based depth estimates. The high data density of the 1996 Patagonia aeromagnetic survey allowed us to create a higher resolution, and correspondingly more complex, depth to bedrock map.

The 50 m resolution 1996 Patagonia aeromagnetic data were upward continued 70 m, and the Euler deconvolution method was applied using a structural index of 0.5. Using an upward continuation of 70 m, the number of depth estimates for sources was greater than 1 per estimate window, higher than the resolution of the data allowed. The data were upward continued until these excess source estimates were reduced to a resolution of approximately 1 per window, 70 m. This level of filtering, and a depth tolerance of 15 percent (the default setting) created dozens of a reasonable number of estimates. Larger or smaller values of upward continuation or depth tolerance were found to produce too few or too many (multiples of the same source or many closely spaced sources) depth estimates.

The Euler deconvolution method only provided depth solutions over parts of the basin (fig. 7) and gridding these estimates left much of the basin with no estimated depth (fig. 8). Some of these depth estimates were negative, that is they would locate the depth of the source above the Earth's surface. This can occur if there is noise in the aeromagnetic data producing a very high gradient in the data or from a mismatch of the actual shape of the source and the structural index used in the estimation technique to approximate the shape of the source. Also, depth estimates greater than zero occur over exposed bedrock. These estimates can occur from a mismatch of the actual shape of the source and the structural index used in the estimation technique to approximate the shape of the source or if strong magnetic anomalies occur at depth within the bedrock.

In order to provide depth estimates for the entire basin, both horizontal gradient and analytic signal methods were also used to generate depths. Both estimates used the 50 m gridded 1996 Patagonia aeromagnetic dataset. For the horizontal gradient method, the data were reduced-to-the pole. These depth estimates are displayed in figures 9 and 10 respectively. Both methods produce estimates that are in general shallower than the Euler depth estimates.

In order to produce a depth to bedrock estimate across the entire study area, the three depth datasets were combined and the deepest of the three depth estimates was chosen. This was done for several reasons. First, the deeper Euler deconvolution depth to bedrock estimates were similar to the gravity based depth to bedrock estimates in the deeper parts of the upper Santa Cruz Basin by Gettings and Houser (1997). These estimates are consistent across two very different depth estimation techniques, and therefore have a higher likelihood of being accurate. Second, for many types of sources both the horizontal gradient magnitude and the analytical signal method are known to give estimates that are too shallow (Phillips, 2000; Casto, 2001). These relationships were also observed in depth estimates in this study. Picking the deeper estimates from these two methodologies is reasonable, especially when their depth to bedrock estimates tend to be shallower that the Euler deconvolution and gravity estimates. Third, in the southeast part of the study area there are lava flows interbedded in the Nogales formation sediments (Page and others [2016], displayed on pl. 1 and 2). The lava flows may be magnetic enough to create their own source estimates that would interfere with the estimates for deeper sources. Choosing the deepest estimates from each method may help reduce interference from these flows. Fourth, rocks with a reversed natural remanent magnetism are known to exist in the study area, and these will tend to decrease the observed magnetic anomaly and the depth estimate for a magnetic source. Choosing the deepest estimates from each method may help reduce depth estimation errors from rocks with reversed natural remanent magnetism. The resulting dataset was smoothed to a resolution 200 m to filter out high frequency noise in the depth estimates.

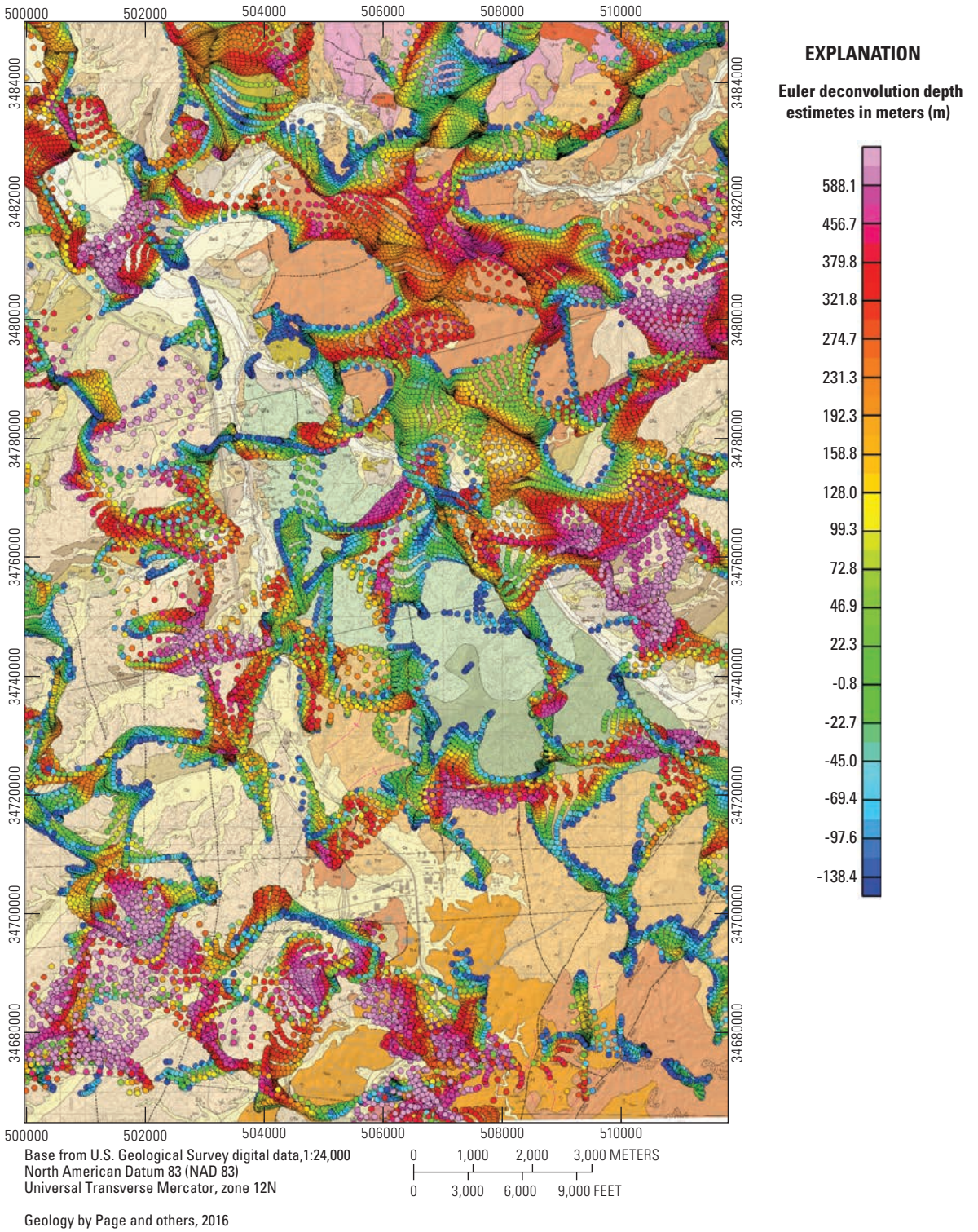

Figure 7. Map showing Euler deconvolution depth estimate solutions using a structural index of 0.5 in the upper Santa Cruz Basin study area plotted over basin geology from Page and others (2016).

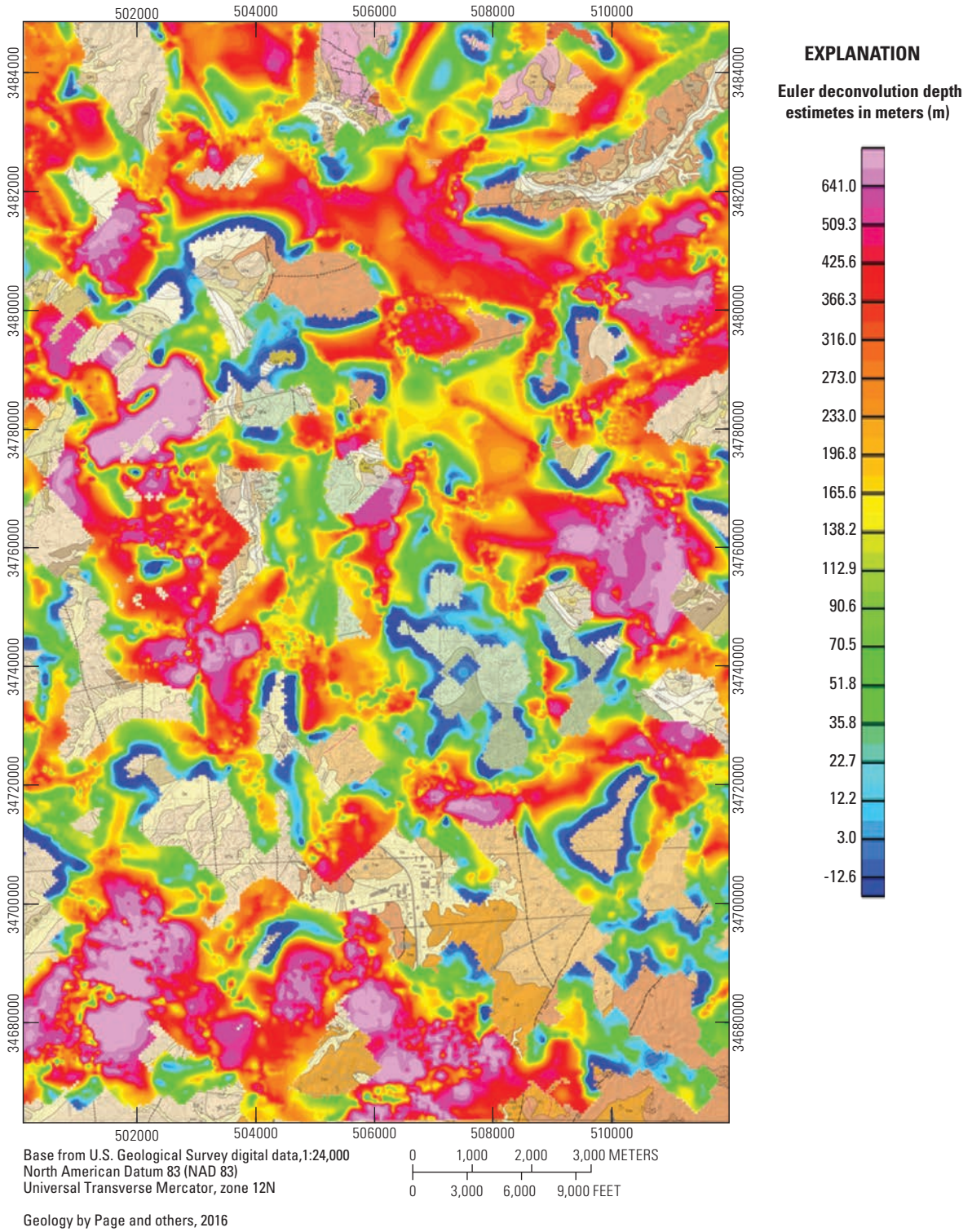

Figure 8. Map showing gridded Euler deconvolution depth estimate solutions using a structural index of 0.5 in the upper Santa Cruz Basin study area plotted over basin geology from Page and others (2016).

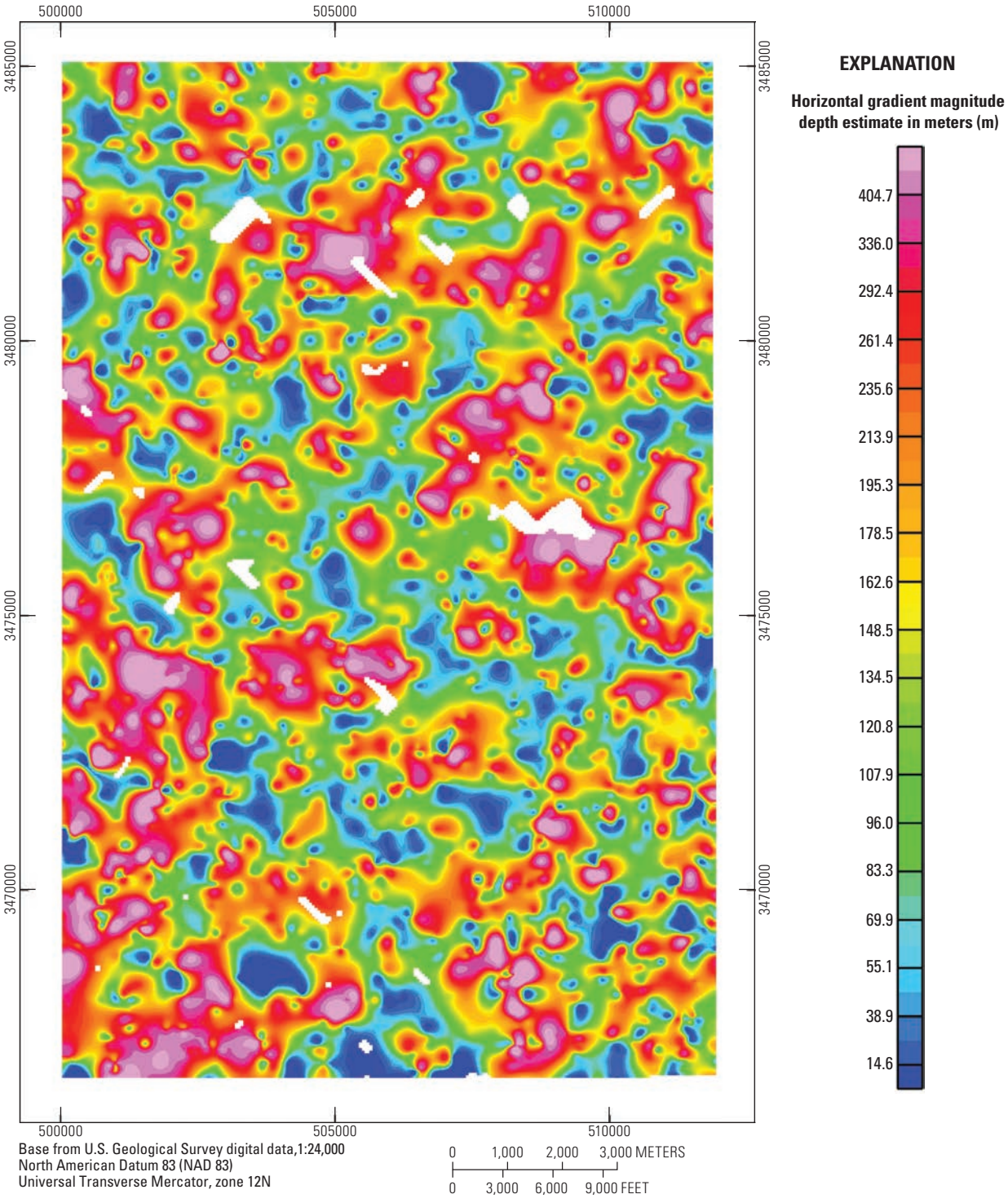

Figure 9. Map showing horizontal gradient magnitude depth estimate grid in upper Santa Cruz Basin study area. White areas indicate no depth estimate solution.

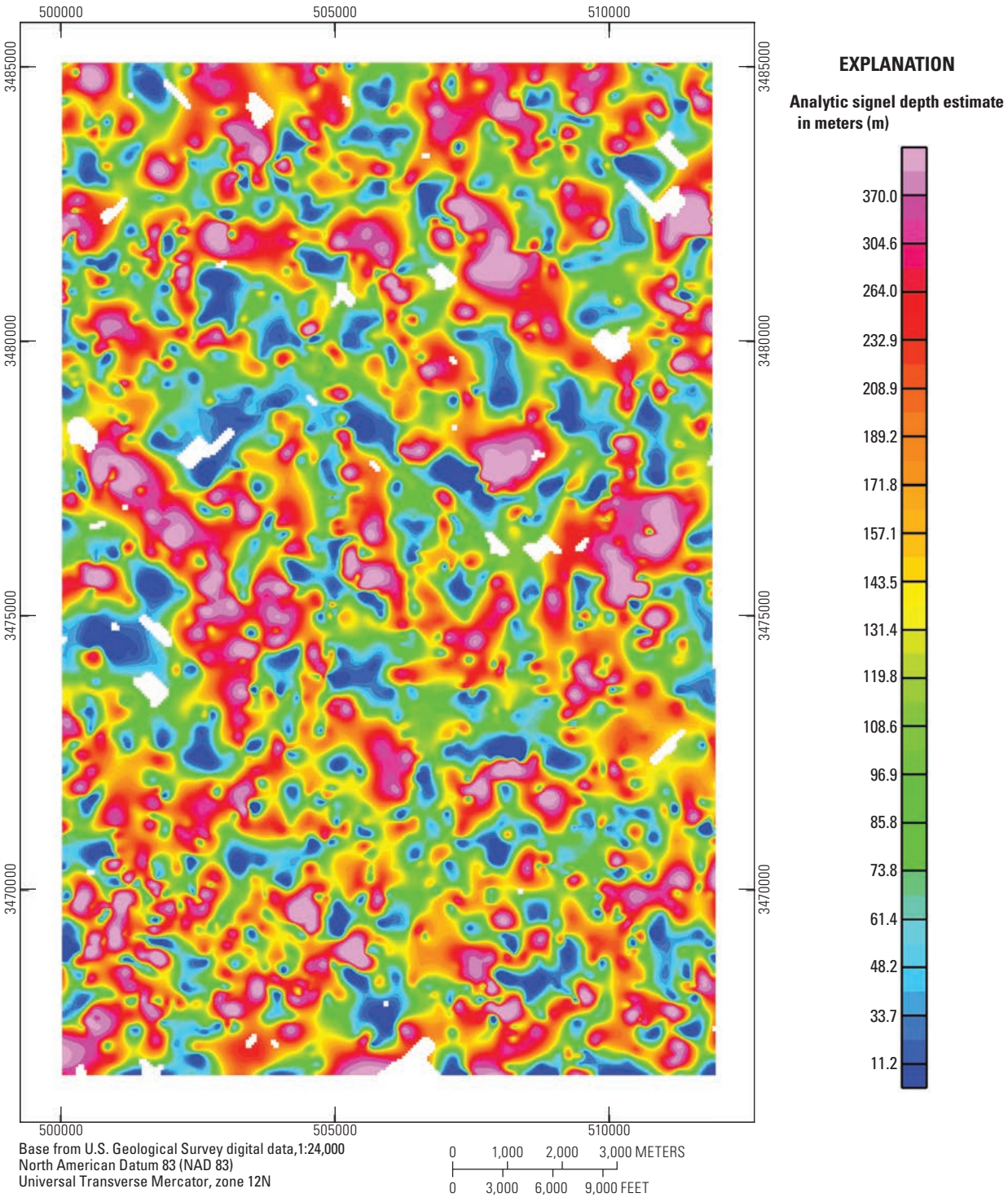

Figure 10. Map showing analytic signal depth estimate grid in upper Santa Cruz Basin study area. White areas indicate no depth estimate solution.

One final step was taken in the preparation of the depth to bedrock map. There are two areas of bedrock with known reversed natural remanent magnetism. One is located at the northeast part of the study area and includes map unit Tghu (table 1, the upper unit of the Grosvenor Hills volcanics). The other is the south central portion of the study area along the Mexican border (map unit Kd, an Upper Cretaceous diorite, table 1). The strong aeromagnetic lows associated with each of these lithologies can be seen on the aeromagnetic anomaly map, figure 6. Since all depth estimates of aeromagnetic data are affected by reversed natural remanence, the gravity based depth to bedrock estimates from Gettings and Houser (1997) were used in these regions. The areas where the gravity based estimates are used were subjectively chosen and were based on where it appeared the reversed rocks controlled the anomaly in the aeromagnetic anomaly data (fig. 6).

Figure 11 displays the sources of techniques used to produce the final depth to bedrock dataset, with depth to bedrock contours added. Where aeromagnetic data were used to estimate depth the Euler deconvolution method typically has priority in the deepest parts of the basin. These estimates are often close to the estimates produced by Gettings and Houser, 1997, displayed in figure 3. The horizontal gradient depths seem to be found in the more shallow areas of the basin and the analytic signal depths seem to be found in the areas of intermediate depths. The complex relationships depicted by the intermixing of the green and blue areas indicate that there is not a lot of difference in depth estimates between the horizontal gradient method and the analytic signal method. They are both similar complex surfaces that cross each other quire often.

Figure 12 displays the combined aeromagnetic depth estimates with the gravity depth estimates of Gettings and Houser (1997) described above. In addition, areas of outcropping bedrock were filled in black because depths to bedrock estimates are meaningless in these areas. Several features on this map stand out and are described below that are tied to locations labeled on figure 12. Again, these are simply random features that appear interesting in figure 12. More observations about this data could be made.

Location A, Bedrock depth greater than 700 m in this area correlates with similar depth estimates based on the gravity dataset (fig. 3). Location B, Scattered bedrock highs in this region are in contrast to the deeper portion of the gravity based depth to bedrock map in fig. 3. Location C, The gravity and aeromagnetic depth estimates fit together well in this region. Location D, Deep bedrock in this area near outcropping map unit Jbm (figs. 3 and 4). Location E, Poor transition from gravity based depth estimates to aeromagnetic based depth estimates in this region. Gravity based estimates come from only a small number of gravity stations (fig. 4) in this area. Also, bedrock structure is complex and basalt flows are known to exist interbedded in the southeast part of the study area in Nogales formation sediments in this region. Basalt can have high magnetic susceptibility (fig. 13) and very high Koenigsberger ratios (fig. 14) and can strongly influence the magnetic field. Location G, Complex bedrock morphology exists in this region. Location H, Gravity and aeromagnetic depth estimates are similar in this region. This is another region of relatively thick basin sediments. Location I, Somewhat good agreement between gravity based and aeromagnetic based depths in this region. The aeromagnetic depths are somewhat deeper. Location F, “Highway 82 microbasin” of Culbertson and others (2010): magnetic depth estimates predict a microbasin, as do Culbertson and others (2010), using ground based time-domain electromagnetic (TEM) methods. The contradictory shallow depths predicted by gravity data (fig. 3) are probably due to lack of data (a single gravity station and potentially an inaccurate measurement) in this region (fig. 5). It should be noted that indicated basin depths here could be caused by reversed magnetic remanence and (or) incorrect interpretation of TEM data. More gravity data need to be acquired to verify the presence of this basin. Location G, Complex bedrock morphology exists in this region. Location H, Gravity and aeromagnetic depth estimates are similar in this region. This is another region of relatively thick basin sediments. Location I, Somewhat good agreement between gravity based and aeromagnetic based depths in this region. The aeromagnetic depths are somewhat deeper than the gravity based estimates.

Two-Dimensional Forward Modeling of Aeromagnetic Data

Two-dimensional forward modeling of Earth’s magnetic field data for six geologic cross sections was done to test the plausibility of the depth to bedrock map in figure 12. Since rocks with reversed natural remanent magnetism are found in the study area, remanent magnetic data from nearby rocks of similar age were used as proxy data. These models are very sensitive to the parameters used in the modeling. Any changes in magnetic susceptibility or remanence as well as the orientation of faults and contacts can make substantial differences in the models. But successful modeling using reasonable parameters and geologic considerations indicates that modeled basin depths that we calculated are plausible for the study area.

The magnetization of a rock mass, J (magnetic dipole moment per unit volume,) is equal to the vector sum of the induced field, Ji, and the natural remanent magnetic field, Jr, that is;

$$J = J_i + J_r \quad (1)$$

The 1996 Patagonia aeromagnetic survey measures the magnitude of this resultant vector, |J| (called the magnetic intensity). Few investigators, however, have included natural remanent magnetism as a contributing factor to studies of continental magnetic anomalies (Bultman, 2014; Morris and others, 2007). Not all susceptibilities, nor remanences, are known for the study area. We therefore used estimates of the Koenigsberger ratio to derive an apparent susceptibility for magnetic rocks in the study area, and subsequently modeled the rocks based on this apparent susceptibility.

For rocks with a remanent magnetism aligned in the direction of Earth’s present day magnetic field a measure of

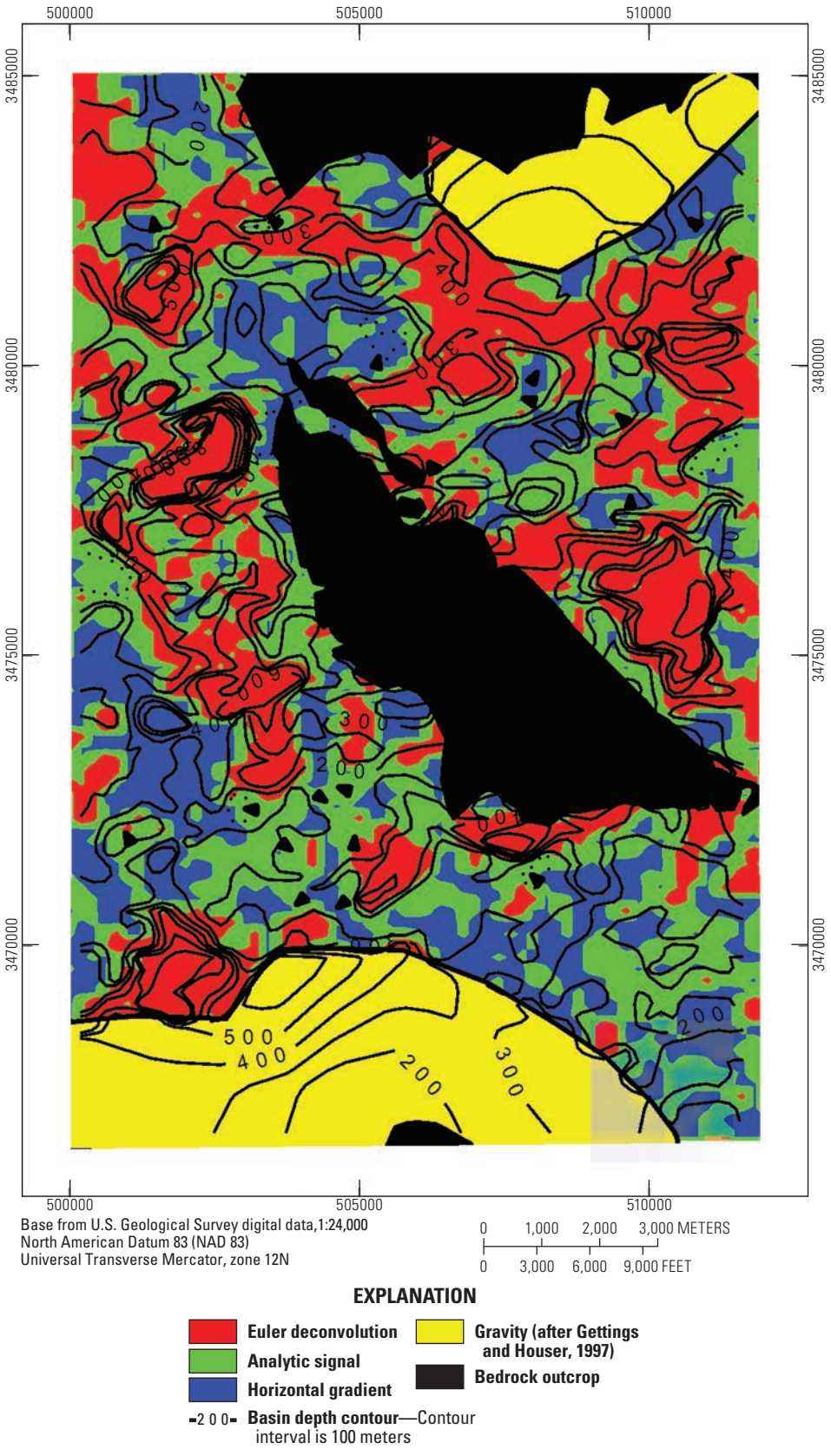

Figure 11. Map showing sources of techniques used for depth to bedrock map in upper Santa Cruz Basin study area. The horizontal gradient depths seem to be found in the more shallow areas of the basin and the analytic signal depths seem to be found in the areas of intermediate depths. The Euler deconvolution method only provided depth solutions over parts of the basin and these were generally confined to deeper portions of the basin. Areas of outcropping bedrock were filled in black because depths to bedrock estimates are meaningless in these areas.

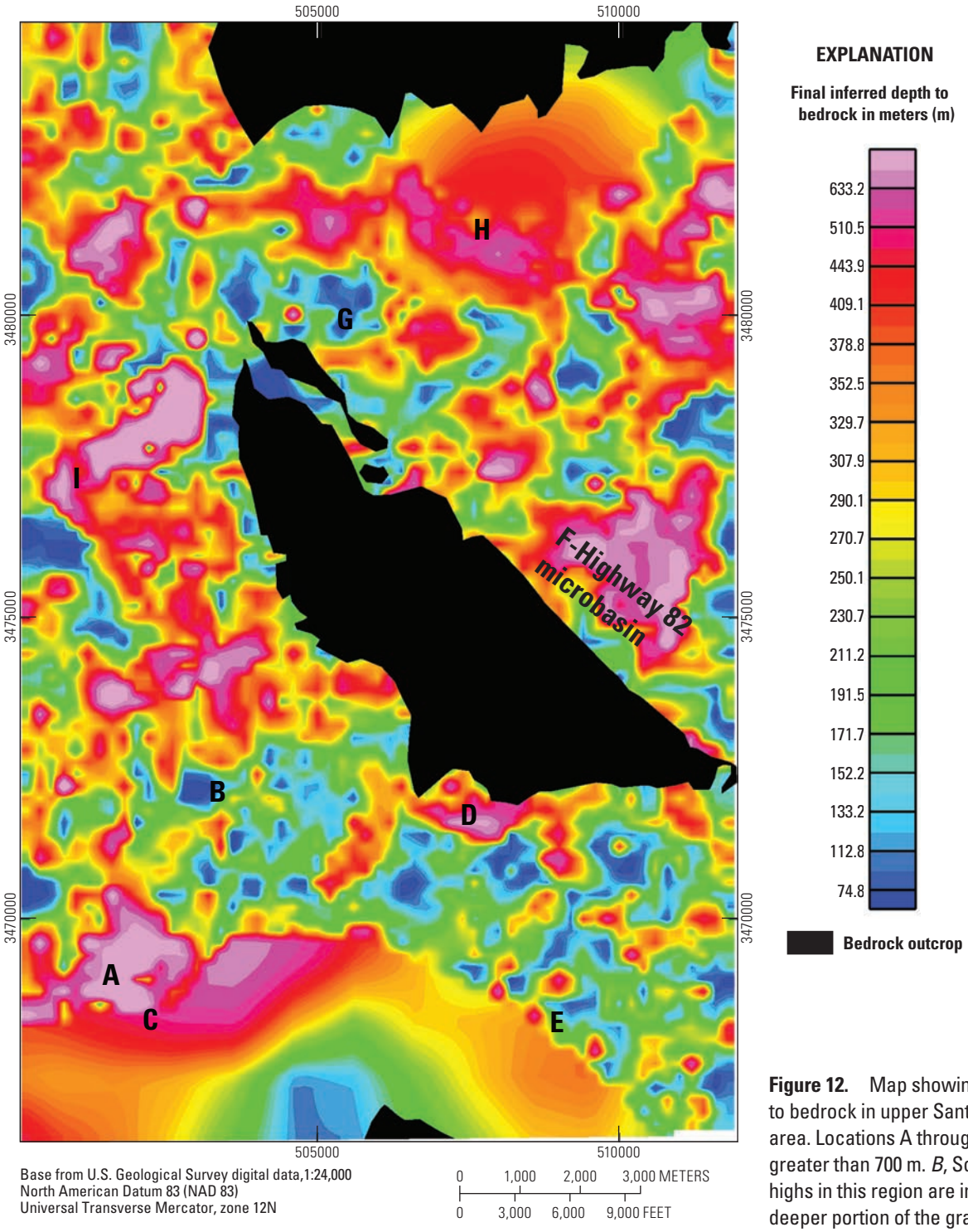

Figure 12. Map showing final inferred depth to bedrock in upper Santa Cruz Basin study area. Locations A through I: *A*, Bedrock depth greater than 700 m. *B*, Scattered bedrock highs in this region are in contrast to the deeper portion of the gravity based depth to bedrock map in fig. 3. *C*, The gravity and aeromagnetic depth estimates fit together well in this region. *D*, Deep bedrock in this area near outcropping map unit Jbm. *E*, Poor transition from gravity based depth estimates to aeromagnetic based depth estimates in this region. Estimates come from only a small number of gravity stations in this area and bedrock structure is complex and basalt flows are known to exist interbedded in the southeast part of the study area in Nogales formation sediments in this region. *F*, "Highway 82 microbasin" of Culbertson and others (2010). Magnetic depth estimates predict a microbasin, as do Culbertson and others (2010), using ground based time-domain electromagnetic (TEM) methods. *G*, Complex bedrock morphology in this region. *H*, Gravity and aeromagnetic depth estimates are similar in this region. *I*, Somewhat good agreement between gravity based and aeromagnetic based depths in this region. Areas of outcropping bedrock were filled in black because Euler deconvolution depths to bedrock estimates are meaningless in these areas.

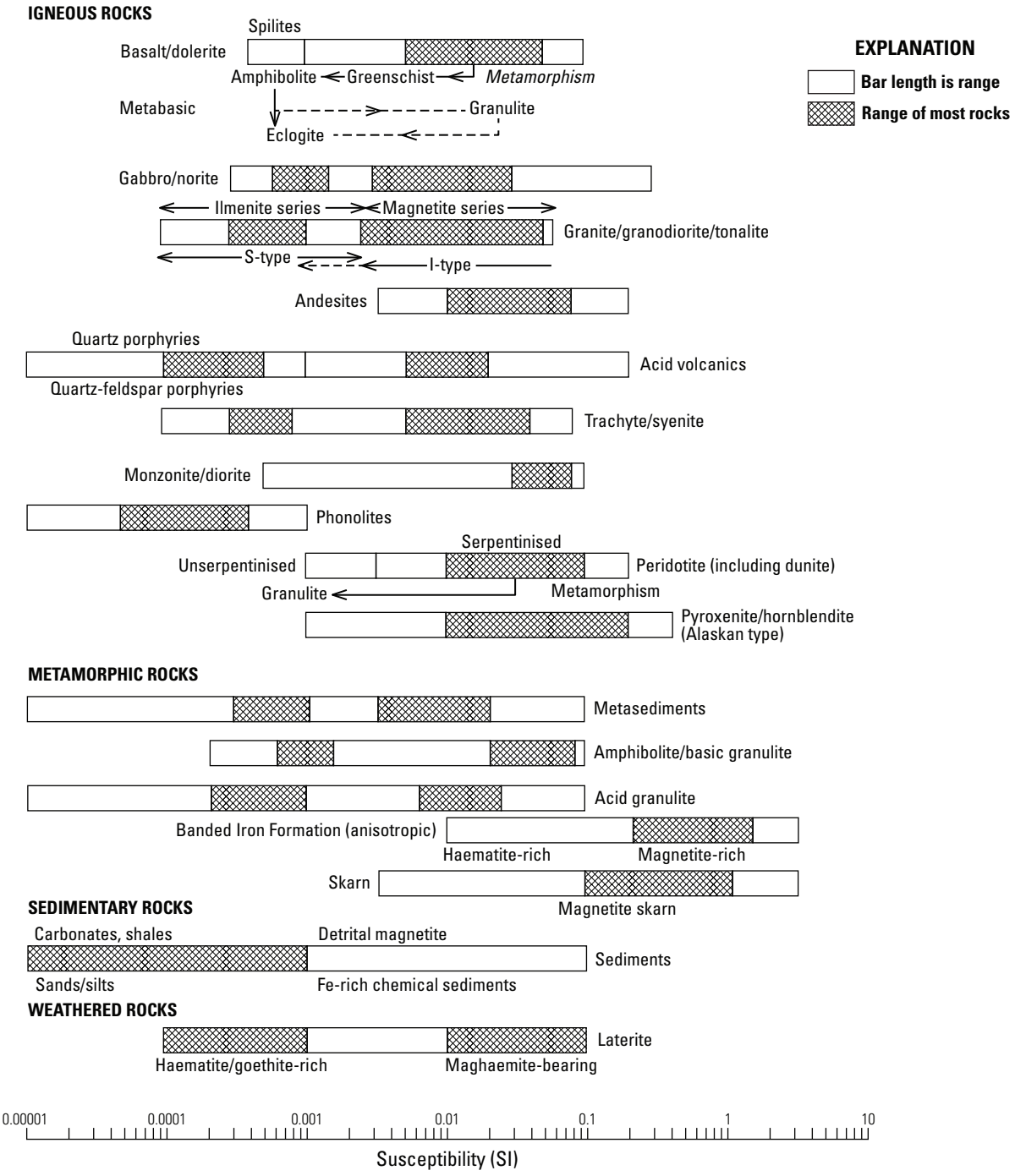

Figure 13. Graph showing magnetic susceptibility of common rocks (after Clark, 1997).

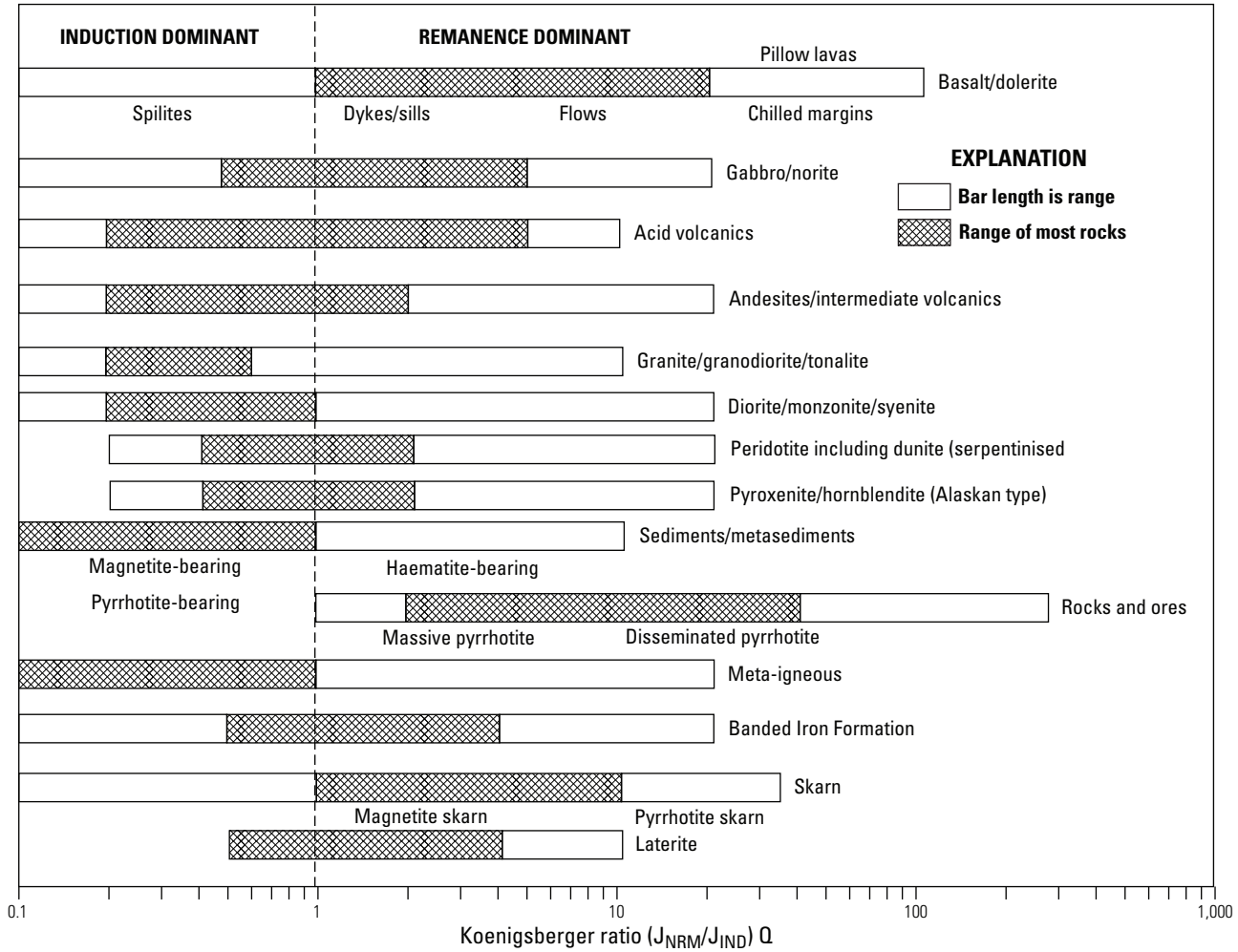

Figure 14. Graph showing Koenigsberger ratio of common rocks (from Clark, 1997). J_{NRM}, natural remanent magnetization of a rock mass; J (magnetic dipole moment per unit volume); J_{IND}, induced magnetization of a rock mass.

apparent susceptibility was created that includes magnetization components from both the induced and remanent fields. For sufficiently weak fields, such as the Earth's magnetic field, the induced magnetization, J_i, of a material is approximately proportional to and parallel to the applied field with the constant of proportionality known as the magnetic susceptibility, k (Clark, 1997). Therefore the induced component of the total magnetization is equal to:

$$J_i = kF \quad (2)$$

where F is the magnitude of the Earth's internal field in amperes per meter (A/m).

The Koenigsberger ratio, Q, (Koenigsberger, 1938a and 1938b) is the ratio of the remanent magnetization to the induced magnetization for a rock mass, $| J_r | / | J_i |$.

The total magnetization of a rock,

$$J_T = J_i + J_r \quad (3)$$

can be used to calculate the apparent susceptibility when the Koenigsberger ratio, Q, is known or estimated and the angle between the remanent field and the Earth's (inducing) field (α) is known or estimated since

$$Q = | J_r | / | J_i | \quad (4)$$

then:

$$J_T = k\,F + Q\,|J_i| \quad (5)$$

$$J_T = k\,F + Q\,k\,F\cos(\alpha) \quad (6)$$

$$k_a\,F = k\,F + Q\,k\,F\cos(\alpha) \quad (7)$$

$$k_a = k + Q\,k\cos(\alpha) = k\,(1+Q\cos(\alpha)) \quad (8)$$

where:

JT = Earth's total magnetic field in per meter (A/m)
k = magnetic susceptibility
k_a = apparent magnetic susceptibility adjusted for rock remanence
Q = Koenigsberger ratio
F = magnitude of the Earth's internal field in amperes per meter (A/m)
α = angle between the remanent field and the Earth's (inducing) field

The apparent susceptibility calculated in equation 8 can then be used in place of the measured susceptibility to include both the induced field and the remanent field. Figure 13 displays the magnetic susceptibilities, k, for several types of rock and figure 14 displays the Koenigsberger ratio, Q, for several types of rock. In this modeling, Q is estimated from figure 14 and α is assumed to be 30°, somewhat closely aligned to the present day magnetic field. While this number could vary dramatically based on the age of the rock in question and tectonic movements since the remanent magnetism was frozen into the rock, 30° was chosen because it is reasonable for a wide range of rock ages. Though these assumptions may not be appropriate for mapping the actual lithology at the bottom of the basin, they are sufficient for demonstrating that the depth to bedrock map is one possible model of the depth to bedrock. Using this approximation allows a better representation of the magnetic intensity in rock than simply using magnetic susceptibility and this assumption works with any orientation of the remanent magnetic field.

The remanent magnetic intensity must still be estimated for these rocks by using estimated Q values for specific lithologies based on figure 14 and on the relationship:

$$|J_r| = |J_i| \times Q = k \times F \times Q \quad (9)$$

At the time of the survey, F = 38.41 A/m and it will be used to generate the remanent intensity since the field strength at the time the remanence was preserved is unknown. For example, map unit Kd (diorite, table 1) has measured k = 0.006 SI (table 1). Based on Elephant Head igneous rocks of roughly the same age (Hagstrum, 1994) and found about 40 km north, map unit Kd is given a remanent magnetic inclination of –48.2° and declination of 165°. As a diorite, Q for map unit Kd is estimated at 1.3, just on the high side of the common range of rocks. The estimated remanent intensity of Kd, J_r, is then 0.006 × 38.41 A/m × 1.3 = 0.3 A/m. Other remanent intensities were calculated in a similar fashion and are given in table 1.

Using map unit Jb (table 1) as an example, k (table 1) was measured in the field at 0.007 SI. Based on the lithology of map unit Jb (biotite-hornblende quartz monzonite, table 1) the estimated Koenigsberger ratio (Q_e) for this composition of rock varies from 0.1 to 10 with most values ranging from 0.2 to 0.6 (fig. 14). Q_e was chosen to be 0.6 since the composition of map unit Tghu is on the more mafic end of the rock compositions used in figure 14. The apparent susceptibility, k_a, for map unit Jb is then 0.007 + (0.60×0.007×cos(30°)) = 0.01 SI.

For rocks with known reversed remanent magnetic field, published remanent vectors for rocks in the region with similar ages were found. These remanent vectors and the sources of their estimations are displayed in table 1.

Modeling in these geologic cross sections was based on matching the calculated results of a two-dimensional forward magnetic model over a profile to the observed aeromagnetic data over the same profile. The magnetic properties for lithologies used in the modeling are given in table 1. The morphology of the bedrock-basin fill contact in all profiles was obtained from the depth to bedrock map (fig. 12) and is used as the starting point for bedrock depth in the modeling. For all modeling, Tertiary and Quaternary basin fill is lumped together into one basin fill unit, for convenience referred to as the Tertiary Nogales Formation (Tn, table 1), although it includes more units than the actual Nogales Formation. The location of all mapped contacts and faults were entered into the models and held to their mapped locations. Mapped exposed lithologies were entered into the model, and potential bedrock lithologies were chosen based on nearby exposed lithologies. Models were started by choosing concealed lithologies that made geologic sense and had appropriate apparent susceptibilities. As modeling progressed, apparent susceptibility was changed as needed, including creating a reversed remanent Earth's magnetic field if necessary. If the susceptibility was a closer match to another rock type, that rock type was used in the model. Bedrock depths were changed very little from the initial depth to bedrock map estimates and only modified in a few cases.

The locations of the six two-dimensional models coincide with the profiles and geologic cross sections from the study area geologic map (Page and others, 2016). The four northernmost profiles and cross section models were truncated by a few hundred meters on their west sides. The locations of these profiles and corresponding geologic cross section models are displayed in figure 15. The models (figs. 16–21) are plotted below the geologic map area corresponding to their location to better see relationships between the geologic map and the cross section models. The modeling was done using the GM-SYS profile modeling extension in the Oasis montaj geophysical analysis software (Geosoft, 2015).

- Profile *A–A′*, figure 16:

The geologic cross section from forward magnetic anomaly modeling of profile *A–A′* in figure 16 has no outcropping bedrock. Map unit Jb (fig. 4) will be used as the main bedrock unit in this area due to its outcrop just to the south of the profile in the Mt. Benedict Horst block (fig. 1). Fitting a model using the assumptions and estimates previously described required the addition of a reversely magnetized geologic body in the subsurface to account for the negative anomalies found in the profile. The Tertiary Grosvenor Hills volcanics (map unit Tghu, table 1) outcrops to the north of this profile and is known to be reversed and is therefore a plausible unit to include in the cross-section. When a 500 m (or more) thick unit of reversely magnetized Tertiary

Table 2. Electrical properties of some geologic materials (after Rubin and others, 1999)

[S/m; Siemens per meter; CDT, conductivity-depth transform]

Material	Resistivity (ohm-m)	Conductivity (S/m)	CDT values
dry sand	10^3 to 10^7	10^{-3} to 10^{-7}	–3 to –7
saturated sand	10^2 to 10^4	10^{-2} to 10^{-4}	–2 to –4
silts	10^2 to 10^3	10^{-2} to 10^{-3}	–2 to –3
shales	10 to 10^3	10 to 10^{-3}	–1 to –3
clays	1 to 10^3	1 to 10^{-3}	0 to –3
sandy soil (dry)	7,100	1.4 e10^{-4}	–3.85
saturated sandy soil	150	6.7 e10^{-3}	–2.17
clayey soil	3,700	2.7 e10^{-4}	–3.57
saturated clayey soil	20	5.0 e10^{-2}	–1.3
granite	10^3 to 10^5	10^{-3} to 10^{-5}	–3 to –5

Grosvenor Hills volcanics is placed on top of map unit Jb in most locations, the morphology of the bedrock surface and the mapped structure (faults) can be modeled successfully. It should be noted that there are no exposed relationships between the Grosvenor Hills volcanics and map unit Jb, but that does not preclude this relationship from occurring. Gettings, 2002, indicates that flows of the Salero Formation can have both normal and reversed remanent magnetism. To the west of the Mt. Benedict fault (fig. 2), a reversely magnetized volcanic component of Cretaceous Salero Formation (map unit Ks, table 1) is used to match the observed negative magnetic anomaly on the west side of the aeromagnetic profile. Map unit Ks was chosen due to its proximity to the cross-section, outcropping just to the north of profile *A–A′* and along the Mt. Benedict fault to the south.

Two locations on figure 16 are labeled as location 1 and location 2. At these locations the model does not fit the aeromagnetic data well and modeling could not be improved using the rocks that have been chosen in these models (those in table 1). Therefore this model mismatch could be due to a questionable depth to bedrock estimate or complex geologic relationships with unknown rocks with unknown susceptibilities and remanent magnetisms. In addition, at location 2 bedrock configuration to the east of the profile may also contribute to the problem.

- Profile *B–B′*, figure 17:

The cross-sectional model for profile *B–B′* (fig. 17) has map unit Jb (fig. 4) outcropping near the center of the profile. To the east of this, the profile is similar to profile *A–A′* and uses the known reversely magnetized Tertiary Grosvenor Hills volcanics (map unit Tghu, table 1) to account for anomaly lows. To the west, the calculated depth to the top of the bedrock is very deep, dropping to over 900 m depth, but the model works well. Problems fitting the model near the edges are probably due to edge effects, which include influences of geology beyond the model boundaries.

- Profile *C–C′*, figure 18:

A large portion of the center of the profile *C–C′* (fig. 18) is occupied by the outcropping map unit Jb (table 1). The low measured susceptibility (table 1) of this lithology does not generate an anomaly that matches the observed anomaly. Therefore it is likely that this measurement is not representative of the unit. In fact, we hypothesize that the unit Jb may also contain reversely magnetized rocks. This could have been a separate phase of the intrusive emplaced during a period of reversed Earth's magnetic field polarity or a portion of the original intrusive's remanent magnetism could have be reset when the Late Tertiary intrusive adjacent to it was emplaced. We assume remanent directions from Jurassic rocks in the nearby Canelo Hills (table 1). Applying this hypothesis allows us to fit the data as shown (fig. 18). This hypothesis could be tested using oriented magnetic samples along the outcrop of Jb.

The concealed lithology chosen on the west side of the profile is the reversely magnetized map unit Jg (table 1). This unit outcrops extensively in the region, especially to the east, and is also important in modeling profile *D–D′*. Map unit Ti, with reversed natural remanent magnetic polarity, was used on the east of the Mt. Benedict fault (fig. 2) to help create the relatively low magnetic values observed in this region. This unit by itself, however, was insufficient to generate the relatively low magnetic values observed. Therefore, given the rest of the assumptions made about rock magnetism, the eastern part of the outcropping map unit Jb had to have a reversed natural remanent magnetic field, and was modeled as previously described.

The bedrock depression at location 1 in figure 18 (UTM, zone 12 north, 502000E) cannot be modeled easily. Either there is complex geology at this location or the bedrock depth is wrong.

- Profile *D–D′*, figure 19:

Bedrock in profile *D–D′* (fig. 19) is completely concealed, but it is assumed that map unit Jbm (table 1), which

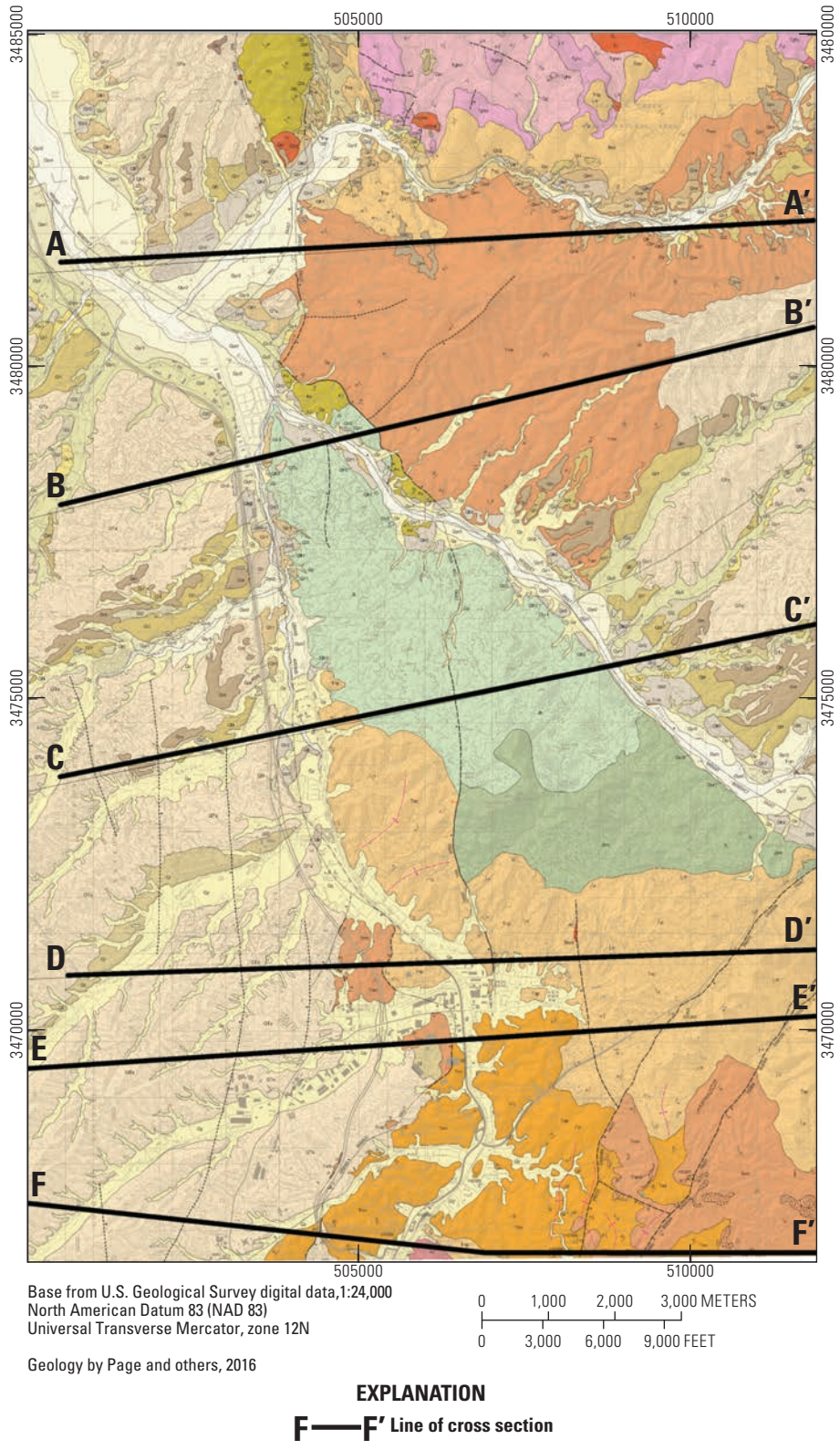

Figure 15. Map showing locations of cross sectional profiles for forward modeling of Earth's magnetic field data.

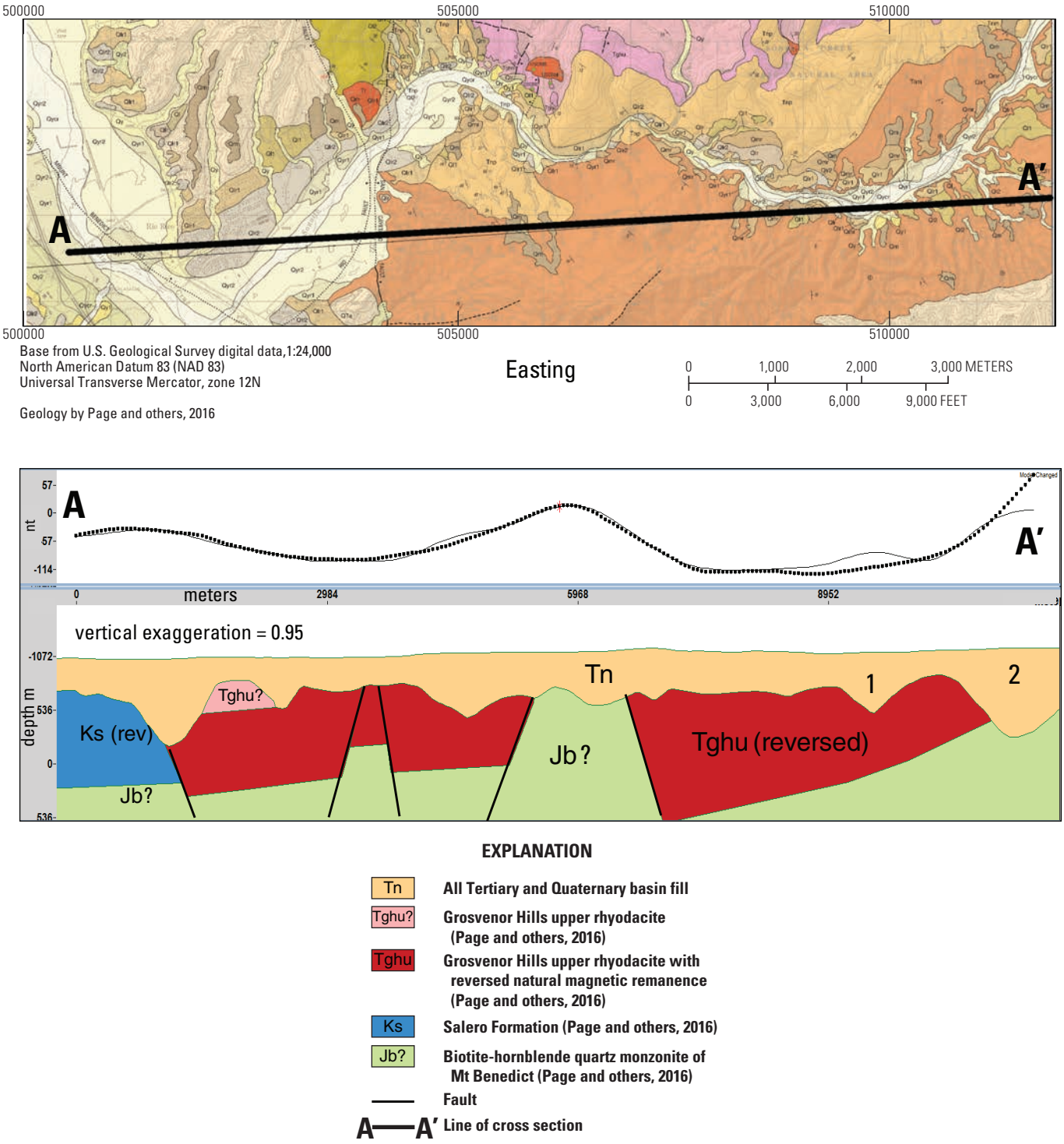

Figure 16. Geologic cross section based on Earth's magnetic field forward model for profile *A*–*A'*, upper Santa Cruz Basin study area. At locations 1 and 2, the model does not fit the aeromagnetic data well; this model mismatch could be due to a questionable depth to bedrock estimate or complex geologic relationships with unknown rocks with unknown susceptibilities and remanent magnetisms. At location 2, bedrock configuration to the east of the profile may also contribute to the problem. Rev or reversed, reversed remanent magnetism. Map unit labels are shown in table 1 and fig. 4.

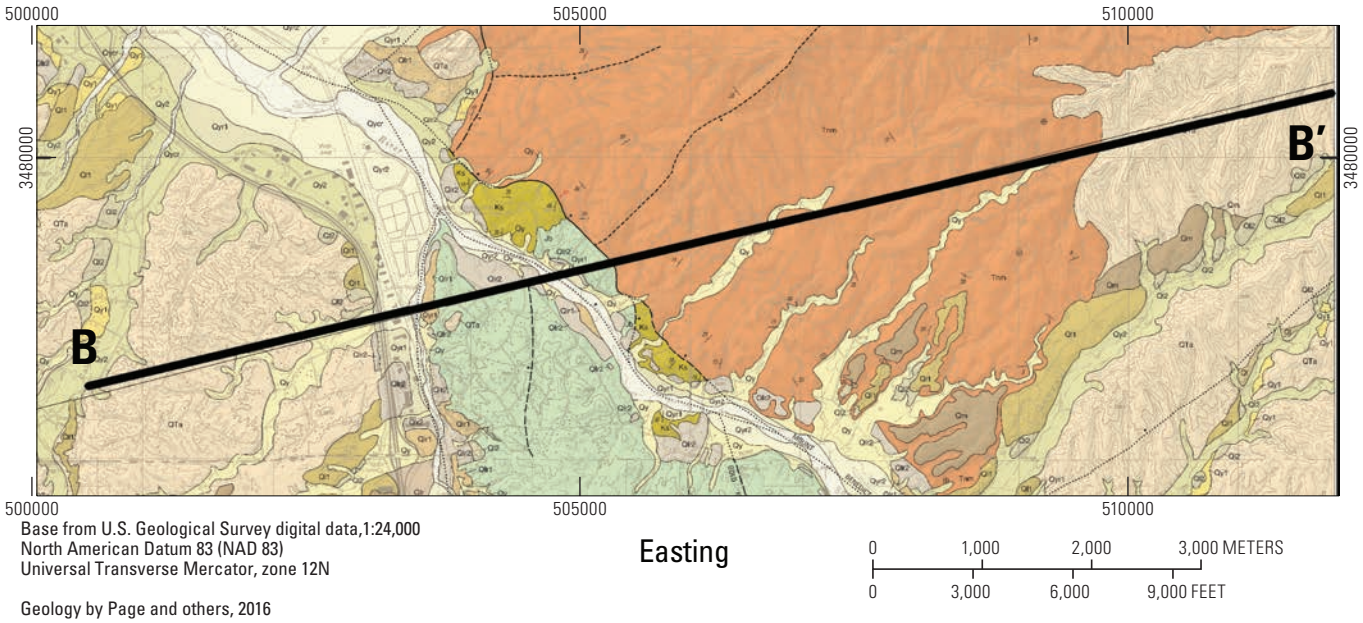

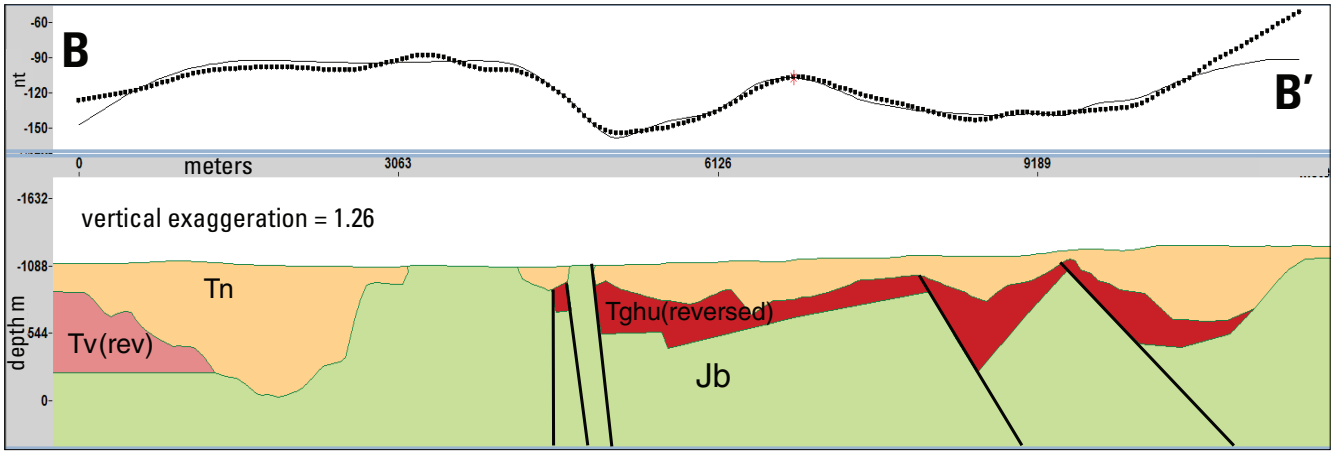

EXPLANATION

Tn	All Tertiary and Quaternary basin fill
Tv	Extrusive andesite and dacite with reversed natural magnetic remanence (Drewes, 1980, 1996; Drewes and others, 2002)
Tghu	Grosvenor Hills upper rhyodacite with reversed natural magnetic remanence (Page and others, 2016)
Jb	Biotite-hornblende quartz monzonite of Mt Benedict (Page and others, 2016)
——	Fault
B——B′	Line of cross section

Figure 17. Geologic cross section based on Earth's magnetic field forward model for profile *B–B′*, upper Santa Cruz Basin study area. Rev or reversed, reversed remanent magnetism. Map unit labels are shown in table 1 and fig. 4.

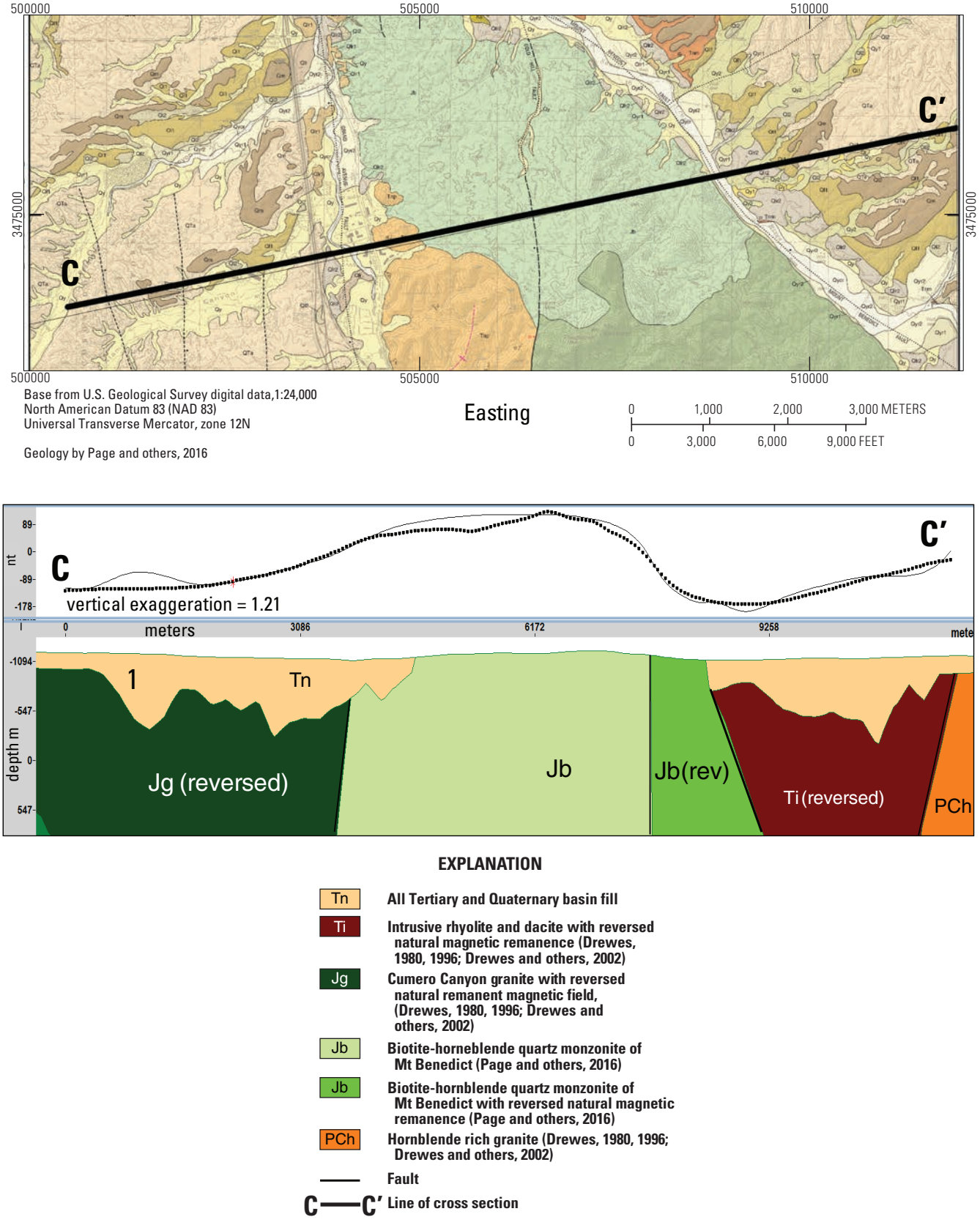

Figure 18. Geologic cross section based on Earth's magnetic field forward model for profile *C*–*C*′, upper Santa Cruz Basin study area. The bedrock depression at location 1 indicates that there is either complex geology, or the depth to bedrock is wrong. Reversed, reversed remanent magnetism. Map unit labels are shown in table 1 and fig. 4.

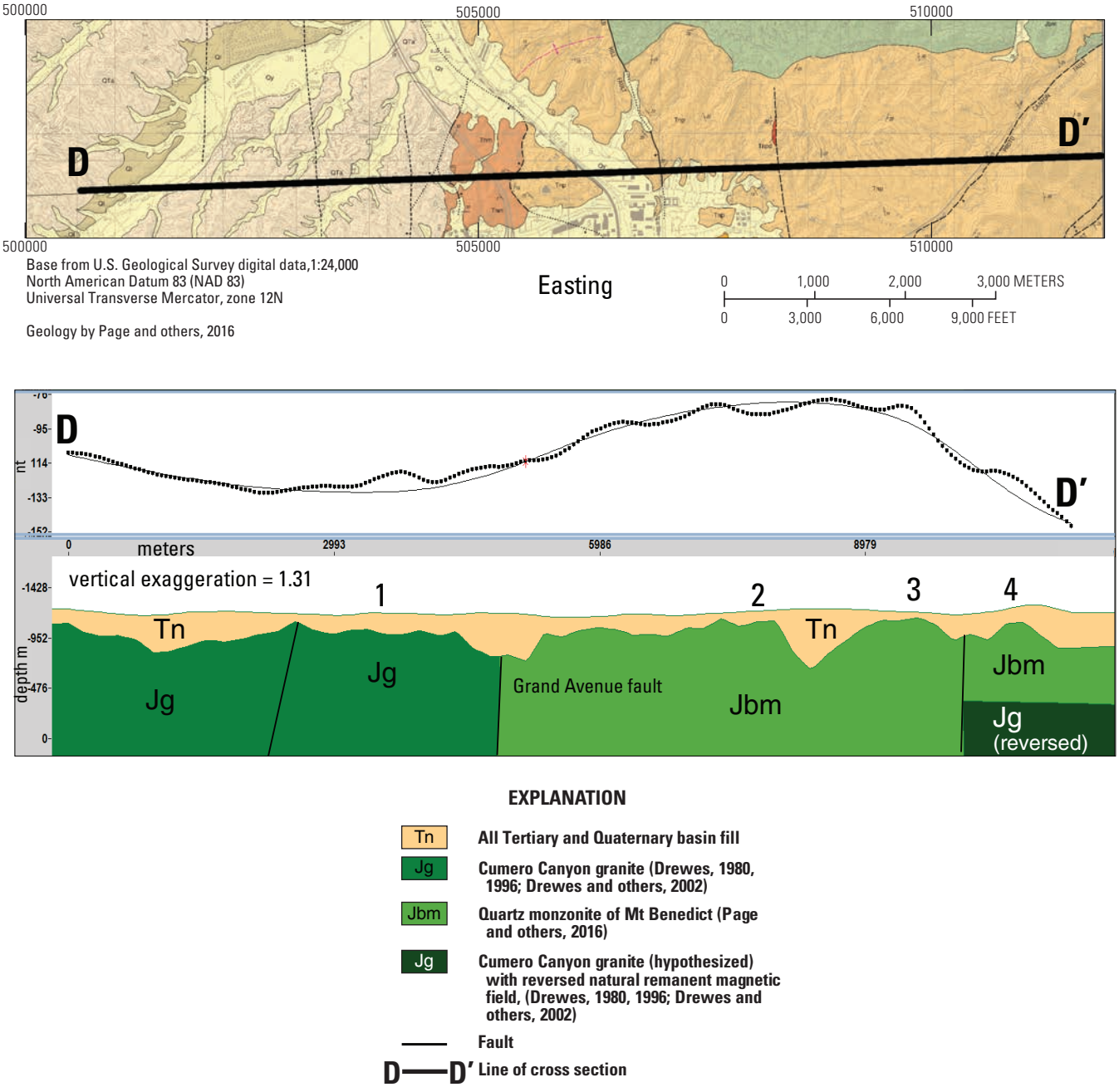

Figure 19. Geologic cross section based on Earth's magnetic field forward model for profile *D–D′*, upper Santa Cruz Basin study area. Hypothesized concealed intrusion is labeled as unit Jg (reversed). The model fits well except for high-frequency misfits at locations 1, 2, 3, and 4. The complexity of the geology at these locations is likely greater than the resolution of the modeled geologic structure, and involves unknown rocks with unknown susceptibilities and remanent magnetisms. Map unit labels are shown in table 1 and fig. 4.

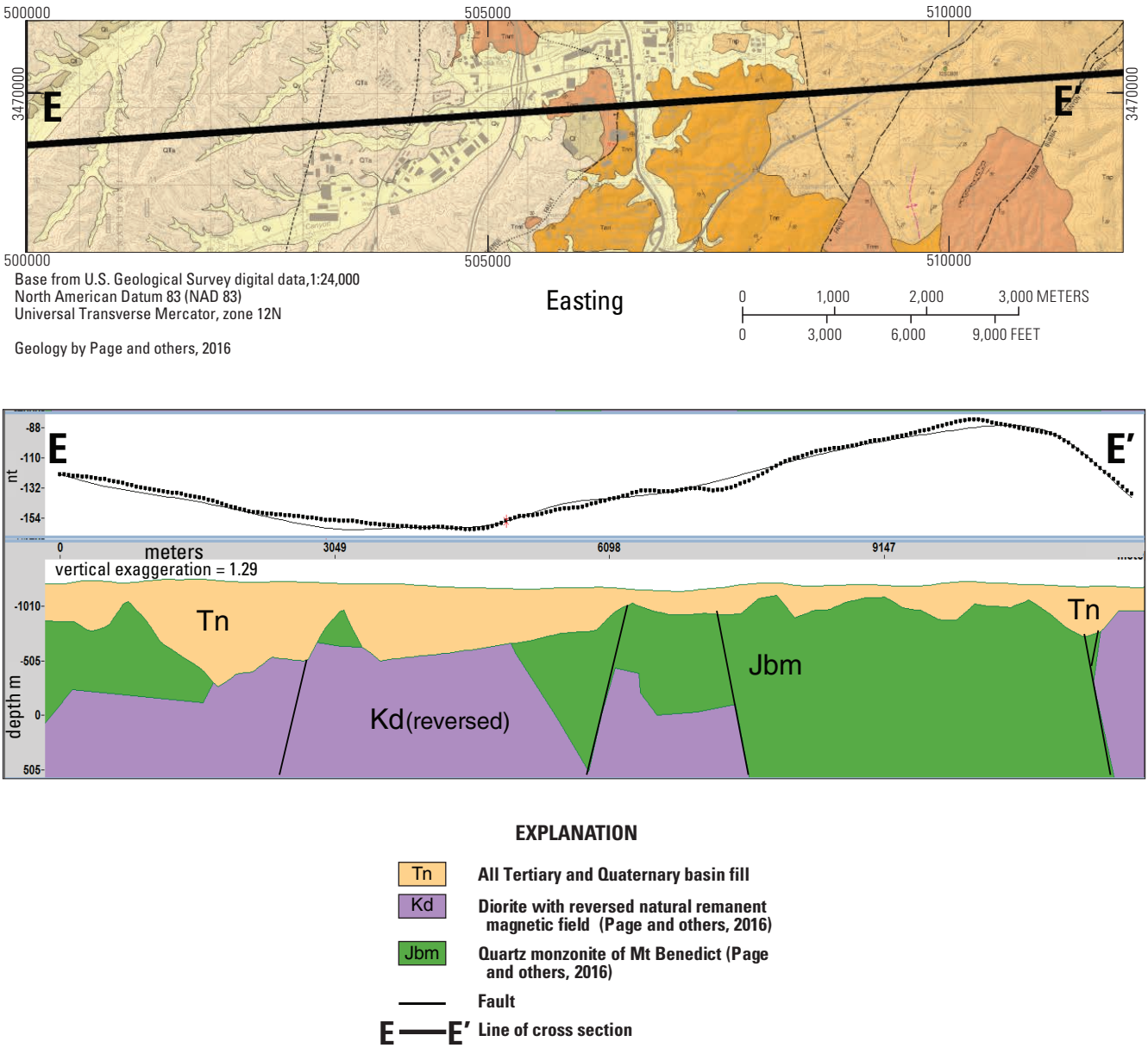

Figure 20. Geologic cross section based on Earth's magnetic field forward model for profile *E–E′*, upper Santa Cruz Basin study area. Rev or reversed, reversed remanent magnetism. Hypothesized concealed map unit is labeled as unit Kd (rev) on the east side of the profile. Map unit labels are shown in table 1 and fig. 4.

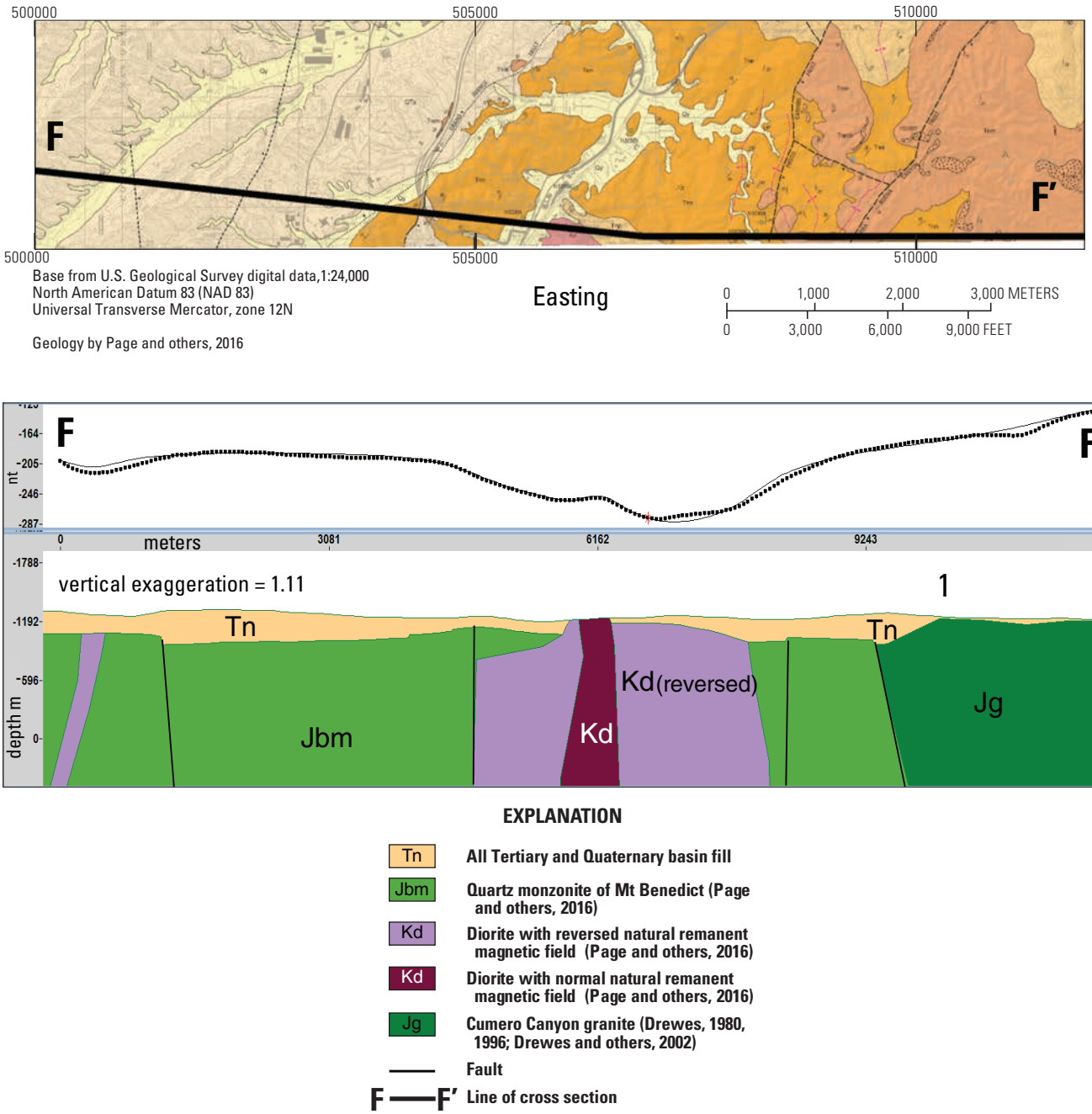

Figure 21. Geologic cross section based on Earth's magnetic field forward model for profile *F–F′*, upper Santa Cruz Basin study area. The transition from gravity-based depth to bedrock to aeromagnetic-based depth to bedrock is seen at location 1. The depths from the aeromagnetic data (to the east of location 1) seem too shallow here based on the topographic relief seen while working in the field in that area. Map unit labels are shown in table 1 and fig. 4.

outcrops just to the north, composes the basement east of the Grand Avenue fault (fig. 3), and Jurassic granite (map unit Jg, table 1) composes the basement west of the fault. Also, due to the large negative anomaly observed on the east end of the profile, a concealed intrusive with a reversed natural remanent magnetism was added. Map unit Jg (with a reversed natural remanent magnetic field, table 1) is a potential candidate due to its extensive outcrop to the east along the western flank of the Patagonia Mountains (Drewes, 1982). The model fits rather well except for high-frequency misfits at locations labeled with 1, 2, 3, and 4. As in figure 16, the complexity of the geology at these locations is likely greater than the resolution of the modeled geologic structure and it involves unknown rocks with unknown susceptibilities and remanent magnetisms.

- Profile *E*–*E*′, figure 20:

Bedrock in profile *E*–*E*′ (fig. 20) is completely concealed. The magnetic anomalies of this profile can be modeled quite well using map unit Jbm (table 1), which is exposed to the north. Bedrock unit Kd, with a reversed natural remanent magnetic field (table 1) is exposed at the surface to the south of the profile, but is only found at depth on the western side of the profile. A reversely magnetized unit is suggested on the far eastern side of the profile to account for the large negative anomaly observed in that region. We have assumed map unit Kd is the source of the negative anomaly.

- Profile *F*–*F*′, figure 21:

The only exposed bedrock in profile *F*–*F*′ (fig. 21) is a small outcrop of map unit Kd in the center of the profile. While map unit Kd has a reversed natural remanent magnetic field, the small positive anomaly at UTM 505800E requires a non-reversed phase of the intrusive to be properly modeled. Map units Jbm and Jg (table 1) are modeled in the rest of the profile. The transition from gravity-based depth to bedrock to aeromagnetic-based depth to bedrock is seen at location 1 in figure 21. The depths from the aeromagnetic data (to the east of location 1) seem too shallow here based on the topographic relief seen while working in the field in that area. Also, the gravity depths in this area are controlled by only 1 gravity station (fig. 5). More gravity data in this region might help clarify the depth to bedrock in the far eastern portion of this profile.

In general, the depth to bedrock estimates of figure 12 are both reasonable and possible, but should be considered as a model that could be verified by more geophysical work or drilling.

Transient Electromagnetic Data and Analysis

Transient electromagnetic (TEM) surveys use a short (transient) pulse of current in a transmitting loop antenna to induce electric and magnetic fields in the ground. The subsequent decay of the induced electric and (or) magnetic field in the ground is measured. Inversions or transforms of these data can be used to determine subsurface electrical properties. The technique has proven very useful for mineral exploration, groundwater and environmental mapping, and other geoscience related studies (Dickinson and others, 2010; Wynn, 2006; Bultman, 2002; Bultman and others, 1999).

TEM Data

At the request of the USGS an electromagnetic and magnetic survey was flown over parts of south central Arizona by Geoterrex-Dighem (now Fugro, https://www.fugro.com/) from January 8–18, 1998. The survey covered five separate areas and approximately 2,500 line kilometers. These areas are shown using the actual flight line data from the survey and are labeled in figure 22. Area 1 is referred to as Huerfano Butte; Area 3 is Cottonwood Canyon; and areas 2, 4, and 5, are simply called Nogales and vicinity. Most of areas 2 and 5, and a small portion of area 4, lie within the study area (fig. 22). The majority of flight lines in each area have a spacing of approximately 400 m. Additionally there are several tie lines for each area that are flown perpendicular to the main set of flight lines. These are also shown in figure 22.

The data were originally acquired by Geoterrex-Dighem using the GEOTEM multicoil system. This system has a vertical axis transmitter antenna that is 232 square meters (m^2) in area that is flown at a nominal height of 120 m above ground. The transmitter is coiled 6 turns from nose to wingtip to tail to wingtip to nose around a CASA C–212 twin turboprop aircraft. The receiver is a multicoil (X, Y, and Z) system that records at 4 samples per second for 20 channels on each coil. It is towed 125 m behind the center of the transmitter loop at a nominal height of 70 m above ground. The transmitter has a base frequency of 30 Hz, a pulse width of 4,080 microseconds, a pulse delay of 130.2 microseconds and an off time of 12,486 microseconds. Given the large transmitting antenna and a current output of 500 amperes, the system produces a transmitted signal with a dipole moment of 6.96×10^5 ampere meters squared (Am^2). Sample recording window delay times vary from –3,907 to 11,306 microseconds from the end of the pulse. It should be noted that the 1998 Santa Cruz TEM survey data are relatively old technology. For instance, the exact distance between transmitter and receiver is assumed and not measured. Global Positioning System (GPS) navigation is used and the final data are in UTM projection with a North American Datum 1927 (NAD27) datum and using the Clarke 1866 spheroid. Since the data were acquired in a UTM projection with a World Geodetic System 1984 (WGS84) datum, the contractor used a conversion of delta x (easting) of 8 m and a delta Y (northing) of –163 m to transform the data into their final datum form (with a NAD27 datum). For this study, that operation was reversed in order on the data to get them back into WGS84, which closely corresponds to a UTM projection with a North American Datum 1983 (NAD83) datum.

One product included with the data by the contractor was a conductivity-depth transform (CDT) for each flight line. The CDT is a one-dimensional transform developed by Wolfgram

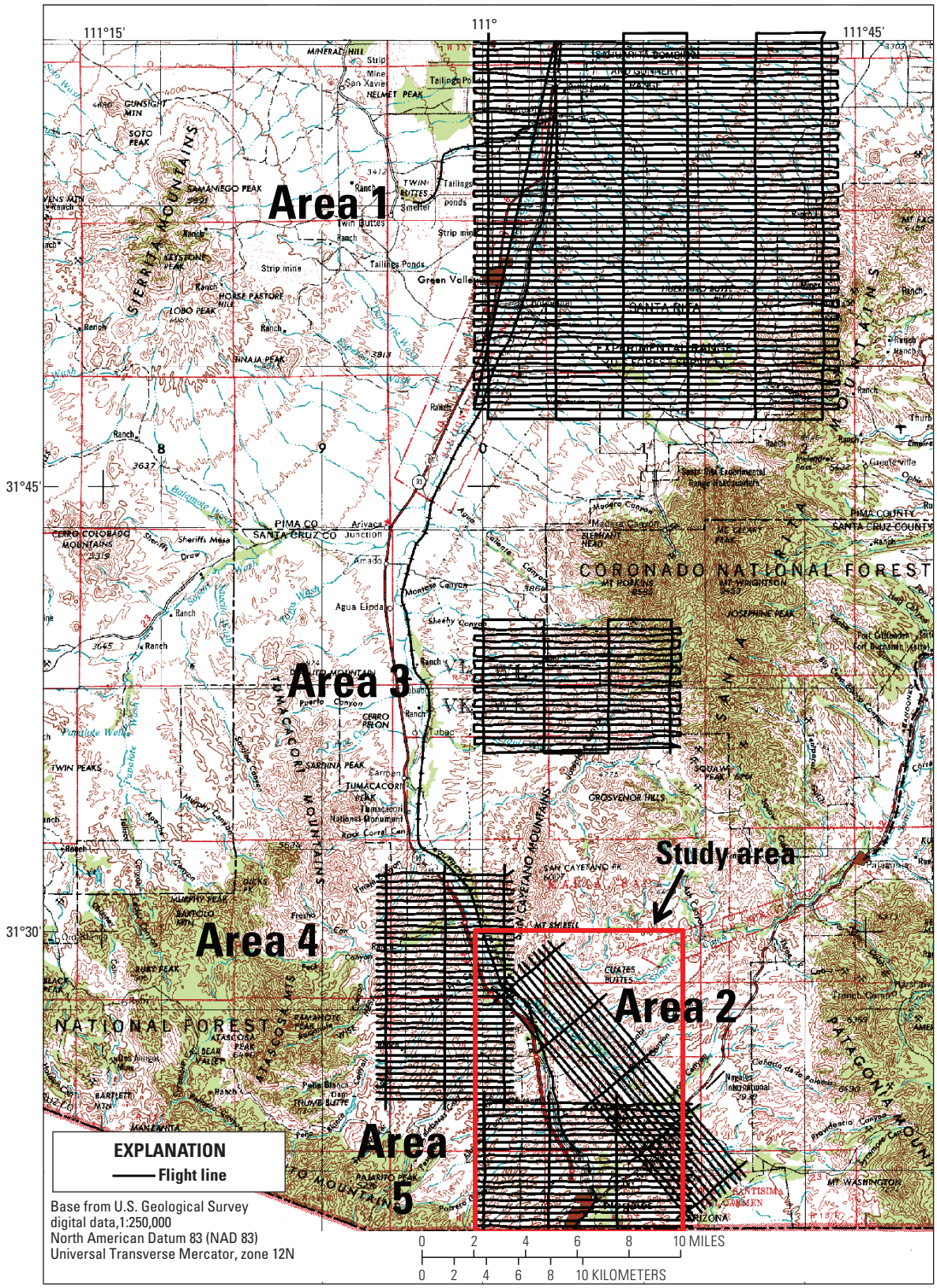
111°15'
111°
111°45'
31°45'
31°30'
Area 1
Area 2
Area 3
Area 4
Area 5
Study area
CORONADO NATIONAL FOREST
NATIONAL FOREST
SIERRITA MOUNTAINS
SANTA RITA MOUNTAINS
TUMACACORI MOUNTAINS
SAN CAYETANO MOUNTAINS
PATAGONIA MOUNTAINS
PIMA CO
SANTA CRUZ CO
PIMA COUNTY
SANTA CRUZ COUNTY
Green Valley
Arivaca Junction
Amado
Agua Linda
Tubac
Rio Rico
Nogales International
MINERAL HILL
HELMET PEAK
SAMANIEGO PEAK
KEYSTONE PEAK
HORSE PASTURE HILL
LOBO PEAK
NINJA PEAK
TWIN BUTTES
SOTO PEAK
GUNSIGHT MTN
CERRO COLORADO MOUNTAINS
SHERIFFS MESA
TWIN PEAKS
SARDINA PEAK
TUMACACORI PEAK
CERRO PRIETO
GROSVENOR HILLS
MT HOPKINS
MT WRIGHTSON
JOSEPHINE PEAK
MT WASHINGTON
ATASCOSA PEAK
BEAR VALLEY
BARTLETT MTN
PAJARITO PEAK
MT SMUGGLER
QUATES BUTTES
EXPLANATION
Flight line
Base from U.S. Geological Survey
digital data,1:250,000
North American Datum 83 (NAD 83)
Universal Transverse Mercator, zone 12N
0 2 4 6 8 10 MILES
0 2 4 6 8 10 KILOMETERS

Figure 22 (Previous page). Map showing areas and flight lines for the 1998 Santa Cruz transient electromagnetic survey. An electromagnetic and magnetic survey was flown over parts of south central Arizona by Geoterrex-Dighem (now Fugro, https://www.fugro.com/) from January 8–18, 1998. The survey covered five separate areas and approximately 2,500 line kilometers. These areas are shown using the actual flight line data from the survey. Area 1, Huerfano Butte; Area 3, Cottonwood Canyon; Areas 2, 4, and 5, are simply called Nogales and vicinity. Most of areas 2 and 5, and a small portion of area 4, lie within the study area. The majority of flight lines in each area have a spacing of approximately 400 m. Additionally there are several tie lines for each area that are flown perpendicular to the main set of flight lines.

and Karlik (1995) to convert transient electromagnetic data to conductivity in a cross-sectional format for each flight line in the survey. CDTs are based on a horizontal conductor model and generally do a good job of imaging horizontal conductors. While the depth and estimated conductivity may be approximate, the method is sensitive to the lateral extent of these conductors and therefore it can be very good at finding breaks and offsets (faults) in horizontal conductors. Vallée and Smith (2007) describe the CDT's utility as a transform method by saying "it works as well as other transform or inversion routines, all of which give somewhat different results."

The CDTs are delivered as groups of cross sectional grids (raster image) for each area (see fig. 22, areas 1, 2, 3, 4, and 5). Within an area, all grids have a horizontal datum reference which is the very top of cross sectional grid and is chosen slightly above the highest land elevation reached over the survey area. The terrain surface of the CDT grids has been projected to approximate the true terrain surface, but is not highly accurate. In addition, each grid in an area has a maximum depth of investigation that is specified from the horizontal datum reference chosen and not from the terrain surface. The maximum depth of investigation is the thickness of the entire CDT grid in meters. When viewing these terrain corrected CDT grids, the blank area between the top of the section and the first layer of real values represents air. The contour of the first layer of real values defines the ground surface and should approximately match the true topography. As you go deeper in the CDT, the data stop when a solution cannot be calculated at that location. Each CDT has 128 grid cells from top to bottom. Given that the depths of investigation in the Patagonia TEM survey in the study area range from 850 to 950 m, the vertical extent of each grid cell ranges from 6.64 m to 7.42 m. The horizontal extent of each grid cell varies from area to area but is generally about 23 m.

The conductivity values displayed in each CDT are given as the log base 10 of apparent conductivity in [Siemens/m] (a reading of –2 equals 0.01 [S/m]). To calculate approximate apparent resistivities in the CDT data use 1/(10x), where x is the CDT value (for example, CDT value = –2, resistivity = 1/.01 = 100 Ohm-m).

For the CDTs of area 5 in fig. 22, the depth of investigation is 900 m and the barometric reference (top of the cross-section grid) is 1,650 m. There are 20 west-to-east trending survey flight lines that have 400 m north-south spacing, in addition to four north-south "tie-lines" (fig. 22). Area 2 has 12 survey flight lines that trend northwest-southeast and 5 tie lines (fig. 22). The barometric reference for this area is 1,550 m and the depth if investigation is 850 m. Area 4 has 36 east-west trending survey flight lines and 3 tie lines (fig. 22). Only the easternmost tie line lies in the study area (fig. 22). The barometric reference for area 4 is 1,600 m and the depth if investigation is 950 m.

TEM Analysis and Interpretations in the Study Area

There are some caveats that should be considered when interpreting these data. These include: (1) our technique works best to resolve horizontal layers. These layers may be of differing lithologies of differing facies in sediments. Under the right conditions TEM interpretations including CDTs can locate the water table and distinguish saturated clays from saturated sands and possibly unsaturated sediments from saturated sediments. The method works well for determining when these layers are interrupted, for example, by facies changes, faults, steep contacts or intrusive bedrock; (2) acquiring TEM survey data over power lines or electrical noise of any kind greatly influences the data and the processing of the data. CDTs should be viewed with power line monitor information (which is also acquired during the survey) and the results in areas of electrical noise should not be considered accurate; (3) the conductivity values are apparent conductivities and approximate; (4) these data average conductivity over a large area; and (5) the CDT models are one dimensional. This, combined with the caveats 3 and 4, means that data presented in two CDTs acquired in one spot by flying in differing directions can differ.

Plate 2 displays each CDT (or portion thereof) in the study area just north or west of the plotted flight line. All CDTs and their flight lines are plotted over the geologic map of the study area (from Page and others, 2016). All flight lines numbered in the 201–212 range are from area 2 (fig. 22), flight lines in the 410–436 range are from area 4 (fig. 22) and flight lines in the 501–520 range are from area 5 (fig. 22). CDTs acquired from tie lines in each area are also numbered and displayed. In order to accommodate all of the flight lines in this format, the vertical dimension (Z or depth) of all grid cells in the CDT was reduced to about 40 percent of their original thickness. Plate 2 can be used to locate each CDT and to relate features in the CDT to geology. No depth scale is given for the CDTs presented in plate 2 due to both the approximate nature of estimated depths and space constraints.

Appendix 1 contains images of each CDT (or portion thereof) in the study area without vertically thinning the image. Included in these images is the power line monitor information that gives a relative electrical noise level and an approximate depth scale. Please see the "of20161152_Appendix1_readme.txt" file in appendix 1 for more information on the contents of the appendix. In addition, all data from the Santa Cruz TEM survey are included in appendix 2. This includes the raw survey measurement data and all associated files.

Figures 23, 24, and 25 display CDT 501, 510, and 516 (see plate 2 for locations) each plotted with a map view of their flight line and the power line monitor data acquired over the flight line. In addition, the corresponding portion of the geologic map of the study area (from plate 1) with potential field boundaries is plotted above the CDT. This allow for comparison between features on the CDT and the geologic map.

The CDTs in figures 23–25, and all CDTs in the study area, were used to help define the locations of concealed faults found in the geologic map of the study area (Page and others, 2016). In these figures, double ended arrows have been drawn between features on the geologic map and related features in the CDT. We required CDT features to be continuous over several adjacent CDTs or have other supporting evidence for them to be included in the geologic map.

The four concealed faults shown on the west side of the study area in figure 23 all have strong indications of disruption of horizontal conductors in the CDT (arrows 1, 2, 3, and 4) which continue to adjacent CDTs to the north and (or) south. Potential field gradient magnitude boundaries also are associated with the fault at arrow 4 and other disruptions in horizontal conductors are related to potential field boundaries but are not continuous enough to be mapped as faults. This area is a deep part of the basin and small contrasts in magnetic susceptibility or density may not be visible in the potential field data at depth. While information from CDTs help mapping some concealed faults, including these, not all concealed faults are based on CDT information and not all breaks in conductors on CDTs were mapped as concealed faults. Decisions made on what was a fault in the study area geologic map (Page and others, 2016) were based on continuity in offsets in conductors over the range of several CDTs, other geophysical information including potential field boundaries, and geologic knowledge of the study area.

The concealed fault on the east side of the study area in figure 23 (arrow 5) is the Mt. Benedict fault which is the boundary between igneous rock of the Mt. Benedict horst block (fig. 2) to the west and the basin fill in the graben to the east. This fault is well defined in the CDT and also is mapped to the north as separating outcropping bedrock lithologies (plate 2). The power line monitor data indicate three areas of concern, near UTM easting 504500E, 509800E, and 511000E. Two of the faults mentioned lie close to two of the power line problem areas but the CDT does not appear to be severely affected in these areas.

Offsets in horizontal conductors corresponding to mapped concealed faults can be seen in two locations in figure 24 at arrows 1 and 2. Strong Earth's magnetic field horizontal gradient magnitude boundaries are located just to the east of the fault at arrow 1. Arrow 3 indicates an abrupt change in conductivity from west to east located at the Grand Avenue fault (fig. 2). While there is much electrical interference in this location (fig. 24), the CDT still seems to accurately depict a change in conductivity at this location where the fault is exposed at the surface.

Arrow 4 in figure 24 indicates the Proto Canyon fault, a normal fault with down to the southeast offset. While a conductor near the surface makes it appear that the offset on this fault is down to the northwest, this may not be the same conductor. The southeast side of the fault indicates deep conductors while there is a bedrock high on the northwest side of the fault, indicating a down to the southeast movement. The white area in the CDT below conductors to the left of arrow 4 may indicate high resistivity bedrock at shallow depths indicating the offset is down to the southeast. The apparent offset near the surface is unexplained, but may be related to a contrast in sediment saturation.

Figure 25 displays three mapped concealed faults that show offsets or changes in horizontal conductors on the CDT. Again, care must be made in making interpretations in areas with large electrical noise. The fault associated with arrow 1 is visible in outcrop just to the north (plate 2) and thus also has strong geologic evidence. The faults associated with arrows 2 and 3 are in electrically quiet areas.

Also in figure 25, thick, highly conductive sediments can be seen in the red and magenta colors in the eastern third of the CDT. These likely represent saturated clay-rich rocks in the lower and middle Proto Canyon member of the Nogales formation, where much of the clay is from deep weathering of monzonite clasts (mainly feldspars) derived from map units Jb and Jbm (table 2). This feature extends from CDT 514 through CDT 520, and can be seen in plate 2.

Figure 26 displays several CDTs from area 5 as fences overlain on the southwest portion of the upper Santa Cruz Basin study area geology. The TEM survey flight lines corresponding to each displayed CDT are also shown. Only odd numbered CDTs are displayed so that the geologic map is visible between CDTs. This type of display gives a three-dimensional picture of basin fill apparent conductivity which is related to both basin fill lithology and sediment saturation and allows for a hydraulic characterization of basin fill sediments. These interpretations are preliminary and would need drilling or other testing to verify, but may help guide future studies.

Based on table 2, the following relationship between CDT values and sediment types is proposed. Blue colors in displayed CDTs in figure 26 may represent dry sand-rich sediments (fig 26, location A) or igneous rock (fig. 26, location B), green colors may represent sand-rich sediments in the vadose zone (fig. 26, location C), or possibly saturated volcanics or sediments that are well indurated and have little pore space and little water content (fig. 26, location D). Yellow colors may represent saturated sand-rich sediments (fig. 26, location E). Reds and magentas may represent saturated clay-rich

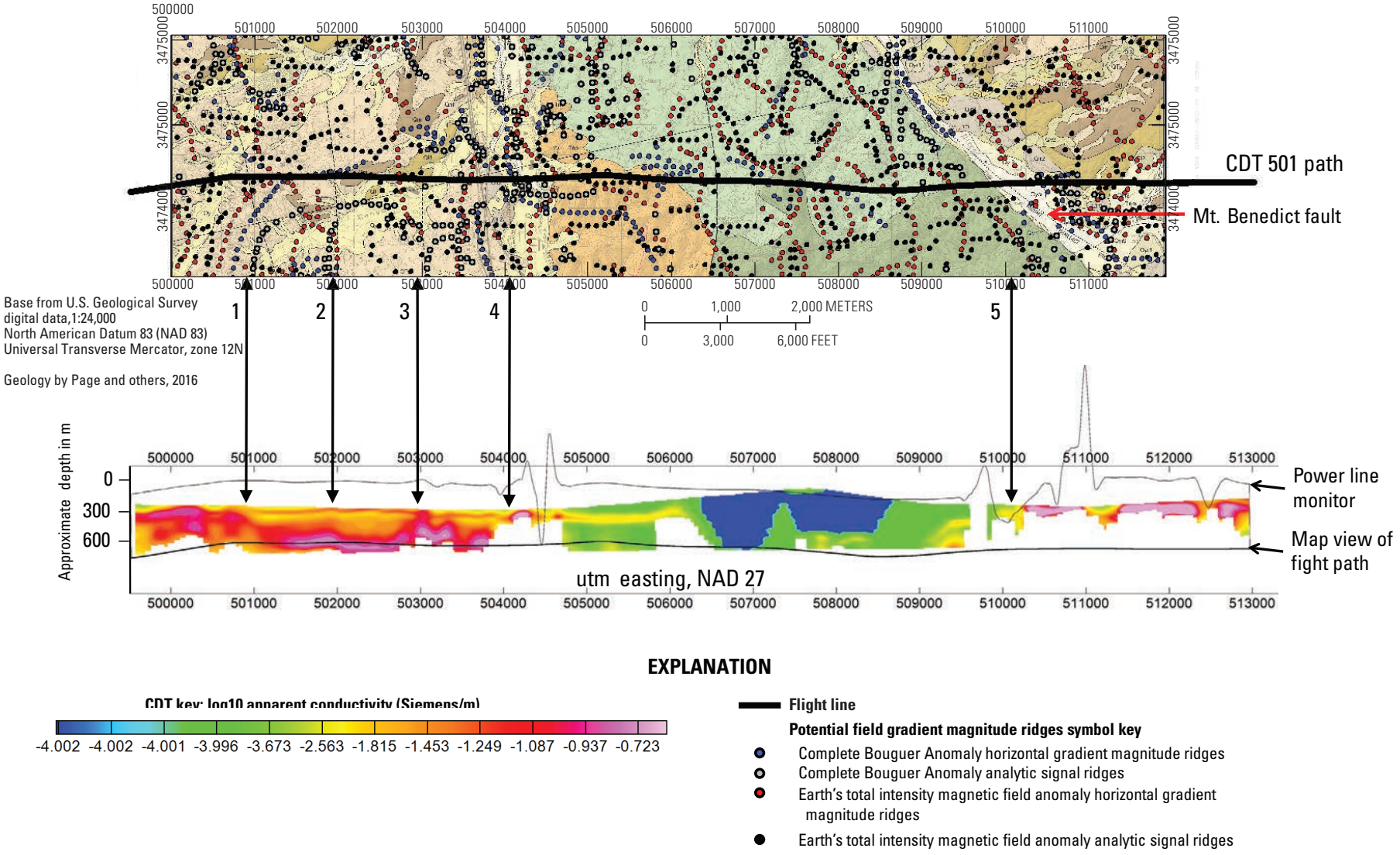

Figure 23. Conductivity-depth transform (CDT) for transient electromagnetic flight line 501. The corresponding portion of the geologic map of the study area with potential field boundaries is plotted above the CDT. In these figures, double ended arrows have been drawn between features on the geologic map and related features in the CDT. The four concealed faults shown on the geologic map all have strong indications of disruption of horizontal conductors in the CDT (arrows 1, 2, 3, and 4). The concealed fault on the east side of the CDT is the Mt. Benedict fault which is the boundary between igneous rock of the Mt. Benedict horst block to the west and the basin fill in the graben to the east. The power line monitor data indicate three areas of concern, near UTM easting 504500E, 509800E, and 511000E.

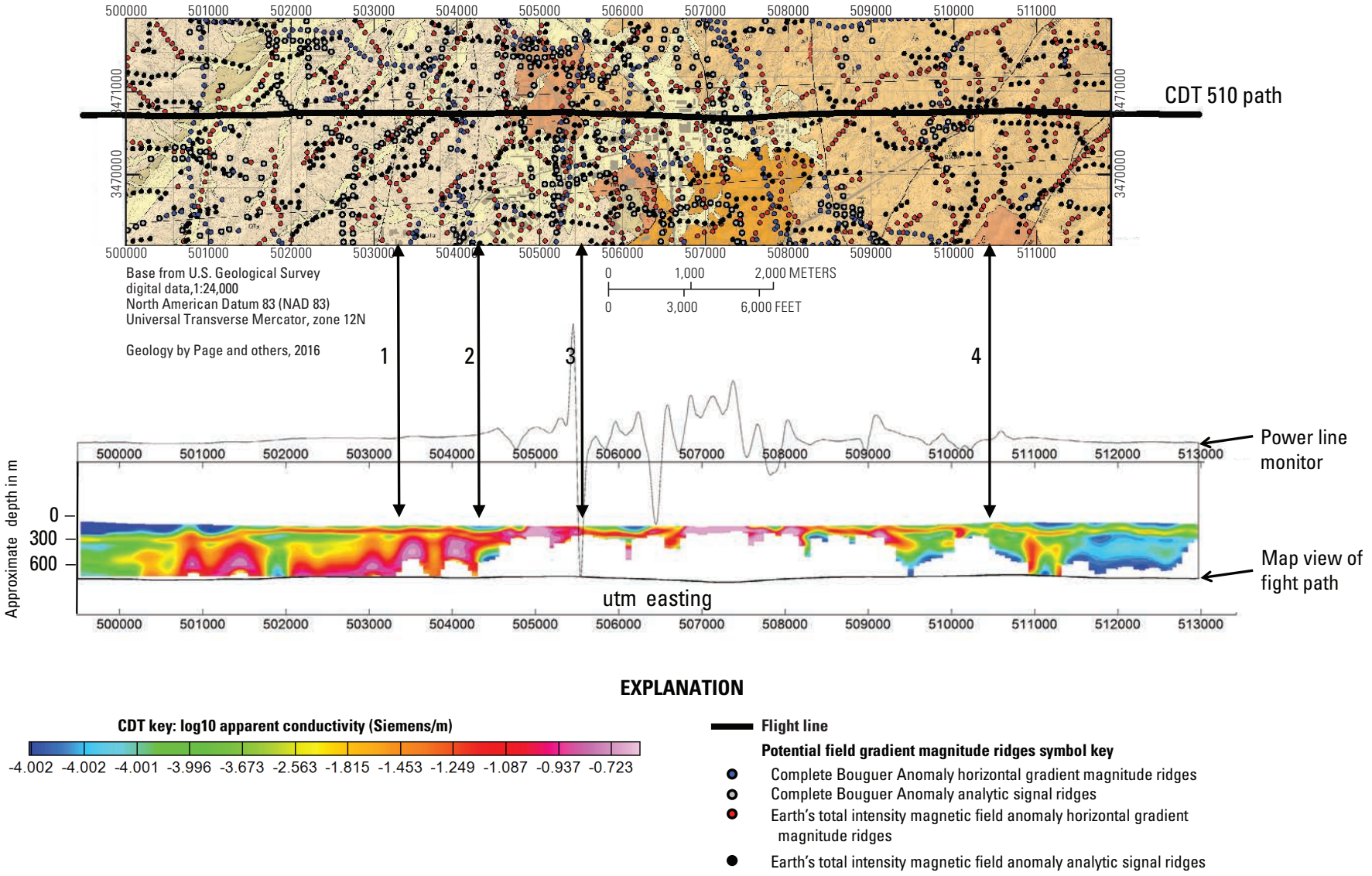

Figure 24. Conductivity-depth transform (CDT) for transient electromagnetic flight line 510. The corresponding portion of the geologic map of the study area with potential field boundaries is plotted above the CDT. In these figures, double ended arrows have been drawn between features on the geologic map and related features in the CDT. Offsets in horizontal conductors corresponding to mapped concealed faults can be seen in two locations at arrows 1 and 2. Arrow 3 indicates an abrupt change in conductivity from west to east located at the Grand Avenue fault. Arrow 4 indicates the Proto Canyon fault, a normal fault with down to the southeast offset. The white area in the CDT below conductors to the left of arrow 4 may indicate high resistivity bedrock at shallow depths indicating the offset is down to the southeast.

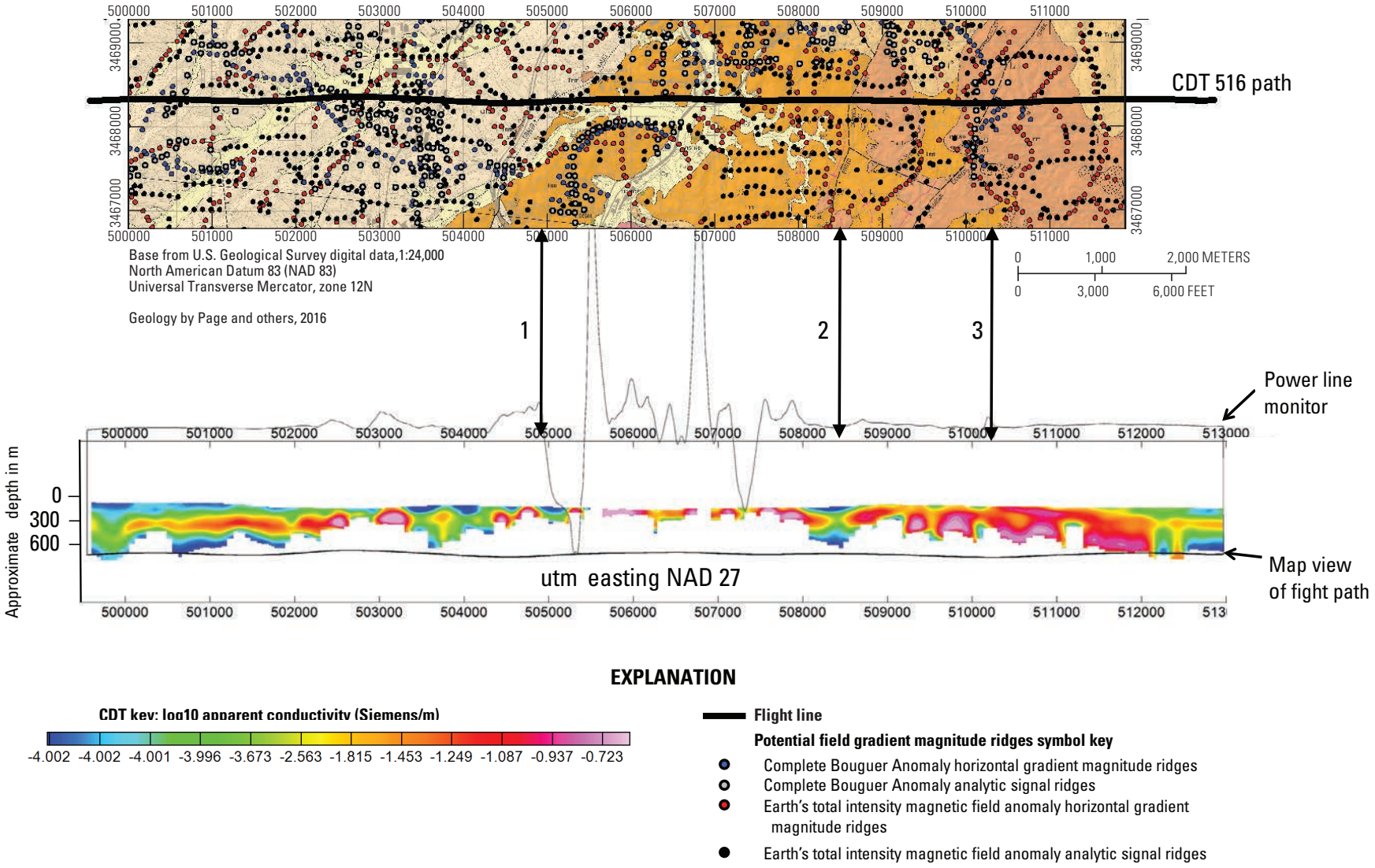

Figure 25. Conductivity-depth transform (CDT) for transient electromagnetic flight line 516. The corresponding portion of the geologic map of the study area with potential field boundaries is plotted above the CDT. In these figures, double ended arrows have been drawn between features on the geologic map and related features in the CDT. Three mapped concealed faults show offsets or changes in horizontal conductors on the CDT. The fault associated with arrow 1 is visible in outcrop jut to the north and thus also has strong geologic evidence. The faults associated with arrows 2 and 3 are in electrically quiet area. Thick, highly conductive sediments can be seen in the red and magenta colors in the eastern third of the CDT. These likely represent saturated clay-rich rocks in the lower and middle Proto Canyon member of the Nogales Formation, where much of the clay is from deep weathering of monzonite clasts (mainly feldspars) derived from map units Jb and Jbm.

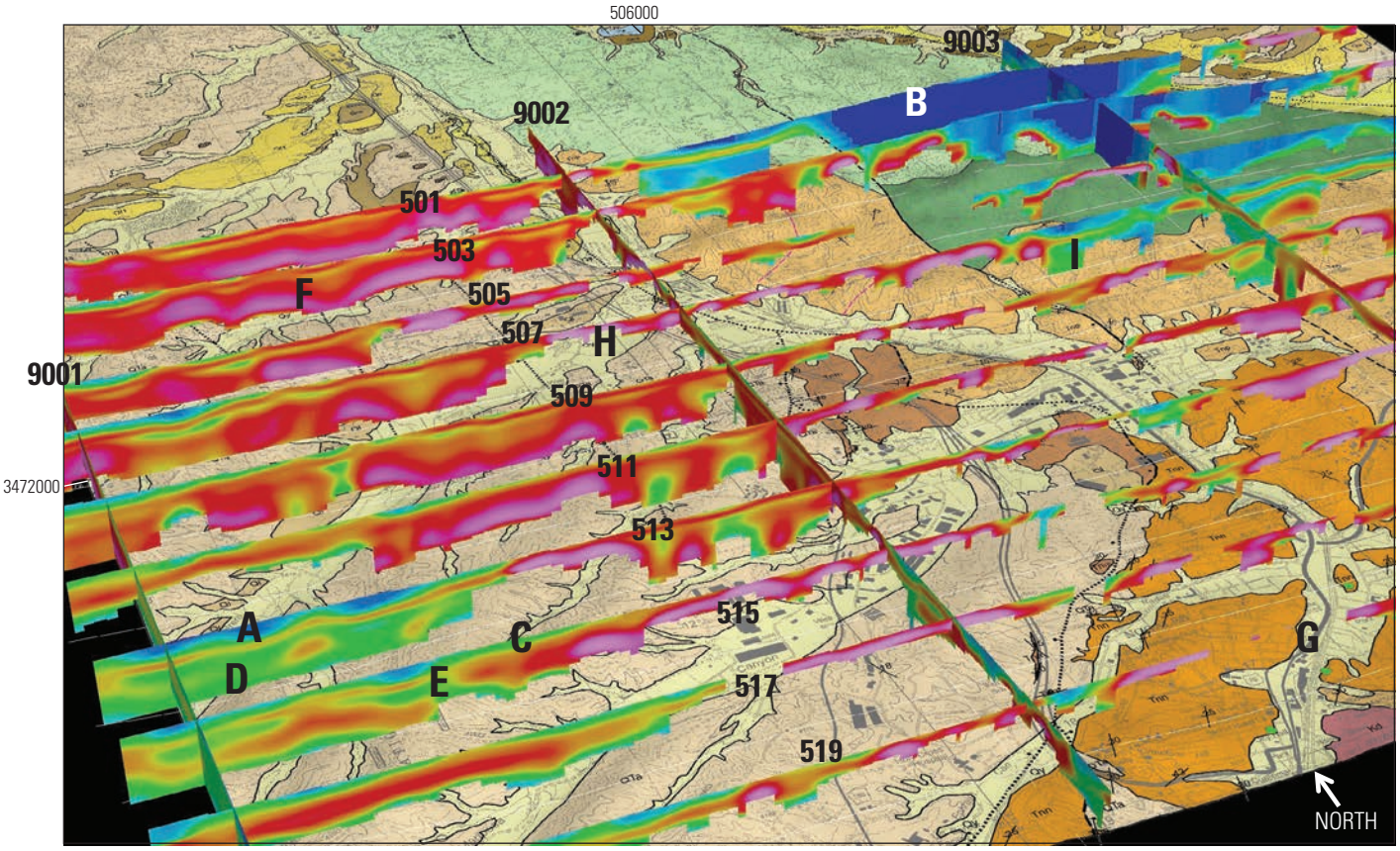

Geology by Page and others, 2016
Projection: Universal Transverse Mercator, zone 12N
North American Datum 1983 (NAD 83)

EXPLANATION

CDT key: log10 apparent conductivity (Siemens/m)

-4.002 -4.002 -4.001 -3.996 -3.673 -2.563 -1.815 -1.453 -1.249 -1.087 -0.937 -0.723

Location A—Blue colors in displayed CDTs may represent dry sand-rich sediments

Location B—Blue colors in displayed CDTs may also represent igneous rock

Location C—Green colors may represent sand rich sediments in the vadose zone

Location D—Green colors may also represent or saturated sediments that are well indurated and have little pore space and little water content

Location E—Yellow colors may represent saturated sand-rich sediments

Location F—Reds and magentas may represent saturated clay-rich sediments with magenta colored areas having the maximum clay content

Location G—Too much electrical noise is present in the data

Location H—Represents a possible bedrock high

Location I—May represent thick basin fill sediments

Figure 26. Area 5 conductivity-depth transforms (CDTs) plotted as fences over mapped geology (from Page and others, 2016). The time-domain electromagnetic (TEM) survey flight lines corresponding to each displayed CDT are also shown. Only odd numbered CDTs are displayed so that the geologic map is visible between CDTs. This type of display gives a three-dimensional picture of basin fill apparent conductivity which is related to both basin fill lithology and sediment saturation and allows for a hydraulic characterization of basin fill sediments. Flightlines for CDTs are white lines.

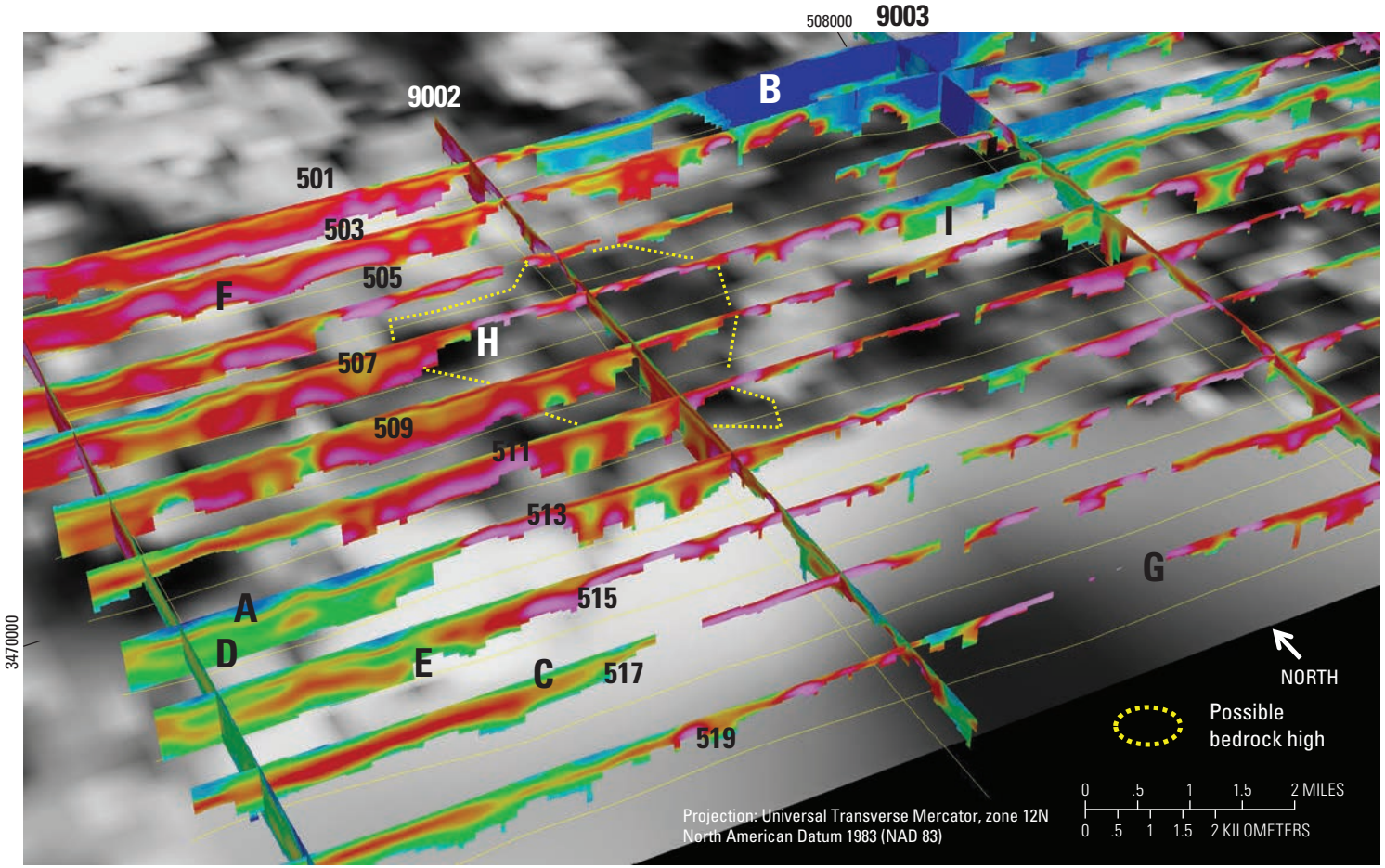

EXPLANATION

CDT key: log10 apparent conductivity (Siemens/m)

-4.002 -4.002 -4.001 -3.996 -3.673 -2.563 -1.815 -1.453 -1.249 -1.087 -0.937 -0.723

Depth to bedrock based on aeromagnetic interpretation in this report

shallow — deep

Location A—Blue colors in displayed CDTs may represent dry sand-rich sediments

Location B—Blue colors in displayed CDTs may also represent igneous rock

Location C—Green colors may represent sand rich sediments in the vadose zone

Location D—Green colors may also represent or saturated sediments that are well indurated and have little pore space and little water content

Location E—Yellow colors may represent saturated sand-rich sediments

Location F—Reds and magentas may represent saturated clay-rich sediments with magenta colored areas having the maximum clay content

Location G—Too much electrical noise is present in the data

Location H—Represents a possible bedrock high

Location I—May represent thick basin fill sediments

Figure 27. Area 5 conductivity-depth transforms (CDTs) plotted as fences over grayscale depth-to-bedrock map (from figure 12). The time-domain electromagnetic (TEM) survey flight lines corresponding to each displayed CDT are also shown. Only odd numbered CDTs are displayed so that the grayscale depth to bedrock map is visible between CDTs. This map indicates a possible bedrock high in this region, location H. Flightlines for CDTs are yellow lines.

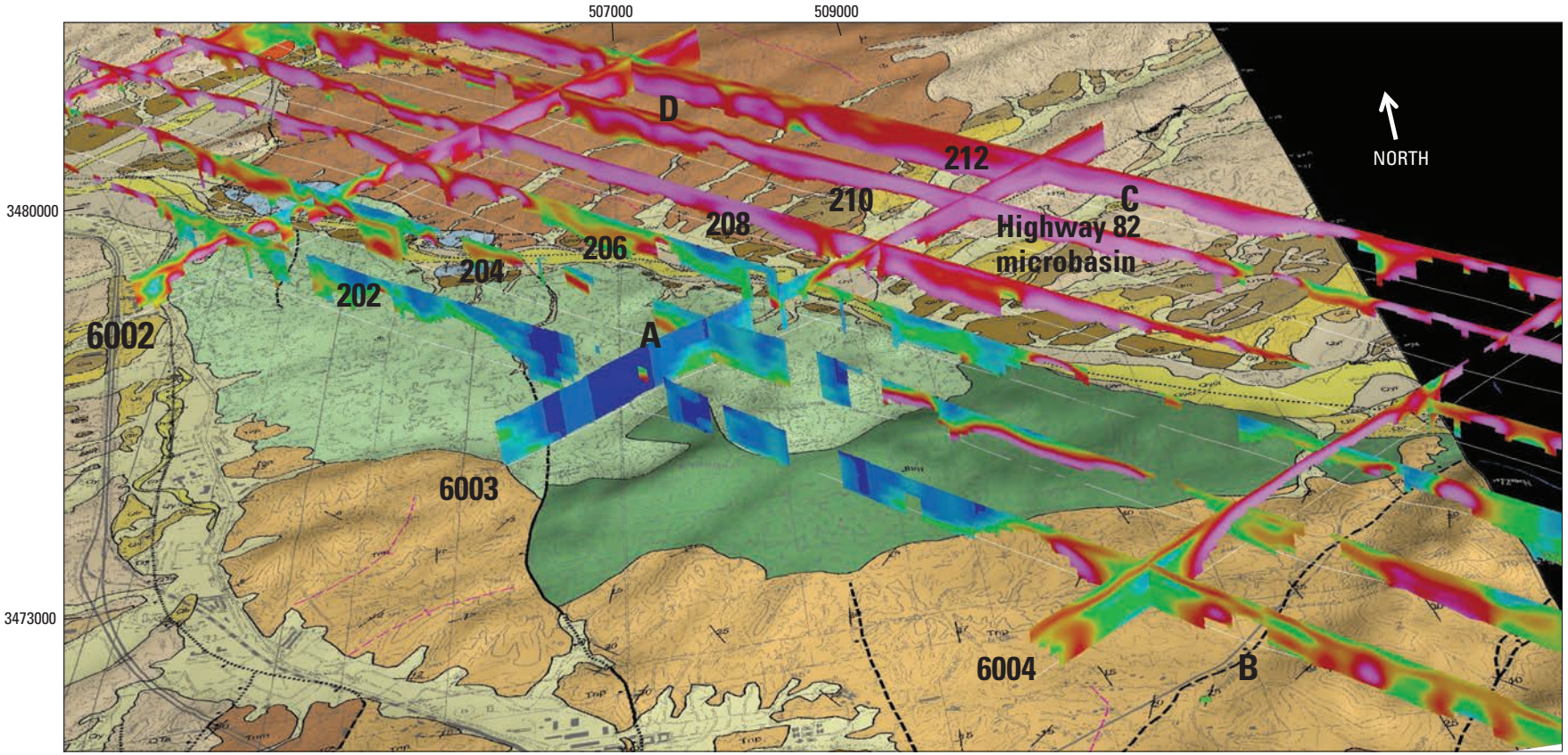

Figure 28. Area 2 conductivity-depth transforms (CDTs) plotted as fences over mapped geology (from Page and others, 2015). The time-domain electromagnetic (TEM) survey flight lines corresponding to each displayed CDT are also shown. Only even numbered CDTs are displayed so that the geologic map is visible between CDTs. The resistive igneous rock in the Mt. Benedict horst block (fig. 2) is visible in the deep to light blue colors in the CDTs at location A. Location B shows offset in conductors at the mapped concealed fault. These data, as well as the aeromagnetic data based depth to bedrock map from figure 12, indicate deep bedrock and great thickness of sediments near location C (the State Highway 82 microbasin) and the structural complexity in the bedrock at location D. Flightlines for CDTs are white lines.

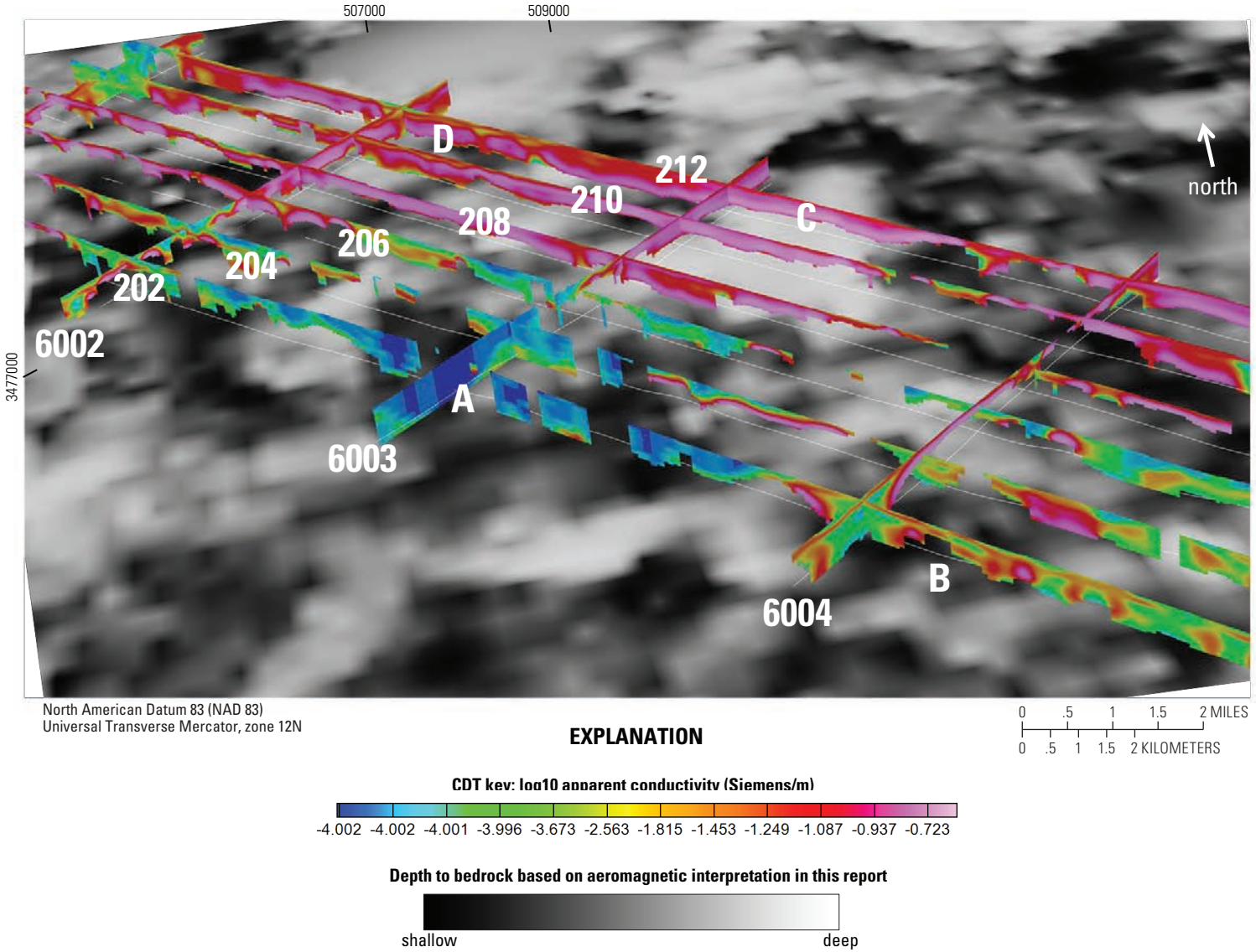

Figure 29. Area 2 conductivity-depth transforms (CDTs) plotted as fences over grayscale depth to bedrock map. The resistive igneous rock in the Mt. Benedict horst block (fig. 2) is visible in the deep to light blue colors in the CDTs at location A. Location B shows offset in conductors at the mapped concealed fault. These data, as well as the aeromagnetic data based depth to bedrock map from figure 12, indicate deep bedrock and great thickness of sediments near location C (the State Highway 82 microbasin) and the structural complexity in the bedrock at location D. Flightlines for CDTs are white lines.

sediments with magenta colored areas having the maximum clay content (fig. 26, location F). Based on this , the basin fill in figure 26 displays deep saturated clay-rich sediments in the west central portion of the study area (CDTs 501–509) grading to more sand-rich saturated sediments to the south with relatively thick unsaturated sediments at the surface (CDTs 513–515). More clay-rich saturated sediments are found at depth beneath sand-rich sediments in CDT 517. Since the exact clay contents of these sediments is unknown, it is difficult to make statements about their potential as an aquifer but it does appear that these sediments are saturated.

Areas where the CDTs do not appear correspond to urban areas in the City of Nogales (like location G) where, in general, too much electrical noise is present in the data. It should be noted again that depths in CDTs can be very inaccurate and it is unwise to take the depths presented in the CDTs as actual depths of conductors.

In addition, the mapped concealed faults discussed in figure 23–25 can be seen in figure 26 by the offsets that they create in basin fill features. Based on experience with CDTs, regions where calculated solutions in the CDT disappear at depth may be related to bedrock highs (igneous or other non-conductive rock), especially when the upper sediments in these regions are very conductive. This is logical in that current is dissipated in the upper conductive region and does not enter the very resistant bedrock high (often igneous rock) directly below. Such a feature is seen at location H in figure 26. This potential bedrock high is centered in the Potrero Canyon (fig. 3), near water production wells for the City of Nogales, Ariz. This bedrock high could possibly result in a perched aquifer in this region.

Figure 27 is similar to figure 26 except that instead of being plotted on the geologic map of the study area, the CDTs are plotted on a grayscale version of the depth to bedrock map (fig. 12). This integrated gravity and magnetic depth to bedrock map also indicates a possible bedrock high in this region (location H). Both CDTs and the depth to bedrock map also indicate a potential deep basin feature at location “I”. This feature is very close to the Mt. Benedict horst block (fig. 2) and would require large vertical fault offsets in the concealed monzonite, map unit Jbm (table 2).

Figure 28 displays CDTs from area 2 plotted as fences over the southeast portion of the upper Santa Cruz Basin study area geologic map. The resistive igneous rock in the Mt. Benedict horst block (fig. 2) is visible in the deep to light blue colors in the CDTs at location A. Location B shows offset in conductors at the mapped concealed fault. Thick deep conductors may represent saturated clay-rich sediments at location C and disruption in conductors in the area around location D indicates complex bedrock structure. Figure 29 is similar to figure 28 except that CDTs are plotted on a grayscale depth to bedrock map. The aeromagnetic data based depth to bedrock map from figure 12 also indicates deep bedrock and great thickness of sediments near location C (the State Highway 82 microbasin) and the structural complexity in the bedrock at location “D”.

Conclusions

The upper Santa Cruz Basin is an important groundwater basin containing the regional aquifer for the City of Nogales, Arizona. This report provides data and interpretations of data aimed at better understanding the bedrock morphology and structure of the upper Santa Cruz Basin in the Rio Rico and Nogales 1:24,000-scale quadrangles and includes some information on the physical properties of the sediments in the basin.

Potential field boundaries were used to find the edges of bedrock bodies of contrasting rock magnetic intensity and (or) rock density where they are concealed by Tertiary and Quaternary basin fill. These geophysical boundaries may represent concealed faults and (or) contacts in the bedrock under basin sediments. Potential field boundaries identified the range front faults along the Mt. Benedict horst block (fig. 2), located possible fault controlled canyons to the west of Mt. Benedict (fig. 2), the possible edges of buried lava flows, and numerous other possible concealed faults and contacts. The horizontal gradient method applied to the 1996 Patagonia aeromagnetic survey data produced the highest number and most significant potential field boundaries.

The 1996 Patagonia aeromagnetic survey had several advantages over gravity data for depth to bedrock estimation, including much greater spatial density of measurements. The final depth to bedrock map was produced by choosing the maximum depth from each of the three methods at a given location and combining all maximum depths. In locations of rocks with a known reversed natural remanent magnetic field, gravity based depth estimates from Gettings and Houser (1997) were used. The final depth to bedrock map has a resolution of 200 m (fig. 12), which provides the most detailed map of depth to bedrock in the upper Santa Cruz Basin study area to date.

The depth to bedrock map was tested by modeling aeromagnetic anomaly data along six profiles. These cross sectional models demonstrated that by using the depth to bedrock map generated in this study, known and concealed faults, measured and estimated magnetic susceptibilities of rocks found in the study area, and estimated natural remanent magnetic intensities and directions reasonable geologic models can be built. This is an indication that the depth to bedrock map is a reasonable interpretation of the data.

Finally, CDTs derived from the 1998 Santa Cruz Basin transient electromagnetic survey were used to help identify basin structure and some physical properties of the basin fill. These data helped confirm many faults and contacts in the basin bedrock and their expressions in the basin fill.

The CDTs also helped to confirm basin depth estimates in both deep and shallow parts of the basin. In particular these data support a bedrock high in the area of Potrero Canyon (fig. 3) and a large depth to bedrock in the Highway 82 microbasin (fig. 12). The CDTs identified many of the concealed faults in the study area and possibly indicate deep saturated clay-rich sediments in the west central portion of the study area, grading to more sand-rich saturated sediments to the south with

relatively thick unsaturated sediments at the surface. Also, the CDTs may indicate deep saturated clay-rich sediments in the Highway 82 microbasin.

Possible Additional Work

The data presented and analyzed in this report may give insights to the direction future work may take to improve the understanding of the hydrogeology in the upper Santa Cruz Basin. More geophysical work or drilling could be done over prominent basin features, such as bedrock highs or lows, to test the validity of these features. These geophysical studies could include truck-mounted magnetometer surveys and (or) gravity surveys with high station densities.

The southeast part of the upper Santa Cruz Basin study has a very limited number of gravity stations and gravity-based depth to bedrock estimates developed here are questionable there. The southeast part of the study area also has a number of basalt flows interbedded with Nogales Formation sediments which may affect aeromagnetic based depth to bedrock estimates. Additional gravity stations in this area could be beneficial.

The only interpretation of the 1998 Santa Cruz TEM survey data presently available is CDTs. While these provide valuable information they are only transforms based on fairly simple mathematical assumptions. True inversion of these data may produce conductivity-depth results with more accurate conductivities and depths of conductors than the CDTs provide, and give a more accurate representation of the groundwater resources in the study area.

References Cited

Blakely, R.J., and Simpson, R.W., 1986, Approximating edges of source bodies from magnetic or gravity anomalies: Geophysics, v. 51, no. 7, p. 1494–1498.

Bournas, Nasreddine and Baker, H.A., 2001, Interpretation of magnetic anomalies using the horizontal gradient analytic signals: Annali Di Geofisica, v. 44, no. 3, June 2001.

Bultman, M.W., 2002, Time-domain electromagnetic signatures of polymetallic vein deposits in Cottonwood Canyon area, Santa Cruz County, Arizona, U.S. Geological Survey Open-File Report 02–18. [Also available at http://pubs.usgs.gov/of/2002/0018/.]

Bultman, M.W., 2014, Detailed interpretation of aeromagnetic data from the Patagonia Mountains Area, Southeastern Arizona: U.S. Geological Survey Scientific Investigations Report 2015–5029. [Also available at http://pubs.usgs.gov/sir/2015/5029/.]

Bultman, M.W., Gettings, M.E., and Wynn, Jeff, 1999, An interpretation of the 1997 airborne electromagnetic (AEM) survey, Fort Huachuca vicinity, Cochise County, Arizona, U.S. Geological Survey Open-File Report 99–7–A. [Available as 1 CDROM.]

Casto, D.W., 2001, Calculating depths to shallow magnetic sources using aeromagnetic data from the Tucson basin: U.S. Geological Survey Open-File report 01–505, 231 p.[Also available at http://pubs.usgs.gov/of/2001/0505/.]

Clark, D.A., 1997, Magnetic petrophysics and magnetic petrology—Aids to geological interpretation of magnetic surveys: AGSO Journal of Australian Geology and Geophysics, v. 17, p. 83–103.

Cordell, Lindrith, and Grauch, V.J.S., 1985, Mapping basement magnetization zones from aeromagnetic data in the San Juan Basin, New Mexico, *in* Hinze, W.J., ed., The utility of regional gravity and magnetic anomaly maps: Tulsa, Okla., Society of Exploration Geophysicists, p. 181–197.

Culbertson, Chris, Lytle, W.E., McMillian, M.M., Sternberg, B.K., and Withers, K.B., Transient electromagnetic investigation of microbasin morphology along the Santa Cruz River, Nogales, Arizona: Geophysics Field Camp 2010, May 11, 2010, University of Arizona, 117 p.

Dickinson, J.E., Kennedy, J.R., Pool, D.R., Cordova, J.T., Parker, J.T., Macy, J.P., and Thomas, B., 2010, Hydrogeologic framework of the middle San Pedro watershed, southeastern Arizona: U.S. Geological Survey Scientific Investigations Report 2010–5126, 36 p. [Also available at http://pubs.usgs.gov/sir/2010/5126/.]

Drewes, Harald, 1971, Geologic map of the Mount Wrightson quadrangle, southeast of Tucson, Santa Cruz and Pima Counties, Arizona: U.S. Geological Survey Miscellaneous Geologic Investigations Map I–614, scale 1:48,000.

Drewes, Harald, 1972, Cenozoic rocks of the Santa Rita Mountains, Southeast of Tucson: U.S. Geological Survey Professional Paper 746, 66 p. [Also available at https://pubs.er.usgs.gov/publication/pp746.]

Drewes, Harald, 1980, Tectonics of southeastern Arizona: U.S. Geological Survey Professional Paper 1144, 10 pl., 96 p. [Also available at https://pubs.er.usgs.gov/publication/pp1144.]

Drewes, Harald, 1996, Geology of Coronado National Forest, chap. B *of* du Bray, E.A., ed., Mineral resource potential and geology of Coronado National Forest, southeastern Arizona and southwestern New Mexico: U.S. Geological Survey Bulletin 2083–A–K, p. 17–41. [Also available at https://pubs.er.usgs.gov/publication/b2083AK.]

Drewes, Harald, Fields, R.A., Hirschberg, D.M., and Bolm, K.S., 2002, Spatial digital database for the tectonic map of southeast Arizona: U.S. Geological Survey Geologic Investigations Series I–1109. [Also available at http://pubs.usgs.gov/imap/i1109/.]

Geosoft, 2015, Oasis montaj (ver. 8.4 and 8.5): Toronto, Geosoft Inc., North America, http://www.geosoft.com/products/oasis-montaj/overview.

Gettings, M.E., 2002, An interpretation of the 1996 aeromagnetic data for the Santa Cruz Basin, Tumacacori Mountains, Santa Rita Mountains, and Patagonia Mountains, south-central Arizona: U.S. Geological Survey Open-File Report 2002–99, 44 p. [Also available at http://pubs.usgs.gov/of/2002/of02-099/of02-99.pdf.]

Gettings, M.E. and Houser, B.B., 1997, Basin geology of the upper Santa Cruz Valley, Pima and Santa Cruz Counties, Southeastern Arizona: U.S. Geological Survey Open-File Report 97–676, 39 p. [Also available at https://pubs.er.usgs.gov/publication/ofr97676.]

Grauch, V.J.S., and Cordell, Lindrith, 1987, Limitations on determining density or magnetic boundaries from the horizontal gradient of gravity or pseudogravity data: Geophysics, v. 52, no.1, p.118–121.

Gunn, P.J., 1997, Quantitative methods for interpreting aeromagnetic data, a subjective review: AGSO, Australian Journal of Geology and geophysics, v. 17, no. 2, p. 105–113.

Hagstrum, J.T., 1994, Remagnetization of Jurassic volcanic rocks in the Santa Rita and Patagonia Mountains, Arizona—Implications for North American polar wander: Journal of Geophysical Research, v. 99, is. B8, p. 15103–15113.

Halpenny, L.C., 1964, Geophysical and geohydrological investigation of Santa Cruz River Valley, International boundary to mouth of Sonoita Creek: Prepared for the International Water and Boundary Commission, United States and Mexico: Tucson, Ariz., Water Development Corporation.

Halpenny L.C., and Halpenny P.C., 1988, Review of hydrogeology of Santa Cruz Basin in the vicinity of Santa Cruz-Pima County line: Tucson, Ariz., Water Development Corporation.

Hood, Peter, 1965, Gradient measurements in aeromagnetic surveying: Geophysics, v. 30, is. 5, p. 891–902.

Hsu, Shu-Kun, Coppens, Dorothee, and Shyu, Chuen-Tien, 1998, Depth to magnetic source using the generalized analytic signal: Geophysics, v. 63, no. 6, p. 1947–1957.

Koenigsberger, J.G., 1938a, Natural residual magnetism of eruptive rocks: Terrestrial Magnetism and Atmospheric Electricity, v. 43, no. 2, p. 119–130, doi:10.1029/TE043i002p00119.

Koenigsberger, J.G., 1938b, Natural residual magnetism of eruptive rocks: Terrestrial Magnetism and Atmospheric Electricity, v. 43, no. 3, p. 299–320, doi:10.1029/TE043i003p00299.

Morris, Bill, Ugalde, Hernan, and Thomson, Vicki, 2007, Magnetic remanence constraints on magnetic inversion models—The leading edge: Society of Exploration Geophysicists, v. 26, is. 8, p. 960–964.

Nabighian, M.N., 1972, The analytic signal of two dimensional magnetic bodies with polygon cross-section—Its properties and use for automated anomaly interpretation: Geophysics, v. 37, p. 507–517.

Nabighian, M.N., 1974, Additional comments on the analytic signal of two dimensional magnetic bodies with polygon cross-section: Geophysics, v. 39, p. 85–92.

Nabighian, M.N., 1984, Towards a three-dimensional interpretation of potential field data via generalized Hilbert transforms—Fundamental relations: Geophysics, v. 49, p. 780–786.

National Oceanic and Atmospheric Administration (NOAA), 2014, International Geomagnetic Reference Field: National Oceanic and Atmospheric Administration, accessed April, 2014 at http://www.ngdc.noaa.gov/IAGA/vmod/igrf.html.

Oppenheimer, J.M., and Sumner, J.S., 1980, Depth-to-bedrock map, Basin and Range province, Arizona: Tucson, University of Arizona, Department of Geosciences, Laboratory of Geophysics, 1 sheet, scale 1:1,000,000. [Available as Arizona Geological Survey publication NP–14].

Page, W.R., Menges, C.M., Gray, Floyd., Berry, M.E., Cosca, M.A., and Bultman, M.W., 2016, Geologic Map of the Rio Rico and Nogales quadrangles, Santa Cruz County, Arizona: U.S. Geological Survey Scientific Investigations Map 3354, 32 p., 2 sheets, scale 1:24,000, http://dx.doi.org/10.3133/sim3354.

Phillips, J.D., 1997, Potential-field geophysical software for the PC, version 2.2: U.S. Geological Survey Open-File Report 97–725, 34 p. [Also available at https://pubs.er.usgs.gov/publication/ofr97725.]

Phillips, J.D., 2000, Locating magnetic contacts—A comparison of the horizontal gradient, analytic signal, and local wavenumber methods, *in* 2000 Society of Exploration Geophysicists (SEG) Annual meeting, Calgary, Alberta, August 6–11, Technical Program Expanded Abstracts: Calgary, Alberta, Society of Exploration Geophysicists, p. 402–405.

Phillips, J.D., 2002, Processing and interpretation of aeromagnetic data for the Santa Cruz Basin—Patagonia Mountains area, south-central Arizona: U.S. Geological Survey Open-File Report 2002–98. [Also available at http://pubs.usgs.gov/of/2002/0098/.]

Phillips, J.D., 2007, Geosoft eXecutables (GX's) developed by the U.S. Geological Survey, version 2.0, with notes on GX development from Fortran code: U.S. Geological Survey Open-File Report 2007–1355, 111 p. [Also available at http://pubs.usgs.gov/of/2007/1355/.]

Phillips, J.D., Hansen, R.O., and Blakely, R.J., 2007, The use of curvature in potential-field interpretation: Exploration Geophysics, v. 38, p. 111–119.

Phillips, J.D., Nabighian, M.N., Smith, D.V., and Li, Yaoguo, 2007, Estimating locations and total magnetization vectors of compact magnetic sources from scalar, vector, or tensor magnetic measurements through combined Helbig and Euler analysis *in* Seventy-Seventh Annual Meeting, San Antonio, Texas, Sept. 23–28, 2007, Technical Program Expanded Abstracts: San Antonio, Tex., Society of Exploration Geophysicists, , 5 p.

Reid, A.B., Allsop, J.M., Granser, H., Millet, A.J. and Somerton, I.W., 1990. Magnetic interpretation in three dimensions using Euler deconvolution: Geophysics, v. 55, is. 1, p. 80–91.

Richard, S.M., Shipman, T.C., Greene, L.C., and Harris, R.C., 2007, Estimated depth to bedrock in Arizona: Arizona Geological Survey Digital Geologic Map Series DGM–52 2007, ver. 1.0.

Roest, W.R., and Pilkington, Mark, 1993, Identifying remanent magnetization effects in magnetic data: Geophysics v. 58, is. 5, p. 653–659, doi10.1190/1.1443449.

Rubin, Yoram, Hubbard, S.S., Wilson, Amy, and Cushey, M.A., 1999, Aquifer characterization, chap. 10 *of* Delleur, J.W., ed., The handbook of groundwater engineering: CRC Press LLC.

Saltus, R.W., and Jachens, R.C., 1995, Gravity and basin-depth maps of the Basin and Range Province, Western United States: U.S. Geological Survey Geophysical Investigations Map, GP-1012, p., 1 sheet, scale 1:2,500,000. [Also available at https://pubs.er.usgs.gov/publication/gp1012.]

Simons, F.S., 1974, Geologic map and sections of the Nogales and Lochiel Quadrangles, Santa Cruz County, Arizona: U.S. Geological Survey Miscellaneous Investigations Series Map I–762, scale 1:48,000. [Also available at https://pubs.er.usgs.gov/publication/i762.]

Sweeney, R.E. and Hill, P.L. 2001, Arizona aeromagnetic and gravity maps and data—A web site for distribution of data: U.S. Geological Survey Open-File Report 01–0081. [Available at http://pubs.usgs.gov/of/2001/ofr-01-0081/]

Thompson, D.T., 1982, EULDPH—A new technique for making computer-assisted depth estimates from magnetic data: Geophysics, v. 47, p. 31–37.

University of Texas at El Paso (UTEP), 2014, Gravity database of the U.S.: El Paso, Tex., University of Texas, Office of Research and Sponsored Projects, accessed January, 2014 at http://research.utep.edu/default.aspx?tabid=37229.

Urquhart, Ted, 1988, Decorrugation of enhanced magnetic field maps, *in* Proceedings of the 58th Society of Exploration Geophysicists Annual International Conference and Exhibition, Expanded Abstracts, Anaheim, Calif., October 30-November 3, 1988: Society of Exploration Geophysicists, p. 371–372.

U.S. Geological Survey, 2000, Three aeromagnetic surveys in south central Arizona; a web site for distribution of data, U.S. Geological Survey Open-File Report 2000–155, https://pubs.er.usgs.gov/publication/ofr00155.

Vallée, M.A., and Smith, R.S., 2007, Comparison of Fixed-Wing Airborne Electromagnetic 1D Inversion Methods, *in* 5th Decennial International Conference on Mineral Exploration, Poster Papers, Toronto, September 9–12, 2007: Exploration 07, accessed in 2014 at http://www.dmec.ca/ex07-dvd/E07/posters.html.

Wolfgram, Peter, and Karlik, Gulcin, 1995, Conductivity-depth transform of GEOTEM data: Exploration Geophysics, v. 26, is. 2/3, p. 179–185.

Wynn, Jeff, 2006, Mapping ground water in three dimensions—An analysis of airborne geophysical surveys of the upper San Pedro River basin, Cochise County, southeastern Arizona: U.S. Geological Survey Professional Paper 1674. [Also available at http://pubs.usgs.gov/pp/2006/1674/.]

Appendix 1. Santa Cruz Transient Electromagnetic Survey Conductivity-Depth Transforms (CDT) Plots

Appendix 1 contains images of each CDT (or portion thereof) in the study area without vertically thinning the image. Included in these images is the power line monitor information that gives a relative electrical noise level and an approximate depth scale. Please see the "of20161152_Appendix1_readme.txt" file in appendix 1 for more information on the contents of the appendix.

The CDTs are as grouped by survey area (fig. 22) and include area 2, 4, and 5. Within an area, all grids have a horizontal datum reference which is the very top of grid and is chosen slightly above the highest land elevation reached over the survey area. The terrain surface of the CDT grids has been projected to approximate the true terrain surface, but is not highly accurate. In addition, each grid in an area has a maximum depth of investigation that is specified from the horizontal datum reference chosen and not from the terrain surface. It is the thickness of the entire CDT grid in meters. When viewing these terrain corrected CDT grids, the blank area between the top of the section and the first layer of real values represents air. The contour of the first layer of real values defines the ground surface and should match the true topography. As you go deeper in the CDT, the data stop when a solution cannot be calculated at that location. Each CDT has 128 grid cells from top to bottom. Given that the depths of investigation in the Patagonia TEM survey in the study area range from 850 to 950 m, the vertical extent of each grid cell ranges from 6.64 m to 7.42 m. The horizontal extent of each grid cell varies from area to area but is generally about 23 m.

The conductivity values displayed in each CDT are the log 10 of apparent conductivity (Siemens/m). So, a reading of –2 from the data displayed in the CDT grid represents 10-2 which equals 0.01 S/m. To calculate approximate apparent resistivities in the CDT data use 1/(10x) where x is the CDT reading (for example, –2 = 1/.01 = 100 Ohm-m). A conductivity key for all CDTs is included in Appendix 1 main directory.

TEM data for areas 2 and 5 lie almost entirely in the study area (fig. 22). Area 4 lies only partially in the study area. For the CDTs of area 5, the depth of investigation is 900 m and the barometric reference (top of the cross-section grid) is 1,650 m. There are 20 west-to-east trending lines that have a 400 m north-south spacing in addition to four north-south "tie-lines" (fig. 22). Area 2 has 12 flight lines that trend northwest-southeast and 5 tie lines (fig. 22). The barometric reference for this area is 1550 m and the depth of investigation is 850 m. Area 4 has 36 east-west trending flight lines and 3 tie lines (fig. 22). The barometric reference for area 4 is 1,600 m and the depth of investigation is 950 m. Depths for features on the CDTs should be computed using this information. More information is given in the file cdt_info_from_contractor.pdf in Appendix 1 main directory.

All CDTs include a map view of the flight path plotted as a line under the CDT image. They also include a plot of the power line monitor data above the CDT image. The UTM northings shown on the sides of each CDT plot reflect the geographic placement of the flight line. The UTM eastings shown below each CDT plot reflect the geographic location of the flight line data, the CDT data, and the power line data.

There are some caveats that should be considered when interpreting these data. These include: (1) The techniques work best to resolve horizontal layers. These layers may be differing lithologies of differing facies in sediment, especially when relate to clay content. The method works well for finding when these layers are interrupted, for example, by faults or intrusives; (2) Acquiring TEM survey data over power lines or electrical noise of any kind greatly influences the data and the processing of the data. CDTs should be viewed with power line monitor information (which is also acquired during the survey) and results in area of electrical noise should not be considered accurate; (3) Under the right conditions it can locate the water table and distinguish saturated clays from saturated sands and possibly unsaturated sediments from saturated sediments. But this is not always the case; (4) The conductivity values are apparent conductivities and approximate; (5) These data average conductivity over a large area; and 6) The CDT models are one dimensional. This combined with the caveats 4 and 5, means that data presented in two CDTs acquired in one spot by flying in differing directions can differ.

The exact location of all CDT flight lines can be found in plate 2 of this report.

Appendix 2. Santa Cruz Transient Electromagnetic Survey Data

All data from the Santa Cruz TEM survey are included in appendix 2. This includes the raw survey measurement data and all associated files.

From January 8th to 18th, 1998, an electromagnetic and magnetic survey was flown by Geoterrex Dighem (now Fugro, https://www.fugro.com/) on behalf of the U.S. Geological Survey. Five areas were flown in the Pima and Santa Cruz Counties, Arizona. A total of 2,486.9 line kilometers of data were collected. The survey areas are referred to as areas 1, 2, 3, 4 and five,

The survey data were compiled and processed in the Geoterrex-Dighem Ottawa office and are presented as maps of the total intensity magnetics, flight path, and the radar altimeter, multiparameter profiles with conductivity-depth-transform sections, digital line and grid archive files.

ISSN 2331-1258 (online)
http://dx.doi.org/10.3133/ofr20161152